

Dissertation

Design, Calibration and Tests  
of an Extended-Range  
Bonner Sphere Spectrometer

ausgeführt zum Zwecke der Erlangung des akademischen Grades  
*Doktorin der technischen Wissenschaften*  
unter der Leitung von

O. Univ. Prof. Dr. Hannes Aigner  
Atominstitut der TU Wien

und

Dr. Marco Silari  
CERN, Schweiz

eingereicht an der Technischen Universität Wien  
Technisch-Naturwissenschaftliche Fakultät

von

Dipl.-Ing. Angela Mitaroff

Matrikelnummer e9125512  
Sonnleithnergasse 43/18  
A-1100 Wien

Genf, Dezember 2001

# Abstract

Stray radiation fields outside the shielding of hadron accelerators are of complex nature. They consist of a multiplicity of radiation components (neutrons, photons, electrons, pions, muons, ...) which extend over a wide range of energies. Since the dose equivalent in these mixed fields is mainly due to neutrons, neutron dosimetry is a particularly important task. The neutron energy in these fields ranges from thermal up to several hundreds of MeV, thus making dosimetry difficult.

A well known instrument for measuring neutron energy distributions from thermal energies up to about  $E=10$  MeV is the Bonner sphere spectrometer (BSS). It consists of a set of moderating spheres of different radii made of polyethylene, with a thermal neutron counter in the centre. Each detector (sphere plus counter) has a maximum response at a certain energy value depending on its size, but the overall response of the conventional BSS drops sharply between  $E=10$ -20 MeV.

*This thesis focuses on the development, the calibration and tests in various radiation fields of a new Bonner sphere spectrometer with an extended response function.*

First, two new Bonner spheres with a response up to  $E=2$  GeV were developed and built as a complement to a conventional BSS. This was achieved by an extensive Monte-Carlo (MC) simulation study performed with FLUKA on possible moderating materials and combinations of these materials. In this study particular care was taken to reliably estimate the uncertainties on the calculated response functions due to variations of the sphere diameter, the moderator density and the moderator thickness. MC simulations also pointed out that the old sphere supports made of plastics increase the neutron scattering and may therefore influence the count rate of the Bonner spheres. Thus, new sphere supports made of aluminium were designed and constructed.

The two new spheres were assembled with the conventional BSS into a new extended-range spectrometer. The new spectrometer was then calibrated at the Physikalisch-Technische Bundesanstalt (PTB) in Braunschweig, Germany, using monoenergetic neutron beams of  $E=144$  keV, 1.2 MeV, 5 MeV and 14.8 MeV. In

the following it was also tested with an  $^{241}\text{Am}$ -Be source in the CERN calibration laboratory and at CERF (CERN-EU high-energy reference field). The CERF facility is very well characterized and provides a broad neutron field from thermal energies up to several hundreds of MeV with a large relative contribution of 10-100 MeV neutrons. The tests in both fields showed that the simulations agreed with the measured values to an accuracy of better than 20%. This is perfectly adequate for the use in radiation protection.

In fact, the extended-range Bonner sphere spectrometer has not only demonstrated its advantages in routine measurements in this domain, but was also successfully employed in research work related to radiation protection. Thereby the superior performance of the new extended-range BSS as compared to the conventional one became clearly visible.

In addition to the work on the Bonner sphere spectrometer, preliminary Monte-Carlo studies aiming at an upgrade of CERF were performed in this thesis. It was shown that an optimized shielding configuration at CERF could produce a radiation field with higher intensities, higher energies and a higher relative neutron fluence as compared to the present set-up. This new reference field is of interest for forthcoming measurements related to the space programme and also for testing and calibrating the Bonner spheres at energies higher than what was possible in this thesis.

# Kurzfassung

Die Streustrahlung außerhalb der Abschirmung von Teilchenbeschleunigern für Hadronen ist sehr komplex. Sie besteht aus einer Vielzahl von Komponenten (Neutronen, Photonen, Elektronen, Pionen, Müonen, ...) und erstreckt sich über einen weiten Energiebereich. Da die Äquivalentdosis in diesen gemischten Strahlungsfeldern hauptsächlich von den Neutronen herröhrt, ist die Neutronendosimetrie dort von besonderer Bedeutung. Sie erweist sich aber oftmals als sehr schwierig, weil das Neutronenspektrum von thermischen Energien bis zu mehreren 100 MeV reicht.

Ein gebräuchliches Instrument zur Messung der Energieverteilung von Neutronen bis ca.  $E=10$  MeV ist das Bonnerkugel-Spektrometer (BKS). Es besteht aus einem Satz kugelförmiger Polyethylenmoderatoren unterschiedlicher Größe in deren Mitte sich ein Zähler für thermische Neutronen befindet. Jeder Detektor (Moderatorkugel + Zähler) hat, in Abhängigkeit von seiner Größe, ein maximales Ansprechvermögen bei einer ganz bestimmten Energie. Das Gesamtansprechvermögen des konventionellen BKS fällt jedoch bei Energien zwischen  $E=10-20$  MeV drastisch ab.

*Diese Arbeit konzentriert sich auf die Entwicklung eines neuen Bonnerkugel-Spektrometers mit erweitertem Ansprechbereich, sowie dessen Kalibrierung und der Durchführung von Tests in verschiedenen Strahlungsfeldern.*

Zu Beginn wurden zwei neue Bonnerkugeln mit einem Ansprechvermögen bis  $E=2$  GeV als Ergänzung zu einem konventionellen BKS entwickelt und gebaut. Dies wurde mit Hilfe umfangreicher Monte-Carlo (MC) Simulationen mit FLUKA erreicht, in denen zahlreiche mögliche Materialen für die Moderatoren und deren Kombinationen studiert wurden. Besonderer wurde dabei Augenmerk auf eine zuverlässige Abschätzung der Fehler des simulierten Ansprechvermögens gelegt, welche durch Abweichungen des Kugeldurchmessers, der Moderatorordichte und der Moderatordicke auftreten können. Weitere MC Simulationen zeigten auch, daß die alten Kugelhalterungen aus Plastik die Neutronenstreuung deutlich erhöhen und damit das Meßergebnis der Bonnerkugeln verfälschen können. Aus diesem Grund wurden neue Kugelhalterungen aus Aluminium entworfen und gebaut.

Die Eingliederung der zwei neuen Bonnerkugeln in das konventionelle BKS ergab ein neues BKS mit erweitertem Ansprechbereich. Das neue Spektrometer wurde in der Physikalisch-Technischen Bundesanstalt (PTB) in Braunschweig, Deutschland, mit monoenergetischen Neutronenstrahlen bei  $E=144\text{ keV}$ ,  $1.2\text{ MeV}$ ,  $5\text{ MeV}$  und  $14.8\text{ MeV}$  kalibriert. Des Weiteren wurde es mit einer  $^{241}\text{Am-Be}$  Quelle in der CERN Kalibrierhalle und bei CERF (CERN-EU high-energy reference field) getestet. CERF ist ein Referenzstrahlplatz mit sehr gut bekannten Parametern. Er bietet ein ausgedehntes Neutronenspektrum, welches von thermischen Energien bis zu einigen hundert MeV reicht und durch einen großen relativen Anteil von 10-100 MeV Neutronen charakterisiert ist. Die Tests in beiden Strahlungsfeldern haben gezeigt, daß die Simulationen mit einer Genauigkeit von 20 % sehr gut mit den Messungen übereinstimmen. Dies ist durchaus ausreichend für Anwendungen im Strahlenschutz.

In der Tat bewies das neue Bonnerkugel-Spektrometer mit erweitertem Ansprechbereich seine Vorteile nicht nur in Routinemessungen sondern auch in Forschungsarbeiten im Hinblick auf den Strahlenschutz. Dabei wurde die Überlegenheit des neuen BKS mit erweitertem Ansprechbereich gegenüber dem konventionellen BKS sehr deutlich.

Ergänzend zu der Arbeit am Bonnerkugel-Spektrometer wurden in dieser Dissertation vorläufige Monte-Carlo Studien mit dem Ziel einer Aufrüstung von CERF durchgeführt. Es wurde gezeigt, daß eine optimierte Abschirmung in CERF ein Strahlungsfeld erzeugen kann, welches höhere Intensitäten, höhere Energien und eine größere relative Neutronenfluenz aufweist. Dieser neue Referenzstrahlplatz wäre von Interesse für bevorstehende Messungen im Rahmen des Weltraumforschungsprogramms, aber auch für Tests und Kalibrierungen der Bonnerkugeln bei höheren Energien als jenen, die für diese Arbeit zur Verfügung standen.

# Contents

|          |   |          |
|----------|---|----------|
| <b>1</b> | <b>Neutron spectrometry</b>                               | <b>1</b> |
| 1.1      | History . . . . .   | 2        |
| 1.2      | Multisphere system spectrometry . . . . .                 | 3        |
| <b>2</b> | <b>Motivation for an extended-range BSS</b>               | <b>5</b> |
| <b>3</b> | <b>The Monte-Carlo code FLUKA</b>                         | <b>7</b> |
| 3.1      | History of FLUKA . . . . .                                | 7        |
| 3.2      | Particle transport in matter . . . . .                    | 8        |
| 3.3      | Geometry in FLUKA . . . . .                               | 9        |
| 3.4      | Tracking . . . . .  | 10       |
| 3.5      | Scoring . . . . .   | 10       |
| 3.6      | Biassing . . . . .  | 10       |
| 3.7      | Models used in FLUKA . . . . .                            | 11       |
| 3.7.1    | Simulation of hadronic cascades in FLUKA . . . . .        | 11       |
| 3.7.1.1  | Inelastic nuclear interactions . . . . .                  | 11       |
| 3.7.1.2  | Elastic nuclear interactions . . . . .                    | 12       |
| 3.7.1.3  | Low-energy neutrons . . . . .                             | 12       |
| 3.7.2    | Simulation of electromagnetic cascades in FLUKA . . . . . | 13       |
| 3.7.2.1  | Transport of charged hadrons and muons . . . . .          | 13       |
| 3.7.2.2  | EMF: Electro-Magnetic FLUKA . . . . .                     | 13       |

|   |           |
|---|-----------|
| <b>4 Unfolding procedures</b>                                   | <b>14</b> |
| 4.1 GRAVEL . . . . .  | 15        |
| 4.2 MAXED . . . . .   | 16        |
| <b>5 MC simulated detector responses</b>                        | <b>17</b> |
| 5.1 The conventional Bonner sphere set . . . . .                | 17        |
| 5.2 Simulation set-up . . . . .                                 | 18        |
| 5.3 Design study of the new extended-range BSS . . . . .        | 20        |
| <b>6 The extended-range BSS</b>                                 | <b>27</b> |
| 6.1 Stanlio and Ollio . . . . .                                 | 28        |
| 6.2 The new extended-range Bonner sphere set . . . . .          | 28        |
| 6.2.1 Factors influencing the response functions . . . . .      | 30        |
| 6.2.1.1 Geometry effects . . . . .                              | 31        |
| 6.2.1.2 Density uncertainties . . . . .                         | 34        |
| 6.2.1.3 Diameter uncertainties . . . . .                        | 38        |
| 6.2.2 Estimate of the response function uncertainties . . . . . | 40        |
| 6.3 The ${}^3\text{He}$ proportional counter . . . . .          | 42        |
| 6.3.1 Fundamentals . . . . .                                    | 42        |
| 6.3.2 Intercalibration . . . . .                                | 45        |
| 6.4 Electronics . . . . .                                       | 46        |
| 6.5 Sphere support . . . . .                                    | 48        |
| <b>7 Calibration with neutron beams</b>                         | <b>52</b> |
| 7.1 Experimental set-up . . . . .                               | 52        |
| 7.2 Background measurements . . . . .                           | 56        |
| 7.3 Data analysis and results . . . . .                         | 61        |
| 7.4 Comparison of simulated to measured response . . . . .      | 62        |
| <b>8 Measurements with sources</b>                              | <b>70</b> |

|           |  |            |
|-----------|--|------------|
| 8.1       | Experimental set-up  | 70         |
| 8.2       | Results  | 70         |
| <b>9</b>  | <b>Measurements in reference fields</b>                                | <b>74</b>  |
| 9.1       | H6 area  | 74         |
| 9.2       | CERF beam monitor  | 76         |
| 9.2.1     | Performance tests of the CERF beam monitor                             | 77         |
| 9.2.1.1   | Stabilisation tests  | 77         |
| 9.2.1.2   | Noise  | 78         |
| 9.2.1.3   | Linearity tests  | 78         |
| 9.2.1.4   | Leakage currents   | 79         |
| 9.2.1.5   | Region of ion saturation   | 80         |
| 9.2.2     | Recombination losses of the CERF beam monitor operating in the H6 beam | 82         |
| 9.2.3     | Calibration of the CERF beam monitor                                   | 83         |
| 9.2.3.1   | Experimental set-up  | 84         |
| 9.2.3.2   | Measurements   | 85         |
| 9.2.3.3   | Analysis   | 86         |
| 9.2.3.4   | Comparison with the low-intensity measurements                         | 88         |
| 9.3       | Experimental set-up  | 89         |
| 9.4       | Background measurements  | 92         |
| 9.5       | Data analysis and results  | 94         |
| 9.6       | Upgrade of CERF  | 104        |
| <b>10</b> | <b>Summary and conclusions</b>   | <b>112</b> |
| <b>A</b>  | <b>Quantities in radiological protection</b>                           | <b>115</b> |
| A.1       | Introduction   | 115        |
| A.2       | Physical quantities  | 116        |
| A.3       | Protective quantities  | 117        |

|   |            |
|---|------------|
| A.4 Operational quantities . . . . .    | 117        |
| A.4.1 Area monitoring . . . . .         | 118        |
| A.4.1.1 Individual monitoring . . . . . | 118        |
| A.5 Correlated quantities . . . . .     | 118        |
| <b>B Cross sectional views</b>          | <b>120</b> |
| <b>C Response function data</b>         | <b>125</b> |
| <b>D Technical specifications</b>       | <b>128</b> |
| <b>Bibliography</b>                     | <b>131</b> |
| <b>Acknowledgements</b>                 | <b>137</b> |
| <b>Curriculum Vitae</b>                 | <b>139</b> |

# Chapter 1

## Neutron spectrometry

*These results [...] are very difficult to explain on the assumption that the radiation from beryllium is a quantum radiation [...]. The difficulties disappear, however, if it be assumed that the radiation consists of particles of mass 1 and charge 0, or neutrons.<sup>1</sup>*

The discovery of the neutron was based on “Beryllium rays” knocking out atoms from various targets and measuring the energies of the resulting recoiling nuclei [Cha32]. Since 1932 neutron spectrometry has contributed much to the development of nuclear physics and has also become an important tool in several other fields, notably nuclear technology, fusion plasma-diagnostics, radiotherapy and radiation protection.

Methods of neutron spectrometry can be classified basically into seven groups based on the principle used to sense or measure neutron energy:

- Spectrometry of recoil nuclei after scattering with a neutron,
- Measurement of the energy of charged particles released in neutron induced reactions,
- Measuring the velocity of the neutron with the time-of-flight method,
- Threshold methods in which the minimum neutron energy is indicated by the appearance of a neutron-induced effect, such as radioactivity or a specific gamma-ray energy,

---

<sup>1</sup>James Chadwick: *Possible Existence of a Neutron*. Nature, Feb. 27, 1932, p. 312.  
In 1935 J. Chadwick received the Noble prize for the discovery of the neutron.

- Methods in which the neutron energy distribution is determined by unfolding (deconvoluting) a set of readings of detectors which differ in the energy-dependence of their response to neutrons,
- Methods based on neutron diffraction,
- Methods measuring the time distribution of the slowing down of a short burst of high-energy neutrons in a suitable medium.

## 1.1 History

Three main periods can be identified in the evolution of neutron spectrometry: 1932-1959, 1960-1979 and 1980-now.

Most neutron spectrometers used today are based on methods that were introduced before 1960. Recoil spectrometers in use by 1960 included ionization chambers and proportional counters, cloud chambers, nuclear emulsions, organic scintillators, recoil telescopes and double-pulse (capture-gated) neutron spectrometers. Neutron spectrometers based on measuring the energies of charged reaction products included the  $^3\text{He}$  proportional counter and the  $^6\text{Li}(\text{Eu})$  scintillator crystal. Time-of-flight methods and threshold activation methods were also prominent during this period.

Notable developments during the second phase, 1960-1979, were the introduction of the Bonner sphere method [Bra60], the advances made in neutron spectrometry techniques based on gaseous ionization detectors [Gro79] and scintillation detectors [Har79]. An associated important development was the advent of computer based unfolding methods for determining neutron spectra from few and multichannel measurements [Har79, Ver68, McE67, Per78]. Other notable developments during this period were the first applications of semiconductor detectors to neutron spectrometry [Dea63] and the introduction of the super-heated drop ('bubble') detector [Apf79].

The third (post 1979) phase also brought considerable technological progress but will probably be remembered most for the impact of computers on neutron spectrometry. In particular, neutron spectrometry has improved as a result of the comprehensive calculation methods that are now available, firstly to generate the response functions or to calculate the neutron detection efficiency of the detector system, *e.g.* by Monte-Carlo simulations, and secondly to unfold (deconvolute) the spectral neutron fluence from the spectrometer readings. The response matrix, which summarizes the detector responses as a function of incident neutron energy, provides the basis for this unfolding process. To date, response matrices are mostly based on calculations which must be validated by experimental

measurements. One of the most important measures of the quality of a neutron spectrometer is the degree to which the response matrix is known and understood.

## 1.2 Multisphere system spectrometry

The prototype multisphere system was the neutron spectrometer introduced by Bramblett, Ewing and Bonner in 1960 [Bra60], which subsequently became known as the Bonner sphere spectrometer (BSS). The original BSS comprised a small thermal neutron detector (cylindrical  ${}^6\text{LiI}(\text{Eu})$  crystal,  $d=4$  mm,  $h=4$  mm), positioned at the centre of a polyethylene sphere. Five spheres of different diameters between  $d=5.08$  cm (=2 inch) and  $d=30.48$  cm (=12 inch) were used to produce five detector systems with distinctly different response functions (Figure 1.1). The structure of the Bonner spheres is almost spherical, thus providing an isotropic response. For a small sphere the degree of moderation is small, as is the capture of thermal neutrons in the moderator. Low-energy neutrons thus have a reasonable probability of arriving at the thermal sensor and being detected, whereas fast neutrons tend to escape. For larger spheres there is considerably more moderation. There is also more capture which means that low-energy neutrons tend to be absorbed in the polyethylene. It is the high-energy neutrons which thus have the greatest probability of being detected in the thermal detector and the response function peaks in the high-energy region.

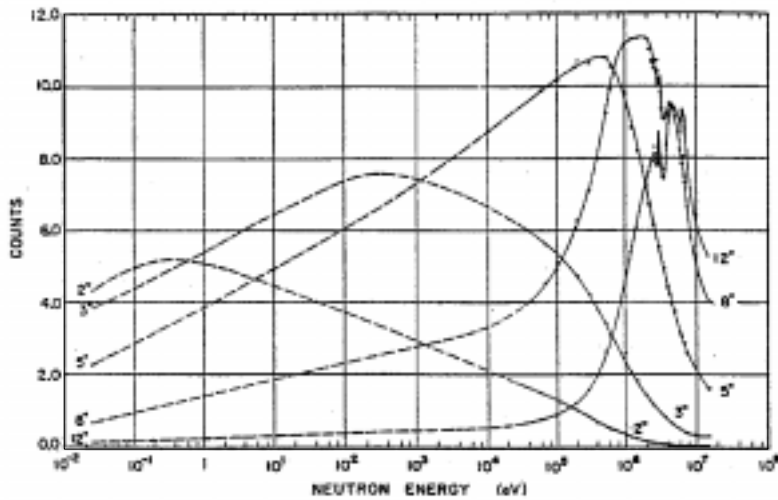


**Figure 1.1:** Response functions of the original Bonner sphere spectrometer, showing the count rate of the  ${}^6\text{LiI}(\text{Eu})$  scintillation crystal detector ( $d=4$  mm,  $h=4$  mm) as a function of neutron energy for five different polyethylene sphere diameters between  $d=5.08$  cm (=2 inch) and  $d=30.48$  cm (=12 inch) [Bra60].

If sphere  $i$  has a response function  $R_i(E)$ , and is exposed to a neutron field with spectral fluence  $\Phi(E)$ , then its reading  $x_i$  is obtained mathematically by folding  $R_i(E)$  with  $\Phi(E)$ , *i.e.:*

$$x_i = \int_0^{\infty} R_i(E) \Phi(E) dE. \quad (1.1)$$

Good approximations to  $R_i(E)$  can be obtained from calculations supported by measurements or calibrations with well characterized monoenergetic neutrons, radionuclide sources and other calibration fields. To determine an unknown neutron spectrum the count rate for each Bonner sphere is measured and then unfolded using the response matrix. Many unfolding codes have been developed over the years, based on several different techniques, such as least-squares adjustments, genetic algorithms or maximum entropy methods. The unfolding procedures used for this work are discussed in more detail in Chapter 4.

## Chapter 2

# Motivation for an extended-range Bonner sphere spectrometer

The aim of this work was to develop, to calibrate and to test in various fields a new Bonner sphere spectrometer with an extended range. Two new Bonner spheres with a response up to  $E=2$  GeV were developed as a complement to a conventional BSS. This was achieved by an extensive Monte-Carlo study on possible new moderating materials and combinations of these materials.

A conventional BSS, as presented in Chapter 1, consisting of only polyethylene moderators and a thermal neutron detector, has an inherent upper energy limit around  $E=10$ - $20$  MeV due to decreasing  $(n, p)$  cross sections with increasing neutron energy. Thus response functions of Bonner spheres with even large moderators peak near  $E=10$  MeV and quickly drop at higher energies. In addition, the shape of the response curves in the high-energy region are very similar, which makes resolving spectral shapes above  $E=20$ - $30$  MeV more difficult. In typical high-energy neutron fields the signal from even the larger spheres is dominated by neutrons below  $E=20$  MeV, and the signal from high-energy neutrons may not be distinguished from the expected signal fluctuations. As a consequence, such systems are unreliable in environments with a large contribution of high-energy neutrons. However, high-energy neutrons dominate the dose equivalent outside the shielding of hadron accelerators because they are the most penetrating component which has also a large fluence to ambient-dose-equivalent conversion coefficient<sup>1</sup>.

The design of the two new Bonner spheres, finally called *Stanlio* and *Ollio*, was done by performing MC simulations with the particle transport code FLUKA, which is the state-of-the-art MC programme for shielding purposes in high-energy physics. The studies followed a similar approach adopted in the development of

---

<sup>1</sup>A definition of the dose quantities used in radiation protection can be found in Appendix A.

the extended-range rem counter LINUS [Bir98a]. But in contrast to other groups [Vyl97, Mar01, Wie01] it was chosen to develop Bonner spheres with completely different shapes of response functions as compared to that of LINUS.

After construction, the new extended-range spectrometer was calibrated at the Physikalisch-Technische Bundesanstalt (PTB) in Braunschweig, Germany using monoenergetic neutron beams and was tested at CERN, Switzerland, with radioactive sources and in the ‘CERN-EU high-energy reference field’ (CERF) facility.

At CERN the extended BSS is presently used in radiation protection for routine measurements in high-energy neutron fields such as around the present accelerators and for experiments related to shielding studies. For the future the extended BSS will become essential to verify the correct operation of the dose monitors installed around the Large Hadron Collider LHC, where a large amount of high-energy neutrons will be present.

# Chapter 3

## The Monte-Carlo code FLUKA

The Monte-Carlo (MC) method is a method of approximately solving complex problems in mathematics and physics by simulating the problem using random numbers. These random numbers follow probability distributions based on sophisticated models. The name and the systematic development of Monte-Carlo methods dates from about 1944. The real use of MC methods as a research tool stems from work on the atomic bomb during the second world war. Nowadays the MC method has found widespread application in different disciplines *e.g.*: nuclear engineering, astrophysics, radiative heat transfer, aerospace engineering, chemistry, biology, medical physics, health physics, electrical engineering, mathematics, environmental engineering, economics and business modelling.

### 3.1 History of FLUKA

Early versions of hadron cascade Monte-Carlo codes, which finally became the FLUKA code of today, have existed already since 1964 [Ran64, Ran66]. The code was originally non-analog<sup>1</sup> and was used as a tool for designing the shielding of high-energy proton accelerators. The need to develop the fully analog<sup>2</sup> FLUKA (FLUktuierende KAskade) arose from an application to evaluate the performance of NaI crystals as hadron calorimeters [Ran70], where it was necessary to describe fluctuations in energy deposition using purely analog MC methods.

Since that time FLUKA has been continuously improved and extended by an international collaboration of physicists. It is now a multi-purpose MC code which is capable of simulating all components of particle cascades in matter from

---

<sup>1</sup>In the non-analog MC method the probability of special physical processes is modified. These modification techniques are called biasing techniques (see Section 3.6).

<sup>2</sup>In analog MC methods the probability of a process equals the real one.

TeV energies down to the energy of thermal neutrons. Its predictive power was established on a large number of studies benchmarking FLUKA results against experimental data (see [Fer95, Col00] and references therein).

This chapter gives a brief overview of the main physical concepts and models implemented in the versions of FLUKA [Fas01a, Fas01b] used in the simulations of this thesis (FLUKA98, FLUKA99 and FLUKA2000). The programme is coded in FORTRAN.

## 3.2 Particle transport in matter

FLUKA is a three dimensional Monte-Carlo particle transport programme, which simulates particle cascades in user-defined surroundings. One of the big advantages of FLUKA as compared to other MC transport codes is the ability to simulate transport of hadrons, muons, electrons, photons and low-energy neutrons in a single run and without interfacing different codes. All the secondaries issued from the same primary particle are transported before a new primary particle is started. Table 3.1 lists all the particles of which transport and interaction can be simulated with FLUKA.

**Table 3.1:** List of particles which can be transported by FLUKA.

| Leptons  |          |            |                  | Hadrons          |                  |                  |                 |
|----------|----------|------------|------------------|------------------|------------------|------------------|-----------------|
| $e^-$    | $e^+$    | $\nu_e$    | $\bar{\nu}_e$    | $p$              | $\bar{p}$        | $n$              | $\bar{n}$       |
| $\mu^-$  | $\mu^+$  | $\nu_\mu$  | $\bar{\nu}_\mu$  | $\pi^+$          | $\pi^-$          | $\pi^0$          |                 |
| $\tau^-$ | $\tau^+$ | $\nu_\tau$ | $\bar{\nu}_\tau$ | $K^+$            | $K^-$            | $K_l^0$          | $K_s^0$         |
| Photons  |          |            |                  | $K^0$            | $\bar{K}^0$      | $K^0$            | $\bar{K}^0$     |
|          |          |            |                  | $\Omega^+$       | $\Omega^-$       |                  |                 |
|          |          |            |                  |                  |                  | $\Lambda$        | $\bar{\Lambda}$ |
|          |          |            |                  | $\Sigma^+$       | $\Sigma^-$       | $\Sigma^0$       |                 |
|          |          |            |                  | $\bar{\Sigma}^+$ | $\bar{\Sigma}^-$ | $\bar{\Sigma}^0$ |                 |
|          |          |            |                  | $\Xi^+$          | $\Xi^-$          | $\Xi^0$          | $\bar{\Xi}^0$   |

In contrast to many other particle transport programmes FLUKA can simulate most transportation and production aspects from PeV scales to very low energies depending on the particle. The energy ranges for the transport and interaction of the most important particles are given in Table 3.2.

**Table 3.2:** Energy ranges for interaction and transport of the most important particles in FLUKA.

| Particles                     | Transport limits | Limits for primary particles |
|-------------------------------|------------------|------------------------------|
| Charged hadrons               | 1 keV-20 TeV     | 100 keV-20 TeV               |
| $n$                           | thermal-20 TeV   | thermal-20 TeV               |
| $\bar{n}$                     | 50 MeV-20 TeV    | 100 MeV-20 TeV               |
| $\mu^\pm$                     | 1 keV-1000 TeV   | 100 keV-1000 TeV             |
| $e^\pm$ (for high-Z material) | 1 keV-1000 TeV   | 150 keV-1000 TeV             |
| $e^\pm$ (for low-Z material)  | 1 keV-1000 TeV   | 70 keV-1000 TeV              |
| $\gamma$                      | 1 keV-1000 TeV   | 7 keV-1000 TeV               |

### 3.3 Geometry in FLUKA

FLUKA uses a combinatorial geometry package which was originally developed at ORNL (Oak Ridge National Laboratory, USA) for the neutron and  $\gamma$ -ray transport programme MORSE [Emm75]. To this package additional geometry features, like infinite cylinders and planes, were added. Complex objects can be defined by using the Boolean operators union, difference and intersection.

A limited repetition capability (lattice capability) is now available which avoids the description of repetitive structures in all details. Thus, only one single module has to be defined, which can then be re-iterated as many times as required. In essence this allows to define geometries, containing up to thousands of different regions, by using only a small number of region and body definitions.

A geometry debugger detects double- or non-defined regions and provides the ability to plot selected sections through the geometry (derived from the PLOT-GEOM programme of the Ispra Joint Nuclear Research Centre [Jaa73]).

A programme package called FLUKACAD/PIPSICAD, which transforms the input file into an AutoCad script file, was recently developed [Vin00]. The produced script file can then be used to generate a 3-dimensional drawing of the FLUKA geometry in AutoCad, including all features of AutoCad like rendering, dimensioning, etc.. In addition, double- and non-defined regions can be found and plotted in a reliable and fast way. This package is also able to visualize particle tracks, as calculated by FLUKA, in three dimensions.

## 3.4 Tracking

An improved model for multiple scattering, derived from Molière's theory [Mol47, Mol48, Mol55] is used in FLUKA and has been extended to all charged particles [Fer91] during the past ten years. It also takes into account special high-energy effects, very grazing angles, correlations between lateral and longitudinal displacements and backscattering effects close to boundaries. Furthermore, the model contains a sophisticated algorithm for treating the boundary problem. This accurate tracking algorithm always calculates the distance to the nearest boundary, which allows an exact transport to region boundaries. With this procedure, material discontinuities can be properly treated in FLUKA. Boundary crossing points are identified precisely even in the presence of very thin layers. The combined effect of multiple scattering and magnetic fields is also included. In materials of low densities (gases) single scattering can be requested *e.g.* in cases of simulating interactions with residual gas in accelerator vacuum-chambers.

## 3.5 Scoring

The following quantities can be scored with pre-defined estimators or detectors:

- Particle fluence and current,
- Track-length of particles in defined volumes,
- Number of inelastic reactions in a defined volume,
- Amount of energy deposition in a volume,
- Produced residual nuclei,
- Angle dependent particle production yields.

## 3.6 Biasing

Powerful biasing techniques are available in FLUKA in order to increase the statistical significance of the results in phase-space regions which are otherwise not accessible by fully analog simulations. They include:

- Importance biasing at boundaries: according to the importance of the entered region and of the region where the particle is coming from, particles are killed or split.

- Russian roulette/splitting for hadronic interactions.
- Leading particle biasing: only the one particle which has the higher energy out of two is followed after an electron/positron or photon interaction.
- Weight windows: region, particle and energy dependent control of the statistical weight at collision points can be applied with this feature.
- Decay length biasing (Lambda biasing): the decay length of selected particles can be artificially reduced in order to improve statistics of daughter production in the desired regions.
- Interaction length biasing: the interaction length of selected particles in matter can be artificially reduced in selected materials forcing more interactions.
- Neutron non-analog absorption: the scattering-to-absorption ratio of low energy neutrons can be controlled by the user.
- Neutron biased down-scattering: accelerates or slows down neutron moderation in selected regions.

Whenever the number of particles or their parameters are artificially changed in the biasing, the particle weights are adjusted correspondingly, in order to reproduce the real physical situation in the results.

## 3.7 Models used in FLUKA

There are different models describing the interactions and transport in different energy ranges. In general one can split the simulation roughly into two parts. The first considers interactions which produce hadronic particles down to low energies. The second deals with particles produced in the electromagnetic cascade. The general principles of the models are described in the following. More detailed information on the models can be found in [Fas97, Fas01a, Fas01b] and references therein.

### 3.7.1 Simulation of hadronic cascades in FLUKA

#### 3.7.1.1 Inelastic nuclear interactions

An inelastic interaction is described in FLUKA as a multi-step process involving various models each of which acts in a different energy range. The interaction

of high-energy particles ( $4 \text{ GeV} < E < 20 \text{ TeV}$ ) with a nucleus is treated by the Dual Parton Model. The secondary particles from such an interaction propagate through nuclear matter of the same nucleus and may interact with the spectator nucleons. This procedure, including the subsequent de-excitation of the nucleus, is well known under the name 'Generalized Intra Nuclear Cascade Model'. The pertinent energy range is covered mainly by two models. The first, called NUCRIN, is responsible for the inelastic reactions between  $E=2.5 \text{ GeV}$  and  $4 \text{ GeV}$ . The second model which covers hadron interactions below  $E=2.5 \text{ GeV}$  is called PEANUT. Finally, the excited spectator nucleus may evaporate nucleons and light fragments and dissipate energy through photon emission. In FLUKA these processes are treated by models for evaporation, fragmentation and  $\gamma$ -de-excitation.

### 3.7.1.2 Elastic nuclear interactions

The elastic scattering mechanism of hadrons at nuclei can be very important if the target nucleus is small with respect to the impact parameter. The scattering is described in terms of the optical model [Wet81]. The optical potential is produced via a real and an imaginary part. The real part has a Woods-Saxon radial dependence. The imaginary contribution shows rather a periphery-peaked shape. The total elastic cross-section is parameterized by fits to experimental data.

### 3.7.1.3 Low-energy neutrons

Neutron interactions below  $E=19.6 \text{ MeV}$  are followed down to user-defined region dependent energy cut-offs which can be as low as thermal energies. The model used here resembles the one used in the neutron and  $\gamma$ -ray programme MORSE [Emm75].

In cooperation with the Italian ENEA laboratory it was made possible to establish cross-section data sets for more than 130 frequently used elements, materials and isotopes. These cross-section sets consist of 72 neutron energy groups (or 37 wider groups), gamma production data and kerma factors for energy deposition calculation. For many materials, data sets correlated with the temperature of  $T=87 \text{ K}$  are also available. The difference to the normal sets can be found in a reduced Doppler broadening of the cross-sections at thermal energies.

The transport is described by standard multigroup transport with photon and fission-neutron production. This model contains detailed kinematics of elastic scattering on hydrogen nuclei. Furthermore, the transport of proton recoils and protons from  $N(n, p)$  reactions is considered. Photons which are emitted after an

inelastic reaction or a neutron capture are not transported in accordance with the multigroup treatment. These particles are passed through the more accurate Electro-Magnetic FLUKA (EMF) package which performs continuous transport with respect to energy (see below).

In general, for nuclei (with the exception of hydrogen) kerma factors are employed to calculate energy deposition. In the case of hydrogen the recoiling protons are explicitly generated and transported.

### 3.7.2 Simulation of electromagnetic cascades in FLUKA

#### 3.7.2.1 Transport of charged hadrons and muons

Besides hadronic effects FLUKA has to deal also with electromagnetic influences on hadrons. In order to transport charged hadrons and muons from  $E=1000$  TeV down to  $E=1$  keV, FLUKA takes into account the following effects:

- Energy loss,
- Multiple Coulomb scattering,
- Pair production and Bremsstrahlung,
- Muon photo-nuclear interactions.

#### 3.7.2.2 EMF: Electro-Magnetic FLUKA

In FLUKA a detailed transport model for electrons, positrons and photons is available. This part, called Electro-Magnetic FLUKA (EMF), is based on the EGS4 code [Nel85]. For performing electromagnetic simulations concerning these particles, one has to produce the necessary material data tables using the programme 'PEMF'. PEMF is a pre-processor, which provides cross-sections by using a method introduced by Sternheimer, Seltzer and Berger [Sel85, Sel86]. A thorough discussion can be found elsewhere [Fas97, Fas01a].

# Chapter 4

## Unfolding procedures

Unfolding<sup>1</sup> the energy spectrum of particle radiation involves solving the basic system of linear integral equations:

$$x_i = \int_0^\infty R_i(E) \Phi(E) dE \quad (i = 1, \dots, M) \quad (4.1)$$

which represents the measuring process. The function  $\Phi(E)$  to be determined by the unfolding techniques may be a spectral particle fluence, often simply referred to as a spectrum. The  $x_i$  denote the data obtained from measurements, *e.g.* using the various Bonner spheres. The kernels  $R_i(E)$  are the response functions of the measuring system. The subscript  $i$  is related to the channel number, *i.e.* to the individual Bonner sphere of a set.

Equation 4.1 has no unique solution since a finite number of discrete measurements,  $M$ , cannot define a continuous function  $\Phi(E)$ . It can be therefore transformed approximately into a discrete linear matrix equation:

$$x_i = \sum_{j=1}^N R_i(E_j) \cdot \Phi(E_j) \quad (i = 1, \dots, M) \quad (4.2)$$

with the response matrix  $R$ , the group fluence vector  $\vec{\Phi} = (\Phi_1, \dots, \Phi_\nu, \dots, \Phi_N)^T$  and  $\Phi_\nu = \Phi(E_\nu)$ . The  $N$  components  $\Phi_\nu$  can be considered as average fluence values in the intervals between the energies  $E_\nu$  and  $E_{\nu+1}$ . Equation 4.2, too, has no unique

---

<sup>1</sup>The terms unfolding and deconvolution are used synonymous for determining the spectral distribution  $\Phi(E)$  from Equation 4.1.

solution for  $N > M$ . An unique exact solution of the discrete spectrum  $\Phi(E_\nu)$  of equation 4.2 only exists in the case of equal dimensions  $N = M$  and a non-singular response matrix  $R$ . However, in few-channel measurements as in Bonner sphere spectrometry, it would be desired to have  $N > M$  or, preferably, even  $N \gg M$  for maximum information on the whole spectrum. In this case, equation 4.2 becomes strongly underdetermined with an infinite manifold of possible solutions  $\Phi_\nu$ . A more sophisticated unfolding procedure is then required. There are some possibilities to overcome these difficulties. First, all the information available on the spectrum must be used within the unfolding algorithm. Sometimes a pre-calculated fluence vector  $\Phi_0$  is known, sometimes a smoothing condition for the fluence can be formulated. This *a priori* information ('guess spectrum') can be used to construct a solvable system of normal equations. Also, it is a *condition sine qua non* for the resulting fluence vectors to be non-negative for all particle energies.

A number of unfolding codes have been developed for solving the inversion problem; details may be found elsewhere [Mat01]. Here only the two unfolding codes, which were used in this work, are briefly described.

## 4.1 GRAVEL

A code based on the iterative formalism described in [Mat94] for the GRAVEL code has been developed in the MATLAB language by the Polytechnic of Milan. It takes advantage of the MATLAB capabilities for the I/O of data and results and for the graphical presentation of the results and other important quantities (*e.g.*  $\chi^2$ , total fluence, etc.) during the iterations.

The final energy distribution generally is obtained by minimizing the  $\chi^2$  value obtained by comparing the experimental and the reconstructed data. Moreover, in each iteration the modifications with respect to the starting  $N$  group fluences are also minimized, so as to be able to deal with underdefined problems, as in the case of Bonner spheres. Thus, the global minimization refers more properly to the so-called generalized  $\chi^2$ , which is the sum of the  $\chi^2$  value of the experimental data with the  $\chi^2$  resulting from the modifications of the  $N$  group fluences with respect to the values of the previous iteration.

The initial guess is a pure 1/E spectrum. If any information about the expected spectrum is known, for example from Monte-Carlo simulations, it can be used by the programme to improve the resolution of the final energy distribution. In order to avoid negative values of the group fluences, the minimization is performed on their logarithms instead.

## 4.2 MAXED

MAXED is an unfolding code written in FORTRAN based on ‘maximum entropy deconvolution’. It was developed at EML (Environmental Measurements Laboratory, DoE, USA) for use with multisphere neutron spectrometers [Reg99]. MAXED uses the maximum entropy principle to find a spectrum which fits the data within experimental errors in a mathematically rigorous, consistent and unbiased way.

The maximum entropy principle states that from all admissible spectra satisfying the set of constraints, *i.e.* the measurements, one should choose the one that maximizes the entropy  $S$  of the distribution

$$S = - \sum_i [f_i \ln(f_i/f_i^{DEF}) + f_i^{DEF} - f_i] \quad (4.3)$$

where  $f_i$  and  $f_i^{DEF}$  are the discretized output and default spectra. Any *a priori* information about the neutron spectrum is contained in the default spectrum. The information from the measurements is used to modify the default spectrum in order to produce an output spectrum that fits the data within the experimental uncertainties. If the data contains no information about a portion of the spectrum, the unfolded output for that portion of the spectrum will be the same as the default spectrum. The programme does not apply any smoothing procedure to the unfolded spectrum, and none is needed to get a smooth spectrum if the estimates of the experimental uncertainties are realistic. Since no smoothing is applied, MAXED preserves any structure in the default spectrum which is finer than the resolution of the spectrometer. MAXED also uses a process called ‘simulating annealing’ to assure that it finds the globally optimum solution.

# Chapter 5

## MC simulated detector responses

### 5.1 The conventional Bonner sphere set

The BSS presently used by the Radiation Protection group at CERN consists of a set of five moderating spherical shells made of polyethylene, having outer diameters of 81 mm, 108 mm, 133 mm, 178 mm and 233 mm, respectively. The smallest sphere can be surrounded by a cadmium shell of 1 mm thickness in order to absorb the thermal neutron component. The active part of the spectrometer is a spherical  ${}^3\text{He}$  proportional counter with a diameter of 33 mm located in the hollow centre of each sphere. In order to avoid intercalibration uncertainties the same counter is used for all the spheres. This procedure does not increase the measuring time, since the spheres should not be used simultaneously in order to avoid systematic errors due to the modification of the neutron spectrum by the polyethylene of nearby spheres.

Figure 5.1 shows the calculated response functions of the various detectors (moderator plus counter) as a function of energy. Each detector has a maximum response at a certain energy which depends on the moderator size. As one can see, the response of the various Bonner spheres decreases rapidly for energies above a few MeV. This is due to decreasing  $(n, p)$  cross sections with increasing neutron energy.

In order to be able to study the neutron spectra around hadron accelerators, where the high-energy neutron component is important, it was desirable to extend the response of the BSS to substantially higher energies. As it is shown by the results of extensive Monte-Carlo simulations in the following sections, simply taking a bigger polyethylene sphere is not sufficient to enhance the response at high energies. Thus more sophisticated solutions have to be found.

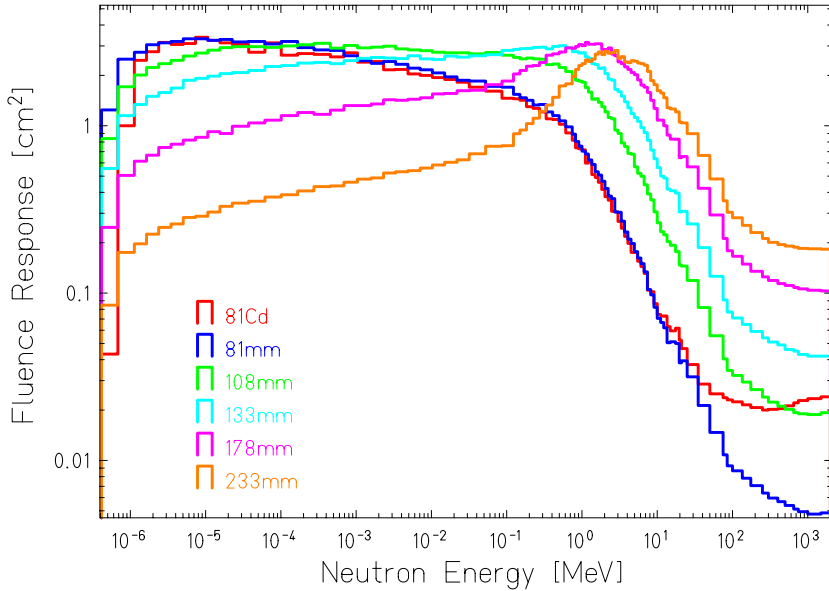


**Figure 5.1:** Absolute neutron fluence response (counts per unit fluence) of the five polyethylene spheres of the BSS. The spheres are labelled with their diameter in millimetres. The smallest sphere can be additionally surrounded by a cadmium shell (81Cd).

## 5.2 Simulation set-up

In order to reproduce correctly the measured responses by calculation and supplement them in energy ranges not measured, detailed information concerning the geometry of the moderator and the  $^3\text{He}$  counter is required. Figure 5.2 shows for example the geometry model which was constructed for the Monte-Carlo simulations of the 81 mm sphere. The sketch is a transverse section through the detector system. The geometry is symmetrical with respect to the stem of the  $^3\text{He}$  counter. The figure shows the proportional counter embedded in a moderator of diameter  $d=81$  mm made of polyethylene with a density of  $\rho=0.963$  g/cm $^3$ . The sensitive or effective volume of the  $^3\text{He}$  counter is a sphere with a diameter  $d=32$  mm, surrounded by a 0.5 mm thick aluminium wall. It is homogeneously filled with  $p=202.65$  kPa (=2 atm)  $^3\text{He}$  and  $p=101.325$  kPa (=1 atm) Krypton gas. The so-called nose is a short cylinder of aluminium and the stem is modelled as a long cylinder of aluminium with an air cavity inside. They are placed on opposite sides of the sensitive volume. The cable which connects the counter with the electronic devices was not taken into account in the simulations.

The simulations of all response functions presented in this chapter were performed with FLUKA98. The neutron response of each detector was calculated for 78 incident neutron energies: for the neutron energies of  $E=0.05, 0.1, 0.25, 0.5, 1$

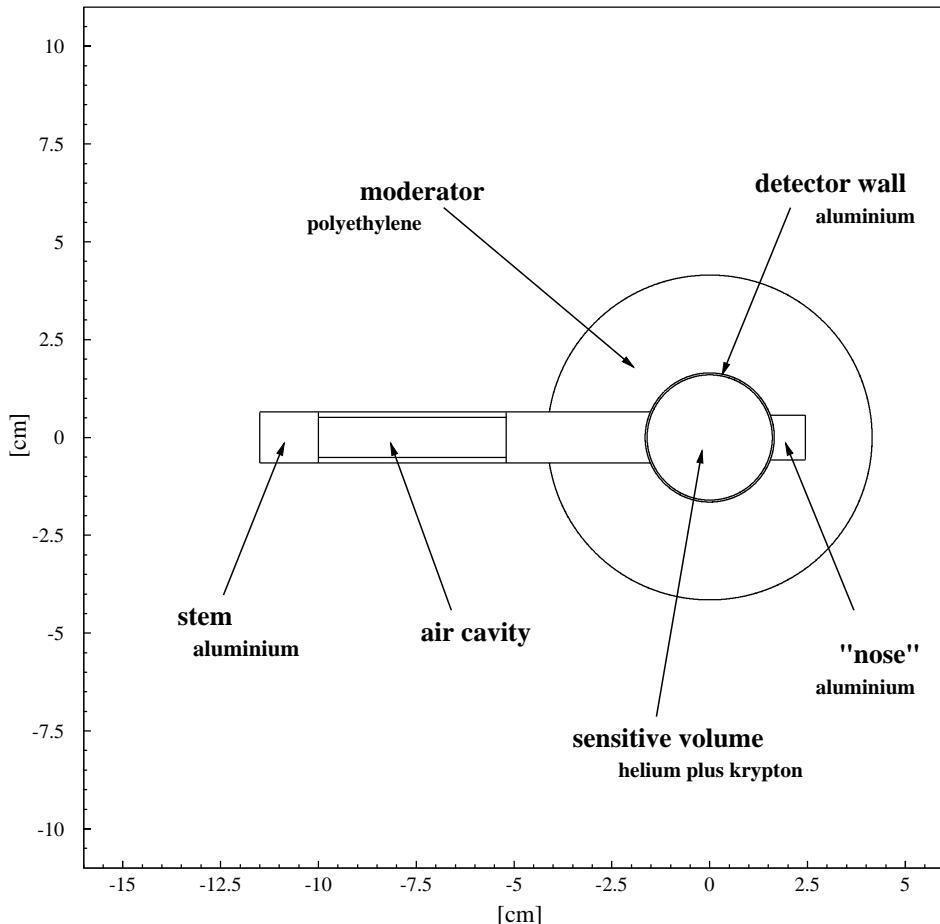


**Figure 5.2:** Geometry model of one of the Bonner spheres: a  ${}^3\text{He}$ -filled proportional counter, consisting of the sensitive volume, the so-called nose and the stem, is embedded in a moderator sphere made of polyethylene (the outer diameter of the smallest one is  $d=81$  mm). The geometry is symmetrical with respect to the stem of the  ${}^3\text{He}$  counter.

and 2 GeV, respectively, a broad parallel beam having a slightly larger extension than the sphere diameter was assumed. In most measurement conditions low-energy neutrons arise from down-scattering and are undirectional. Therefore an isotropic distribution of the incident neutrons was chosen for the 72 low-energy groups, between  $E=19.6 \times 10^6$  eV and  $1 \times 10^{-5}$  eV.

The model used for the Bonner spheres describes the sensitive volume of the proportional counter as an ideal sphere, the whole volume being homogeneously filled with a mixture of  ${}^3\text{He}$  and Kr gas with a ratio of partial pressure of 2:1. Effects

such as charge collection and gas amplification were not taken into consideration. Instead, it was assumed that each  ${}^3\text{He}(n, p)\text{t}$  event is registered and contributes to the reading of the Bonner sphere. The proton as well as the tritium contributes to the detector signal, their combined energy is  $E=764$  keV (Q-value) plus the kinetic energy of the incident neutron. The elastic cross-section can be neglected for the given problem.

The primary neutron fluence  $F_u$  is given in units of  $[1/\text{cm}^2]$  and thus the fluence response  $R$  in units of  $[\text{cm}^2]$ . The FLUKA calculations of  $R$  are realized in the following way: the track length - a standard output - in the sensitive volume of the  ${}^3\text{He}$  counter,  $\Delta x$ , is multiplied with the macroscopic cross-section of  ${}^3\text{He}$ ,  $\Sigma$ , yielding an expected number of counts, which is normalized to unit fluence of the primary neutrons,  $F_u$  (see equation 5.1):

$$R = \frac{\Delta x \cdot \Sigma}{F_u} \quad [\text{cm}^2] \quad (5.1)$$

This is done online by a user written routine, which is linked to the FLUKA libraries. The macroscopic cross-section  $\Sigma$  is defined as

$$\Sigma = \sigma \cdot N_{atom} \quad [\text{cm}^{-1}] \quad (5.2)$$

where  $\sigma$  is the microscopic cross-section given in  $\text{cm}^2$  and  $N_{atom}$  is the atomic density of the sensitive gas given by

$$N_{atoms} = \rho \cdot \frac{N_A}{A} \quad [\text{cm}^{-3}]. \quad (5.3)$$

The parameters  $\rho$ ,  $N_A$  and  $A$  are the density of the  ${}^3\text{He}$  gas  $[\text{g}/\text{cm}^3]$ , the Avogadro's number ( $6.023 \cdot 10^{23}$  atoms/mol) and the mass number  $[\text{g}/\text{mol}]$ , respectively.

### 5.3 Design study of the new extended-range BSS

In order to extend the range of the conventional Bonner sphere spectrometer by means of two new spheres, nineteen configurations of different sizes and materials were investigated by MC simulations. A cross-sectional view of all the detector configurations can be found in Appendix B.

As it can be seen from Figure 5.3, a simple increase of the diameter of the polyethylene sphere does not achieve the desired result. The response at high energies is slightly increased but it is still very similar to the one of the 233 mm sphere. More sophisticated solutions followed therefore an idea adopted in the

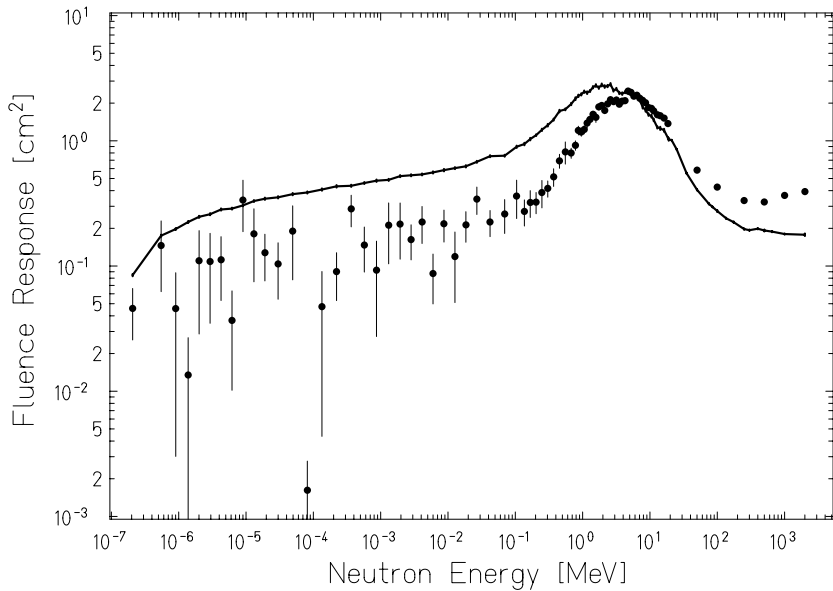


**Figure 5.3:** Calculated neutron fluence response (counts per unit fluence) of the 433 mm (20 cm thick polyethylene) sphere (symbols). The response of the 233 mm polyethylene sphere is plotted as reference (solid line).

development of the extended-range neutron rem counter LINUS [Bir98a], *i.e.* to add a high-Z material and a thermal neutron absorber, in our case cadmium, into a polyethylene moderator. The former does not influence very much the response to low-energy neutrons, but increases the response to high-energy ones via  $(n,xn)$  interactions. The latter absorbs thermal neutrons but does not affect high-energy neutrons.

In the first approach, a layer of either 1 cm of lead, 1 cm of iron, 1 cm of copper, 5 mm of iron, 3 mm of lead or 1 mm of cadmium was embedded into the polyethylene moderator of the 233 mm sphere at a radial distance from the  ${}^3\text{He}$  counter comparable to the configuration used for LINUS. The order of materials from the  ${}^3\text{He}$  proportional counter outwards is shown in Table 5.1. In order to optimize the shape of the response function of the new detectors, lead and cadmium were differently combined in a second approach and the thicknesses of the layers were modified or even completely omitted (Table 5.2).

**Table 5.1:** The order of materials (from the  ${}^3\text{He}$  proportional counter outwards) used in the first approach of the simulations in order to study the effects of different materials embedded into the 233 mm sphere.

| Inner shell | High-Z shell   | Outer shell |
|-------------|--|-------------|
| 3 cm PE     | 1 cm Pb<br>1 cm Fe<br>1 cm Cu<br>5 mm Fe<br>3 mm Pb<br>1 mm Cd | 7 cm PE     |

**Table 5.2:** The order of materials (from the  ${}^3\text{He}$  proportional counter outwards) used in the second approach of the simulations in order to optimize the shape of the desired response function of the two new detectors.

| Inner shell | High-Z shell                                    | Outer shell |
|-------------|---|-------------|
| 3 cm PE     | 1 mm Cd, 1 cm Pb                                | 7 cm PE     |
| 2 cm PE     | 1 mm Cd, 2 cm PE, 1.4 cm Pb                     | 5 cm PE     |
| 1 cm PE     |   |             |
| 2 cm PE     | 1 cm Pb   | 7 cm PE     |
| 3 cm void   |   |             |
| 3 cm PE     | 1 cm Pb<br>1 mm Cd, 1 cm Pb<br>1 mm Cd, 2 cm Pb |             |
| 1 cm PE     |   |             |
| 2 cm PE     | 1 cm Pb   |             |
| 1 cm PE     |   |             |
| 2 cm PE     | 1 mm Cd, 1 cm Pb                                |             |

Figures 5.4 - 5.7 show the results of the calculations for the configurations given in Table 5.1 and 5.2. They show the fluence response (counts per unit neutron fluence) as a function of the neutron energy. For comparison the response function of the largest conventional Bonner sphere (233 mm in diameter) is also plotted as a solid line in all graphs.

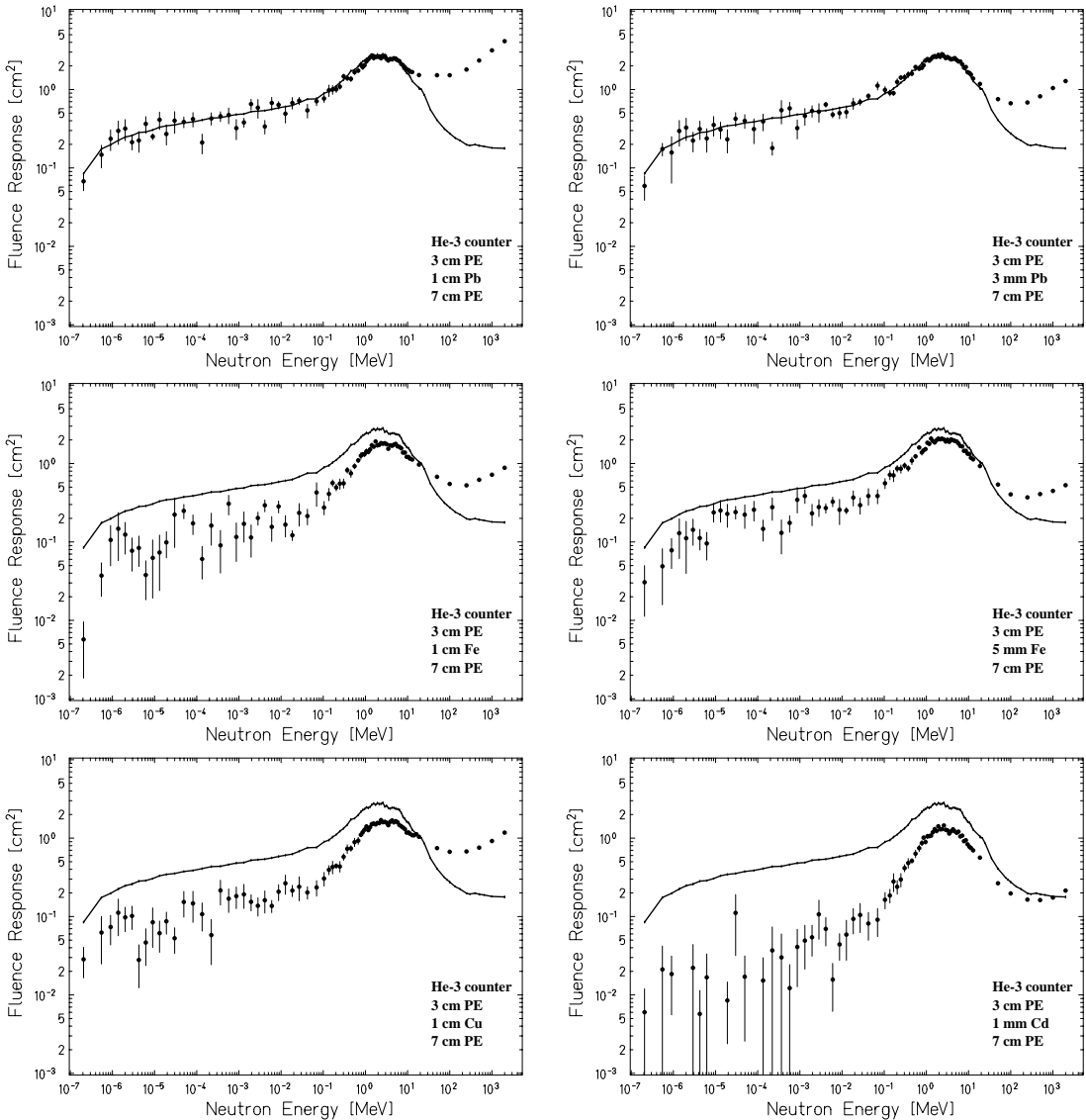


**Figure 5.4:** Calculated neutron fluence response (counts per unit fluence) using different materials embedded into the 233 mm polyethylene sphere (symbols). The response of the 233 mm polyethylene sphere is plotted as reference (solid line).

Figure 5.4 shows the results of the first approach, *i.e.* the investigation of different materials within shells of polyethylene. As expected, lead results in the largest response at high energies. Furthermore, 1 mm of cadmium inside the polyethylene decreases the response at low energies. These two effects can be obtained with the same sphere by combining both materials in two different ways (Figures 5.5 A and B). Both detector configurations increase the response to high-energy neutrons up to  $E=1$  GeV by more than one order of magnitude and suppress the response to incident neutrons with energies lower than  $E=10$  keV by about one order of magnitude as compared to the one of the 233 mm detector of the standard BSS. The configuration of the detector sphere in Figure 5.5 A has the advantage of being about 3 kg lighter than the one in Figure 5.5 B. The former was therefore selected as first additional detector to the conventional BSS and named *Ollio*.

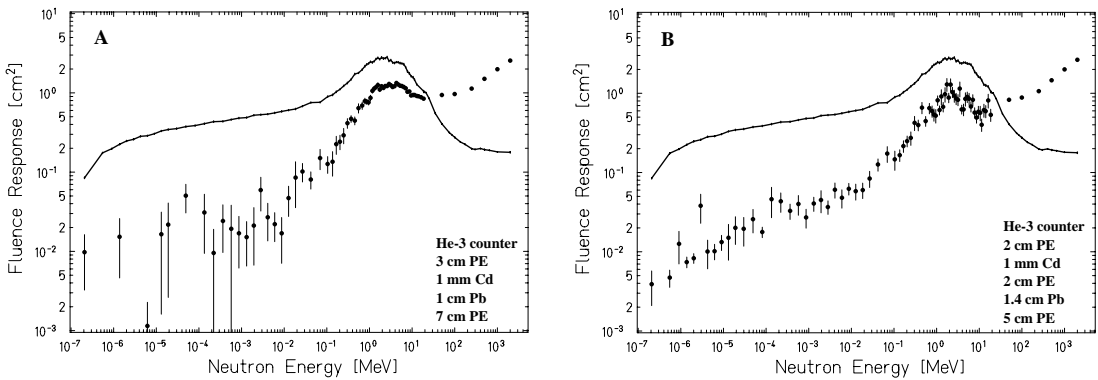


**Figure 5.5:** Calculated neutron fluence response (counts per unit fluence) for two different combinations of polyethylene, lead and cadmium (symbols). The configuration of Figure A was chosen as first additional sphere of the extended-range BSS and is called *Ollio*. The response of the 233 mm polyethylene sphere is plotted as reference (solid line).

The results of Figures 5.6 A, B and C were not satisfactory, since their responses do not differ significantly enough from the response of the 233 mm sphere. They were therefore not considered further.

In contrast, the response function in Figure 5.6 D shows a shape which was investigated more carefully. The lead shell outside yields the typical increase of response at high energies, but because of the small diameter ( $d=113$  mm) the detector behaves at low energies like a small Bonner sphere made of polyethylene. Furthermore a significant suppression of the peak at about  $E=10$  MeV can be observed. This fact sets this response function apart from the former ones and this configuration is therefore of interest for becoming the prototype of the second additional detector because it provides additional information.

A few variations of the geometry of this prototype were investigated in order to get an optimized ratio between the minimum at  $E\sim 10$  MeV and the high-

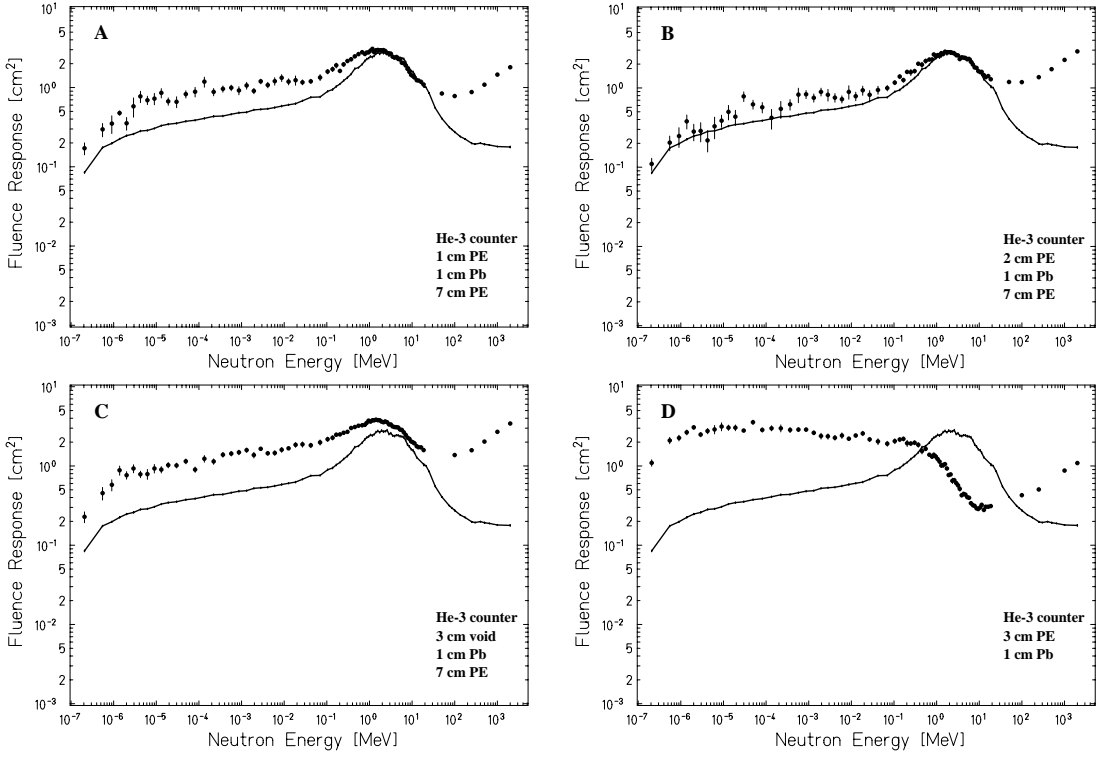


**Figure 5.6:** Calculated neutron fluence response (counts per unit fluence) for different shell thicknesses of polyethylene and lead (symbols). The configuration of Figure D with its different shape of the response function, becomes the prototype of *Stanlio*. The response of the 233 mm polyethylene sphere is plotted as reference (solid line).

energy behaviour (Figure 5.7). Figure 5.7 A shows also the advantage of having an additional cadmium layer inside the sphere. It decreases the response to thermal neutrons by more than a factor 10. The best result, where the peak at  $E \sim 10$  MeV of the response function is completely suppressed but the high-energy part significantly enhanced (Figure 5.7 F) could be obtained with the configuration made up, from the  ${}^3\text{He}$  proportional counter outwards, of 2 cm polyethylene, 1 mm cadmium and 2 cm lead. It became the second new Bonner sphere, named *Stanlio*. *Stanlio* together with *Ollio* seem to be a good addition to the existing BSS.

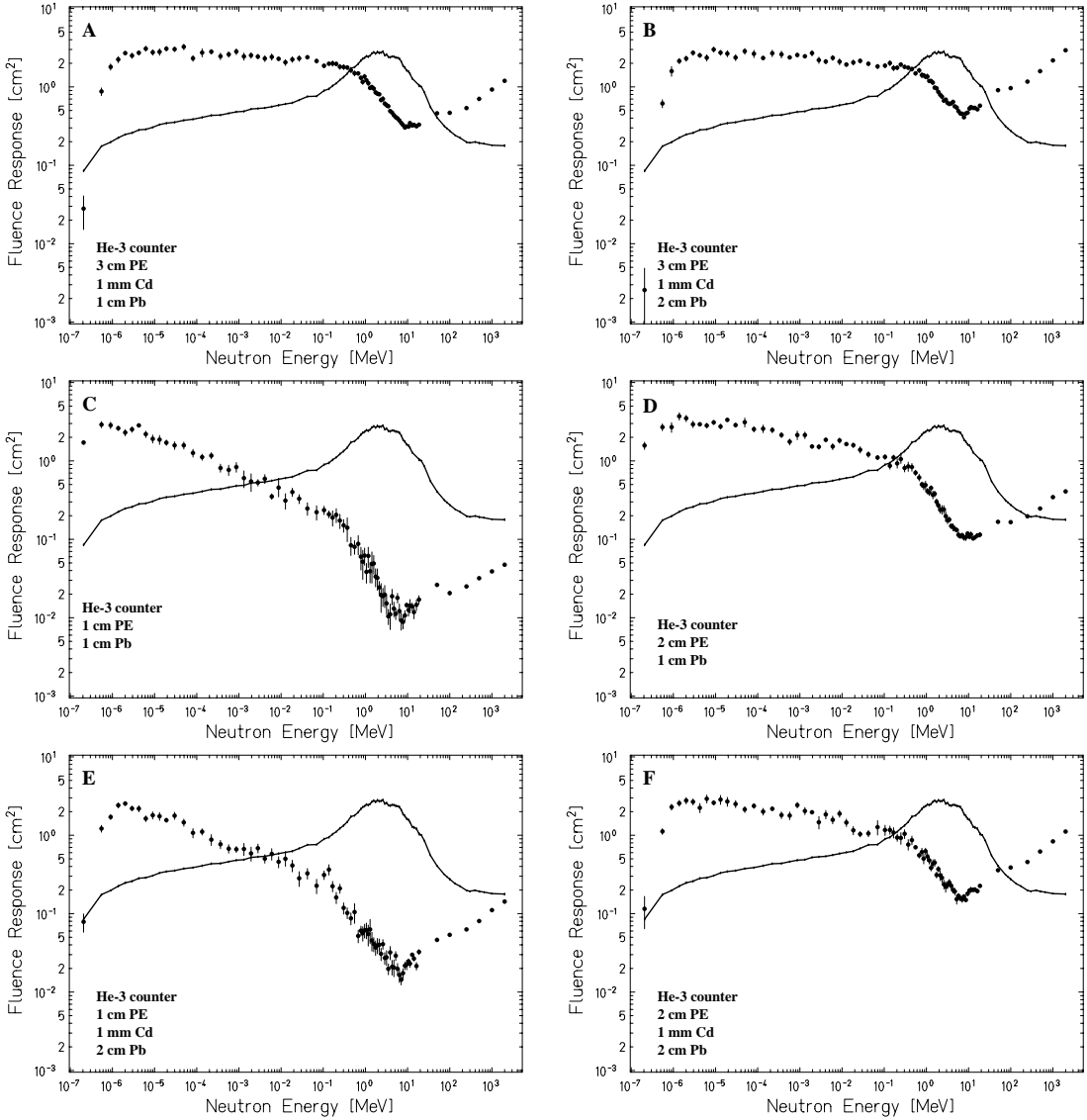


**Figure 5.7:** Calculated neutron fluence response (counts per unit fluence) of different variations of the prototype configuration of Stanlio (symbols). The configuration of Figure F was finally chosen as second additional sphere, called Stanlio. The response of the 233 mm polyethylene sphere is plotted as reference (solid line).

# Chapter 6

## The extended-range BSS

Figure 6.1 shows the various components of the new extended-range Bonner sphere spectrometer: the conventional BSS with moderators consisting of only polyethylene and a cadmium shell to surround the 81 mm sphere, the two new spheres *Stanlio* and *Ollio*, the filler pieces of the spheres, the  ${}^3\text{He}$  proportional

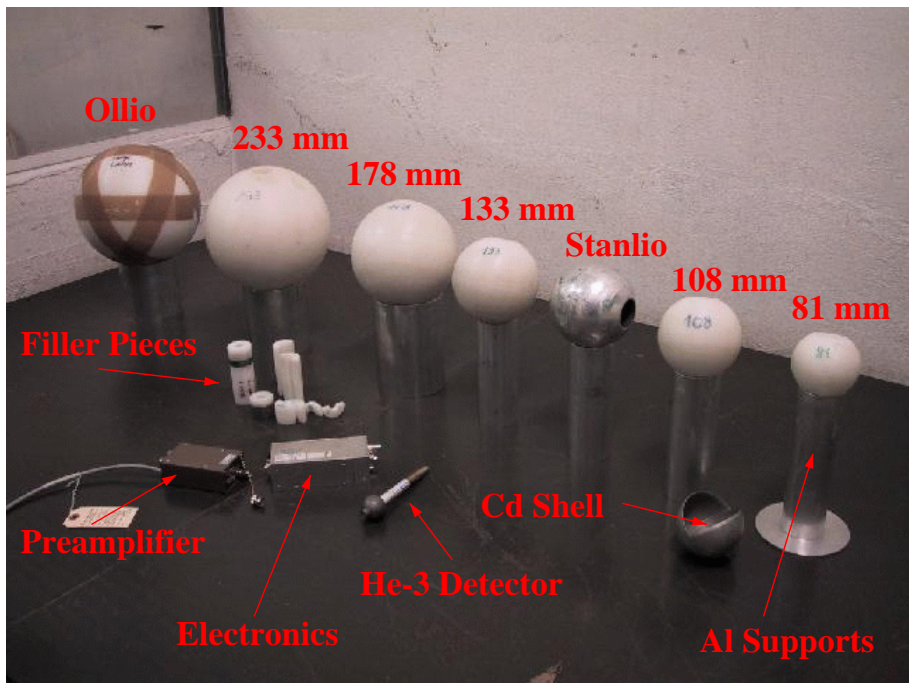


**Figure 6.1:** Components of the new extended-range Bonner sphere spectrometer: the conventional BSS with moderators consisting of only polyethylene and a cadmium shell to surround the 81 mm sphere, the two new spheres *Stanlio* and *Ollio*, the filler pieces of the spheres, the  ${}^3\text{He}$  proportional counter, the preamplifier, a compact electronic device and the Al supports.

counter, the preamplifier, a compact electronic device and the Al supports for the spheres. Details about the conventional BSS can be found in the previous chapter while the other components are described in detail in the following sections.

## 6.1 Stanlio and Ollio

The Monte-Carlo study of new detector responses (Chapter 5) resulted in two new detector designs, which were constructed as supplement to the conventional Bonner sphere spectrometer. The first, called *Stanlio*, has a diameter of 118.5 mm and weights  $\sim 7.75$  kg. The second, called *Ollio*, is a sphere with a diameter of 255 mm and  $\sim 12.62$  kg weight. The detailed parameters of the new spheres are presented in Table 6.1. The table shows the outer diameter of the  ${}^3\text{He}$  proportional counter, of the air-gaps and of the moderator layers of the two spheres.

**Table 6.1:** Geometrical parameters of the new spheres *Stanlio* and *Ollio*.

| Spheres | Outer radius [mm] |         |              |       |         |       |              |
|---------|-------------------|---------|--------------|-------|---------|-------|--------------|
|         | counter           | air-gap | polyethylene | Cd    | air-gap | Pb    | polyethylene |
| Stanlio | 16.5              | 17.25   | 38           | 39    | 39.25   | 59.25 | —            |
| Ollio   | 16.5              | 17.25   | 46.75        | 47.75 | 48      | 58.5  | 127.5        |

Figures 6.2 and 6.3 illustrate the arrangement of the different moderator layers around the  ${}^3\text{He}$  counter. The small air-gaps between the  ${}^3\text{He}$  counter and the polyethylene layer and between the cadmium and lead layers are not visible with the scale of these figures.

## 6.2 The new extended-range Bonner sphere set

Combining the calculated response functions of the conventional Bonner spheres with the ones of Stanlio and Ollio leads to the response matrix of the extended-range Bonner sphere set (Figure 6.4). For clarity, error bars are omitted in the figure. They are  $\sim 3$  % for the polyethylene spheres and about 6 % for Stanlio and Ollio. The original calculations of the responses above  $E=19.6$  MeV were performed at discrete energy values (see Chapter 5.2). In order to facilitate the further handling of the data (*e.g.*: for unfolding procedures, for comparison with experimental data, *etc.*), the discrete values were converted into binned responses. Figure 6.4 shows the well known shapes of conventional Bonner sphere response

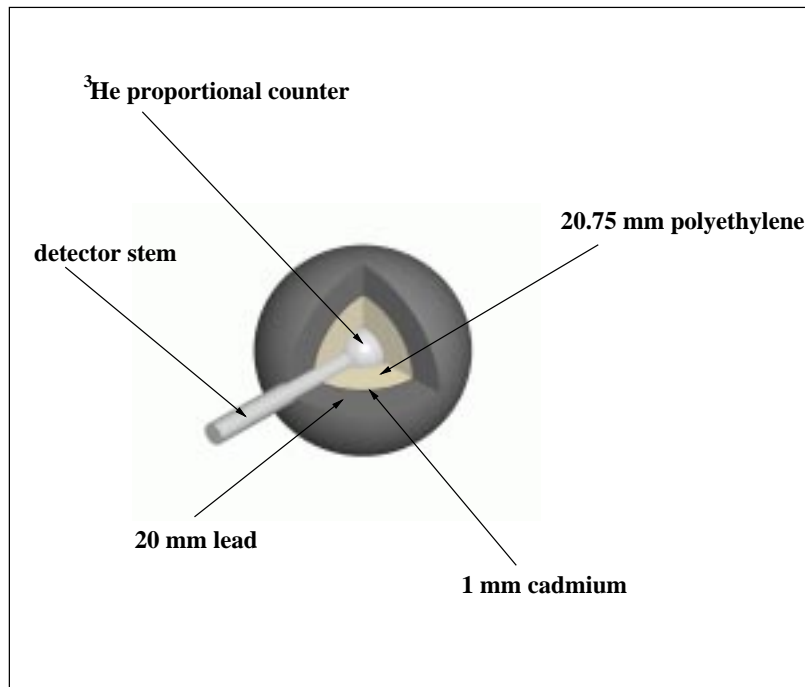


Figure 6.2: *Cut through the moderator of the new Bonner sphere Stanlio.*

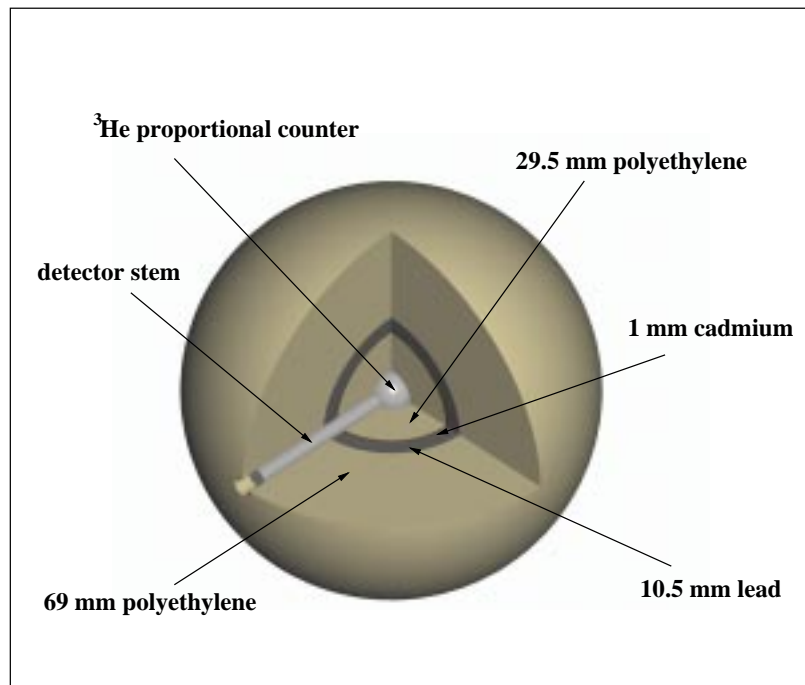
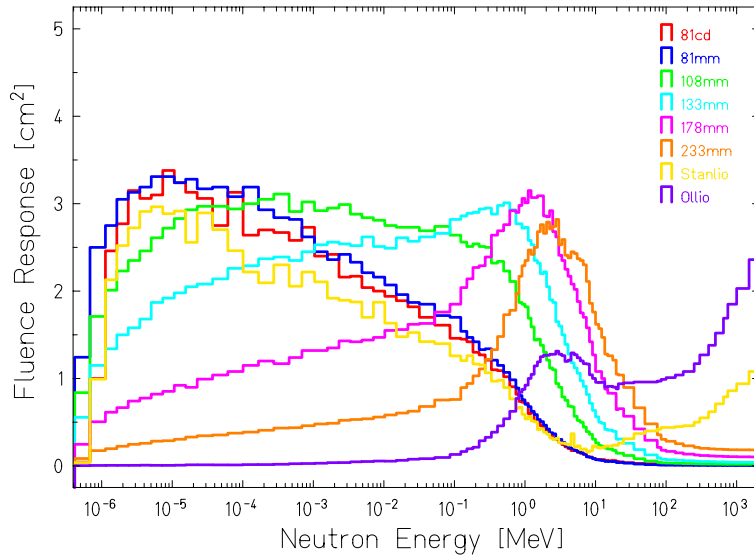


Figure 6.3: *Cut through the moderator of the new Bonner sphere Ollio.*



**Figure 6.4:** The absolute neutron fluence responses (counts per unit neutron fluence) of the extended-range Bonner sphere spectrometer. The conventional spheres made of polyethylene only are labelled with their diameters in mm. 81cd indicates the 81 mm sphere surrounded by 1 mm of cadmium. The two new, lead modified spheres are labelled with their names.

functions, *i.e.* the broad shape for the small spheres which gets with increasing diameter narrower and its maximum shifted to higher energies.

Stanlio and Ollio, the two spheres that contain lead shells, stand apart. Due to the  $Pb(n,xn)$  reaction, which starts playing an important role at  $\sim 10$  MeV, they show an increased response to neutrons with energies above  $E=10$  MeV as compared to the pure polyethylene spheres. At energies below  $E=10$  MeV the shapes of the response functions resemble the ones of the standard spheres of the corresponding sizes: Stanlio, a rather small sphere with a diameter of 118.5 mm, shows a broad response between  $E=1\times 10^{-6}$  MeV and  $1\times 10^{-1}$  MeV. Ollio, a large sphere with a diameter of 255 mm, has a narrow response peaking at a few MeV. It is worth noting that the response function of Stanlio shows a minimum where the responses of Ollio and the other large diameter spheres have a maximum. This feature makes Stanlio a good complement to the standard BSS.

### 6.2.1 Factors influencing the response functions

The calculated response functions shown above are for Bonner spheres with nominal parameters of density and geometry. In reality these parameters can differ from the nominal ones and thus cause uncertainties of the response functions of which the sources can be manifold. On the one hand there are some uncertain-

ties which are not directly assessable, like the exact internal geometry of the  $^3\text{He}$  proportional counter or its gas pressure. These are independent of the moderator thickness and composition and have been evaluated by calibration measurements (see Chapter 7). On the other hand response uncertainties due to variation in the geometry, the density and the thickness of the moderator are easier to quantify but depend strongly on the material and the size of the sphere. These are investigated in more detail in the following. The results obtained were used to estimate the uncertainty of the calculated response functions.

### 6.2.1.1 Geometry effects

Calibration measurements (Chapter 7) hinted that the true response functions, especially those of the small spheres (81 mm, 81Cd and Stanlio), show large discrepancies with respect to the calculated ones. It was found that a small air-gap of a few millimetres exists between the counter and the moderator that was not taken into account in the simulations. A precise measurement of the thickness and shape of the air-gap was not feasible. Thus, an air-gap with a constant thickness of 3.5 mm, which represents an upper limit of the real situation, was implemented in the FLUKA geometry. The calculations of the entire Bonner sphere set were then repeated. Figure 6.5 illustrates the geometrical approximations.

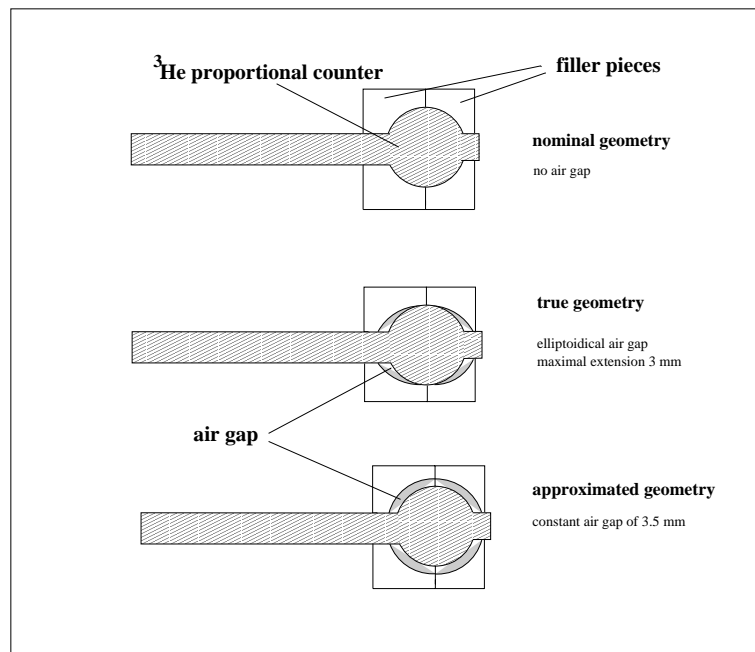


**Figure 6.5:** Illustration of the air-gap approximation. The top sketch shows the nominal geometry. The middle one sketches the geometry closest to reality. At the bottom the air-gap approximation used in the calculations is shown.

The deviation of the response functions including the air-gap versus the nominal response functions is shown in Figures 6.6- 6.9 for the 81 mm sphere, the 178 mm sphere, Stanlio and Ollio, respectively.

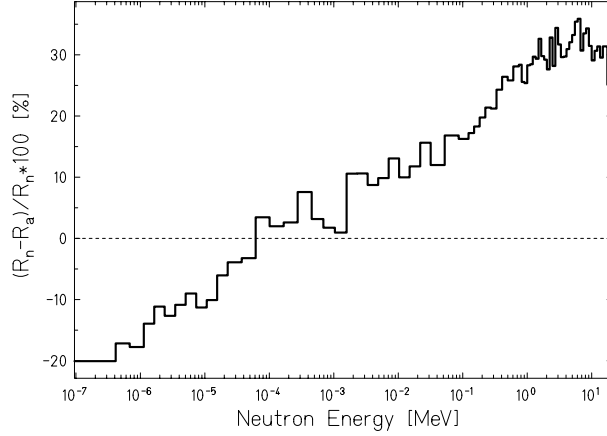


**Figure 6.6:** Relative variation of the nominal response of the 81 mm sphere without air-gap ( $R_n$ ) with respect to the response including an air-gap of 3.5 mm ( $R_a$ ).

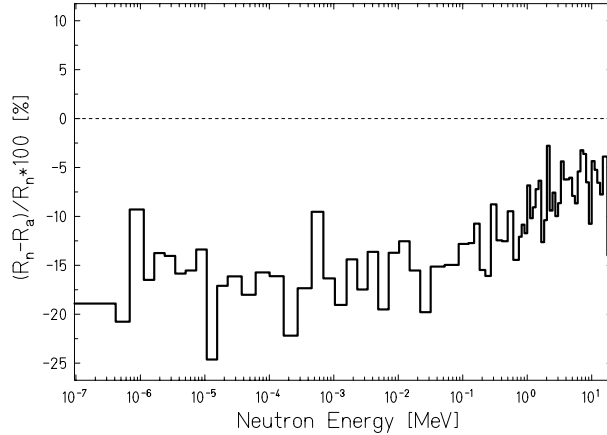


**Figure 6.7:** Relative variation of the nominal response of the 178 mm sphere without air-gap ( $R_n$ ) with respect to the response including an air-gap of 3.5 mm ( $R_a$ ).

Obviously the 81 mm sphere is the most sensitive one to such variations: the replacement of 3.5 mm polyethylene by air constitutes a 15 % reduction in the polyethylene thickness and thus of moderating material. Therefore this Bonner sphere is more sensitive to low-energy neutrons and less sensitive to intermediate and high-energy neutrons above  $\sim 1$  keV. The difference in the response is large and ranging from -20 % up to +30 %. For the 178 mm sphere the effect of the

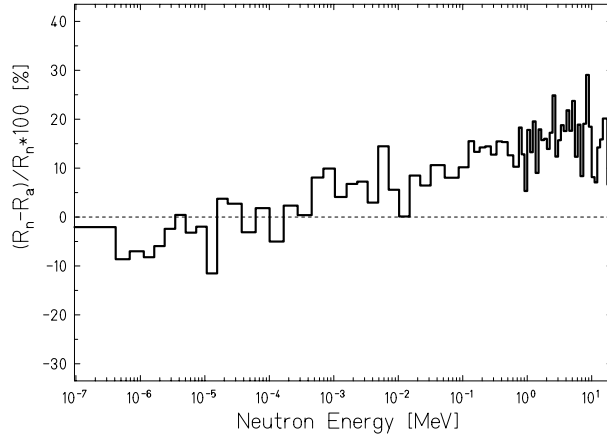


**Figure 6.8:** Relative variation of the nominal response of Stanlio without air-gap ( $R_n$ ) with respect to the response including an air-gap of 3.5 mm ( $R_a$ ).

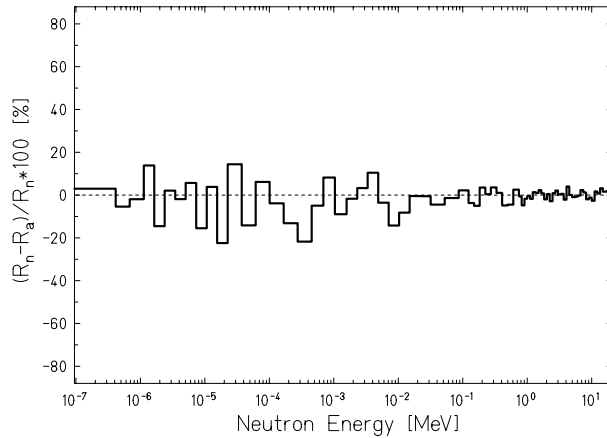


**Figure 6.9:** Relative variation of the nominal response of Ollio without air-gap ( $R_n$ ) with respect to the response including an air-gap of 3.5 mm ( $R_a$ ).

air-gap yields an overall increase of the response up to 20 %. Stanlio, with its diameter of 118.5 mm, resembles rather the 81 mm sphere. Due to the air-gap it shows an increased response of 10 % to neutrons with energies below  $E=1$  keV and a lower response up to 20 % for energies higher than 1 keV. Ollio is not affected significantly by an air-gap of 3.5 mm thickness since it has a radius of 127.5 mm.

The simulated air-gap of 3.5 mm represents an upper limit of the real situation and thus also an upper limit for the resulting uncertainties.

### 6.2.1.2 Density uncertainties

The density of commercial polyethylene can vary between  $\rho_{PE}=0.92$  g/cm<sup>3</sup> and 0.98 g/cm<sup>3</sup>. A small variation in density can lead to a large change in response [Wie94], *i. e.*  $\Delta R/R \gg \Delta \rho/\rho$ . The magnitude of this effect varies with energy.

The nominal density  $\rho_{PE}=0.963$  g/cm<sup>3</sup> was specified by the supplier for the polyethylene of the Bonner spheres. This value was taken for all response calculations performed with FLUKA. In order to verify this value, the density was determined by measuring the weight and the volume of the moderator spheres, excluding the cavities for the <sup>3</sup>He proportional counter and the filler pieces. The results are listed in Table 6.2. The errors are originating from measuring uncertainties. It can be seen that for each sphere the measured density agrees very well with the supplier's specification.

**Table 6.2:** Measured polyethylene densities of the conventional moderator spheres.

| Sphere | Density [g/cm <sup>3</sup> ] |
|--------|------------------------------|
| 81 mm  | 0.962±0.012                  |
| 108 mm | 0.971±0.013                  |
| 133 mm | 0.969±0.005                  |
| 178 mm | 0.965±0.009                  |
| 233 mm | 0.963±0.013                  |

Similarly, density measurements were performed for the filler pieces of the conventional spheres. The results are listed in Table 6.3.

**Table 6.3:** Measured polyethylene densities of the filler pieces and the fraction of their volume to the total volume of the Bonner spheres.

| Sphere | Density [g/cm <sup>3</sup> ] | $V_{fill}/V_{tot}$ [%] |
|--------|------------------------------|------------------------|
| 81 mm  | 0.942±0.018                  | 5                      |
| 108 mm | 1.142±0.004                  | 6                      |
| 133 mm | 0.957±0.021                  | 4                      |
| 178 mm | 0.959±0.002                  | 2                      |
| 233 mm | 0.962±0.004                  | 2                      |

In general, the measured densities of the filler pieces agree quite well within the errors with the specified one, except for the filler piece of the 108 mm sphere which seems to be built from another material.

The influence on the response by the filler pieces was investigated in more detail for the 81 mm and 108 mm spheres, because they show the largest difference from the nominal value (2 % deviation for the filler piece of the 81 mm sphere and 19 % for the filler piece of the 108 mm sphere). For these two spheres calculations were carried out implementing the measured densities listed in Table 6.3. The results are shown in Figures 6.10 and 6.11.

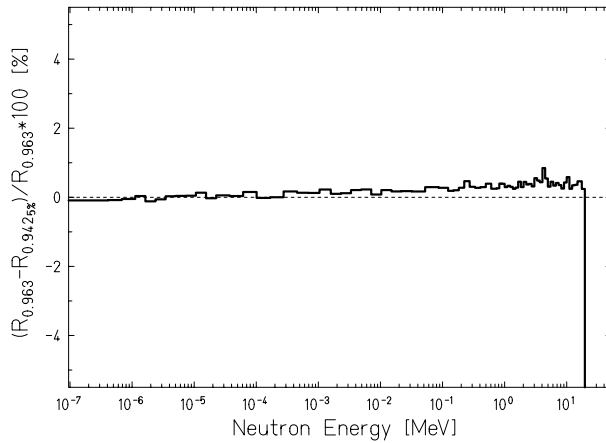


**Figure 6.10:** Relative variation of the response of the 81 mm sphere with filler pieces of  $\rho_{PE}=0.942 \text{ g/cm}^3$  ( $R_{0.9425}$ ) with respect to the 81 mm sphere entirely made of polyethylene of  $\rho_{PE}=0.963 \text{ g/cm}^3$  ( $R_{0.963}$ ), as a function of neutron energy.

It can be seen from Figure 6.10 that the response of a 81 mm sphere containing 5 % polyethylene with density  $\rho_{PE}=0.942 \text{ g/cm}^3$  and 95 % polyethylene with  $\rho_{PE}=0.963 \text{ g/cm}^3$  differs by less than 1 % from the response of the 81 mm sphere entirely made of polyethylene of  $\rho_{PE}=0.963 \text{ g/cm}^3$  (Figure 6.10). For the 108 mm sphere the variation is larger. A 108 mm sphere consisting of 6 % plastics with a density of  $\rho_P=1.142 \text{ g/cm}^3$  and of 94 % polyethylene of  $\rho_{PE}=0.963 \text{ g/cm}^3$  has a difference in response of up to 5 % as compared to the 108 mm sphere made of pure polyethylene of  $\rho_{PE}=0.963 \text{ g/cm}^3$  (Figure 6.11).

For measuring the densities of the lead-, cadmium- and polyethylene components of the filler pieces of Stanlio and Ollio, they had to be dismounted. The densities of the various materials were measured with the same method used for the conventional spheres. The results are listed in Table 6.4. As it can be seen the densities of the lead and the cadmium in the filler pieces agree very well within their uncertainties with the nominal values of  $\rho_{Pb}=11.35 \text{ g/cm}^3$  and  $\rho_{Cd}=8.64 \text{ g/cm}^3$ . In contrast, the density of the polyethylene in the filler pieces of Stanlio and Ollio

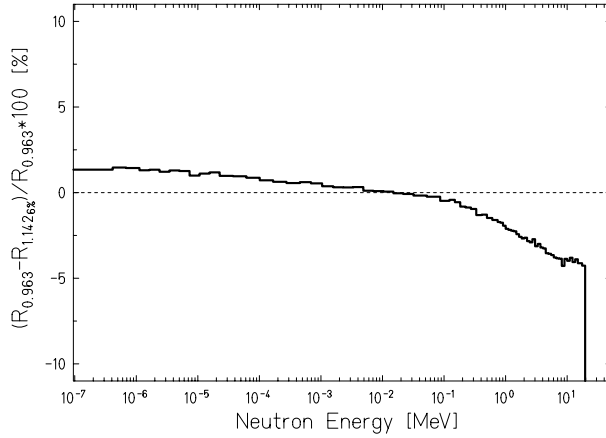


**Figure 6.11:** Relative variation of the response of the 108 mm sphere with filler pieces of  $\rho_P=1.142 \text{ g/cm}^3$  ( $R_{1.142\%}$ ) with respect to the 108 mm sphere entirely made of polyethylene of  $\rho_{PE}=0.963 \text{ g/cm}^3$  ( $R_{0.963}$ ), as a function of neutron energy.

**Table 6.4:** Measured densities of the lead, cadmium and polyethylene filler pieces of Stanlio and Ollio.

| Sphere  | Density [g/cm <sup>3</sup> ] |           |              |
|---------|------------------------------|-----------|--------------|
|         | Lead                         | Cadmium   | Polyethylene |
| Stanlio | 11.25±0.16                   | 8.12±0.71 | 0.92±0.02    |
| Ollio   | 11.2±0.2                     | 8.0±1.0   | 0.94±0.01    |

is significantly different from the nominal one. Separate density measurements of the various materials composing the moderator shells of Stanlio and Ollio were not possible since they are fixed together. The determination of these densities was approached in another way: the density of lead and cadmium was assumed to be the nominal one (justified by the filler pieces). For determining the polyethylene density the entire shells (consisting of polyethylene, cadmium and lead) were weighed. Taking the geometrical specifications of the spheres listed in Table 6.1 and the nominal densities of lead, cadmium and polyethylene, the expected weight of the spheres could be calculated. Then the density of the polyethylene was varied between  $\rho_{PE}=0.92$  and  $0.98 \text{ g/cm}^3$  until the expected weight was equal to the actual one. The results are shown in Table 6.5.

For Ollio this method worked very well since it contains a large amount of polyethylene. While the expected weight of Ollio calculated with a polyethylene

**Table 6.5:** Calculated polyethylene density of the moderator spheres of Stanlio and Ollio.

| Sphere  | Density [g/cm <sup>3</sup> ] |
|---------|------------------------------|
| Stanlio | not measurable               |
| Ollio   | 0.97±0.02                    |

lene density of  $\rho_{PE}=0.92$  g/cm<sup>3</sup> differed by  $\sim 600$  g from the measured one, it agreed with an assumed polyethylene density of  $\rho_{PE}=0.97$  g/cm<sup>3</sup>. For Stanlio, however, this method led only to a weight variation of 20 g for a density variation over the whole range of  $\rho_{PE}=0.92$ -0.98 g/cm<sup>3</sup>, which is less than 0.5 % of the total weight and thus is not significant enough to determine correctly a density value.

In summary, the density measurements of the materials contained in Stanlio and Ollio have shown that for Ollio the density of the polyethylene in the moderator shells agrees with the nominal value, whereas the density of the polyethylene in the filler piece is different. However, the volume fraction of the polyethylene in the filler piece to the one in the shell is only 1.3 %, so that the influence on the response function is negligible (Figure 6.12).

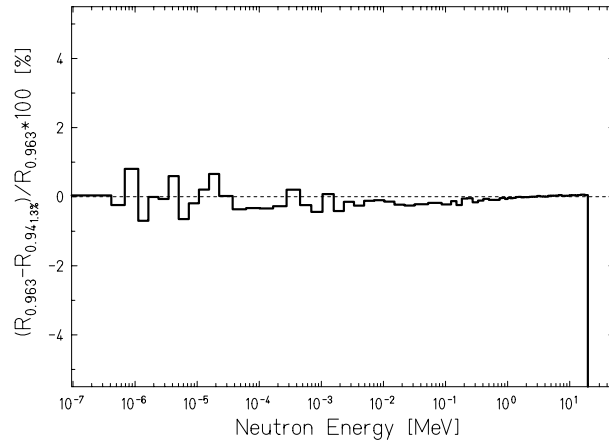


**Figure 6.12:** Relative variation of the response of Ollio with filler pieces consisting of polyethylene of  $\rho_{PE}=0.94$  g/cm<sup>3</sup> ( $R_{0.941.3\%}$ ) with respect to the response of Ollio entirely made of polyethylene of  $\rho_{PE}=0.963$  g/cm<sup>3</sup> ( $R_{0.963}$ ), as a function of neutron energy.

In the case of Stanlio the density of the polyethylene in the moderator sphere could not be determined accurately. If the moderator shell is made of the same

polyethylene as the filler piece, the change of the response would be up to 15 % as compared to the response of Stanlio with nominal polyethylene density (Figure 6.13). This scenario represents the largest density deviation from nominal conditions and is therefore a good upper limit for uncertainty estimations of the response function of Stanlio.

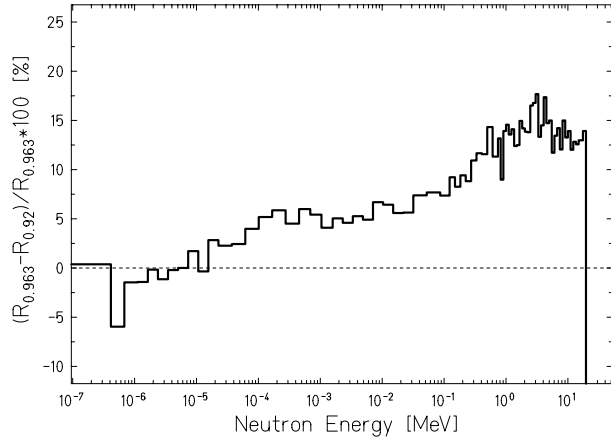


**Figure 6.13:** Relative variation of the response of Stanlio consisting of polyethylene of  $\rho_{PE}=0.92 \text{ g/cm}^3$  ( $R_{0.92}$ ) with respect to the response of Stanlio made of polyethylene of  $\rho_{PE}=0.963 \text{ g/cm}^3$  ( $R_{0.963}$ ), as a function of neutron energy.

### 6.2.1.3 Diameter uncertainties

The diameter of all spheres was measured several times, with different tools on two positions: along the equator and near the poles. Thus, a measured mean diameter,  $D_m$ , of each sphere could be determined. Its uncertainty represents the deviation from an ideal sphere and is given by half the difference between the results obtained near the poles and those along the equator. The values presented in Table 6.6 are the nominal diameter  $D_n$ , the measured diameter  $D_m$  and, in the last column, the relative deviation of  $D_m$  with respect to  $D_n$ . The measurements have shown that the diameters of some spheres differ slightly from the specifications and from an ideal spherical shape. Stanlio, the 108 mm and the 178 mm spheres show the largest deviation from the specifications and their response functions were therefore re-calculated with the measured diameters given in Table 6.6. The differences between the old and the new calculations are shown in Figures 6.14-6.16 for Stanlio, the 108 mm sphere and the 178 mm sphere, respectively.

**Table 6.6:** Nominal and measured outer diameters of the Bonner spheres. The last column gives the relative deviation of the measured diameter with respect to the nominal one.

| Spheres | Diameter [mm] |                 | $\frac{D_n - D_m}{D_n} [\%]$ |
|---------|---------------|-----------------|------------------------------|
|         | $D_n$         | $D_m$           |                              |
| 81 mm   | 81            | $80.9 \pm 0.1$  | 0.1                          |
| 108 mm  | 108           | $107.6 \pm 0.3$ | 0.4                          |
| 133 mm  | 133           | $133.3 \pm 0.1$ | -0.2                         |
| 178 mm  | 178           | $178.7 \pm 0.5$ | -0.4                         |
| 233 mm  | 233           | $232.4 \pm 2.0$ | -0.3                         |
| Stanlio | 118.5         | $120.5 \pm 2.3$ | 1.7                          |
| Ollio   | 255           | $254.5 \pm 2.5$ | 0.2                          |

In Figure 6.14 it can be seen that for Stanlio with an 1.7 % increased diameter of the moderator, the response to neutrons above  $E=100$  keV increases up to 5 %. Below  $E=1$  keV the variation of the response is less than 2.5 %. The diameter variation of  $\sim 0.4$  % for the spheres 108 mm and 178 mm lead to variations in the response functions of less than 5 % (Figures 6.15 and 6.16).

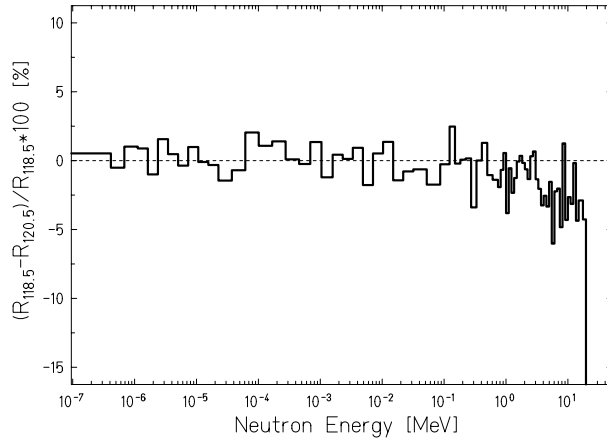


**Figure 6.14:** Relative difference between the response of Stanlio with a measured diameter of 120.5 mm ( $R_{120.5}$ ) and the nominal one of 118.5 mm ( $R_{118.5}$ ), as a function of neutron energy .

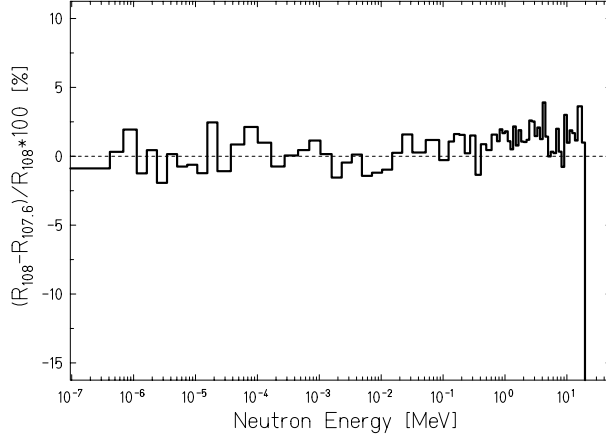


**Figure 6.15:** Relative difference between the response of the 108 mm sphere with a measured diameter of 107.6 mm ( $R_{107.6}$ ) and the nominal one of 108 mm ( $R_{108}$ ), as a function of neutron energy.

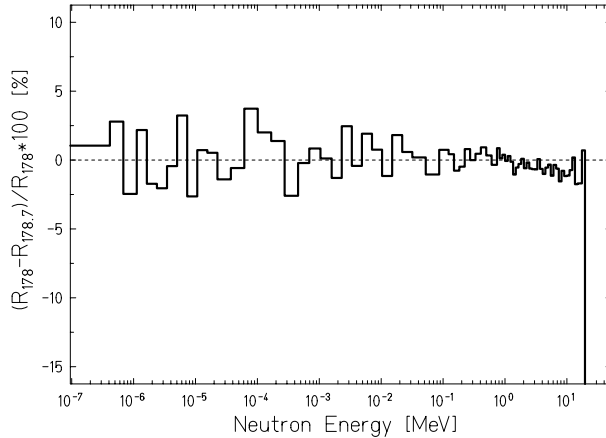


**Figure 6.16:** Relative difference between the response of the 178 mm sphere with a measured diameter of 178.7 mm ( $R_{178.7}$ ) and the nominal one of 178 mm ( $R_{178}$ ), as a function of neutron energy.

### 6.2.2 Estimate of the response function uncertainties

For the analysis of experimental data from the Bonner spheres (Chapters 7, 8 and 9) the knowledge of the response function uncertainties is essential. Due to limited computing time the response functions of all Bonner spheres could not be re-calculated with varying all possible parameters responsible for those uncertainties. Instead, re-calculations of the entire Bonner sphere spectrometer were performed in detail by varying only the parameters of the major sources of uncertainty. For the other sources an upper limit for the response uncertainty was determined for one sphere and applied to all the others.

As shown in the previous section the air-gap between the  ${}^3\text{He}$  proportional counter and the moderator is the major source of uncertainty resulting in responses varying up to 35 % depending strongly on the sphere diameter. The measurements of the polyethylene densities have shown large deviations from the nominal values only for Stanlio with response variations of up to 15 %, which is comparable to the effect of the air-gap. Thus, all response functions of the extended-range Bonner sphere set were re-calculated including the largest possible air-gap in the geometry and for Stanlio including additionally the deviation of the polyethylene density. The outcome of these re-calculations is a set of ‘modified’ response functions which are listed in detail in Appendix C.

The 108 mm sphere, which includes filler pieces of a material other than polyethylene, yields to response deviations of up to 5 %, thus an overall uncertainty of 5 % was assumed for it. The 81 mm sphere whose filler pieces have the largest deviation of the polyethylene density from the nominal one as compared to the 133 mm, 178 mm and 233 mm spheres, yields response variation of less than 1 %. Therefore, the responses of the other spheres were not re-calculated, since their variations due to density uncertainties are even lower, but a general uncertainty of 1 % was considered. The density of the filler piece of the largest sphere, Ollio, differs also from the nominal density. However, due to the small volume of the filler pieces as compared to the total volume of the sphere its effect is also smaller than 1 %. An overall uncertainty of 1 % was assumed in that case, too.

The deviation from the nominal diameters of the moderator spheres varies between 0.1 % and 1.7 %. The response functions of the three spheres with the largest variations were re-calculated in order to estimate an overall upper limit for the response uncertainty due to diameter uncertainties. The results show a response variation of up to 5 % for Stanlio and for the 108 mm and 178 mm spheres. The responses of the other spheres were not re-calculated as their effect of the diameter uncertainty is even smaller. Thus, an overall uncertainty of 5 % due to diameter variations was considered for all spheres.

Finally, the real total uncertainty of the response of each sphere depends also on the radiation field to which it is exposed. In particular, the response variations due to geometry, density and moderator thickness uncertainties are strongly energy dependent. For example, for monoenergetic neutron beams the response can vary up to 40 %, while in neutron fields of a wide energy range the effect is probably reduced and the assumed uncertainties may be a little overestimated.

## 6.3 The ${}^3\text{He}$ proportional counter

### 6.3.1 Fundamentals

The detection of neutrons in a  ${}^3\text{He}$  proportional counter is based on the  ${}^3\text{He}(n, p){}^3\text{H}$  reaction, yielding a proton and a tritium nucleus. These two particles share a  $Q$  value of  $E=764$  keV at a ratio of 3:1 plus the kinetic energy of the incident neutron. The details of the reaction are as follows:



$$\sigma(n, p) = 5327 \text{ barns} \quad (6.2)$$

$$E({}^3\text{H}) \geq \frac{Q}{4} = 0.191 \text{ MeV} \quad (6.3)$$

$$E(p) \geq \frac{3}{4}Q = 0.573 \text{ MeV} \quad (6.4)$$

The charged particles deposit their energy in the counter gas, producing ionization along their oppositely directed tracks. The electrons liberated along the particle tracks drift under the influence of an electric field towards the anode wire. At a short distance from the anode, the electric field rises to a high value and the drifting electrons gain sufficient energy to ionize neutral atoms. Thus the charge released in the detector by a neutron event is increased by a large factor (gas amplification). The electrons are collected by the anode, leaving a large number of positive ions clustered near the anode surface. These ions move away from the anode at a velocity much lower than that of the electrons, but because of their large number and of the fact that their way is longer than the one of the electrons they are responsible for most of the signal pulse amplitude.

In the gas amplification process, the charge multiplication is controlled by the value of the high-voltage applied to the anode. Multiplication factors of up to approximately 1000 are common and the signal pulse amplitude can be adjusted to maintain an adequate signal to noise ratio at the amplifier input.

The fundamental quantity from a proportional counter is the charge produced per event, *i.e.* the time integral of the current pulse due to the mechanism described above. The charge output as a function of the voltage depends on the  ${}^3\text{He}$  pressure, the amount of quench gas additive and the diameter of the anode wire and cathode. Figure 6.17 shows the detector characteristics of the 2 atm and 4 atm  ${}^3\text{He}$  proportional counters used in this work.

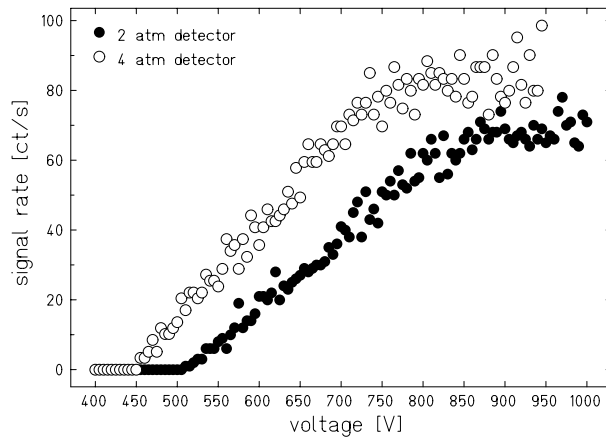


**Figure 6.17:** Signal rate versus voltage for two detectors of different gas pressure. The detectors were placed in a Bonner sphere and exposed to an  $^{241}\text{Am-Be}$  source of the same strength.

In a  $^3\text{He}$  detector the proton and tritium tracks have lengths of the order of the counter dimensions. The proton track length  $L$  is approximately given by

$$L = \frac{k}{P} \quad (6.5)$$

where  $P$  is the gas pressure and  $k \approx 1 \text{ bar}\cdot\text{cm}$ . The orientation of the tracks is isotropic. Protons or tritium produced by events occurring near the detector wall can directly deposit energy in the wall. Such events produce signal pulses smaller than those from full-energy events. This effect is commonly referred to as wall effect and is sketched in Figure 6.18.

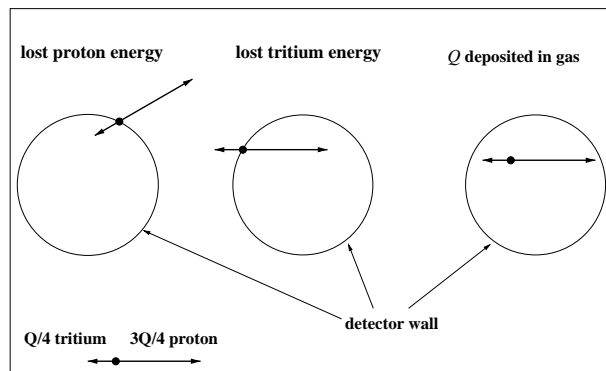


**Figure 6.18:** The conditions of getting a detector signal. **Right:** proton and tritium deposit their energy in the detector gas. **Middle:** tritium loses its energy to the wall. **Left:** proton loses its energy to the wall.

These effects cause the typical shape of the  ${}^3\text{He}$  proportional counter (see Figure 6.19 from right to left): a high and narrow thermal peak, where all the energy  $Q$  from the  $(n, p)$  reaction is deposited in the detector gas; a broad, flat region (tail), where only part of the energy  $Q$  is deposited in the gas; a sharp edge around 1/4th of the peak-channel, which indicates the threshold of the reaction  ${}^3\text{He}(n, p){}^3\text{H}$ , and below this edge a region with an exponential signal coming from electronic noise and gamma rays.

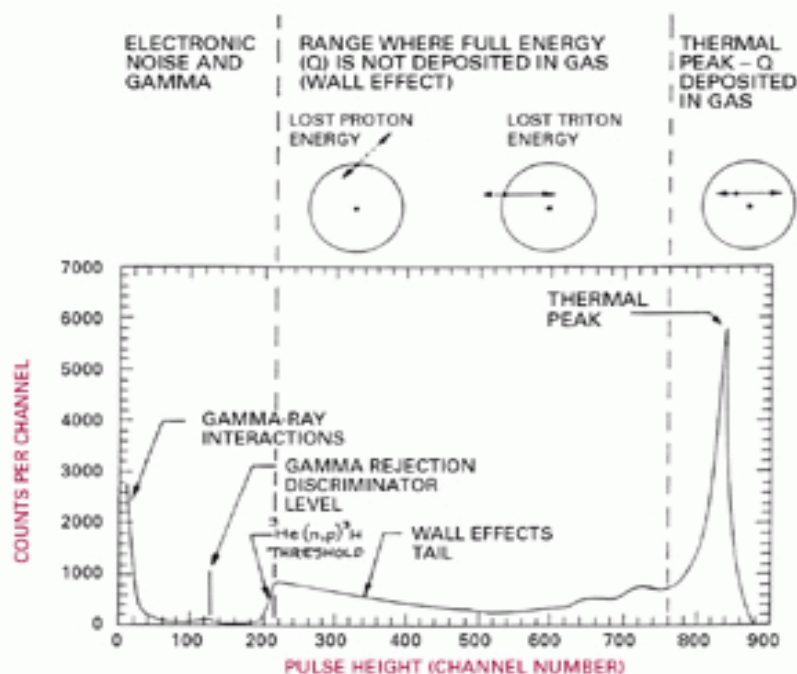


**Figure 6.19:** The pulse height spectrum of a  ${}^3\text{He}$  proportional counter. Three main regions can be distinguished (from the right to the left): 1.) the thermal peak - the entire energy is deposited in the counter gas, 2.) the flat tail - parts of the energy are deposited in the detector wall, 3.) the electronic noise and gamma contribution.

Gamma radiation produces a response in the detector by means of Compton electrons which originate in the wall of the detector. For high-energy photons, the ionization tracks frequently are longer than the detector diameter. The rate of gamma interactions is proportional to the total wall area. The size of each gamma pulse is proportional to the product of pressure and diameter.

When pulse height spectra are recorded for a  ${}^3\text{He}$  counter exposed to gamma rays, the spectral shape is very well fitted by a straight line in a semi-logarithmic plot. This is illustrated in Figure 6.20 for the irradiation of the counter by  ${}^{137}\text{Cs}$  sources of different intensities. Below channel 30 the electronic noise dominates and thus the pulse height spectra is independent of the source intensity.

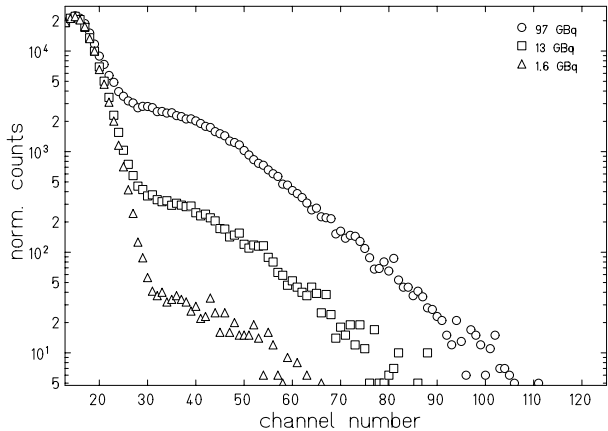


**Figure 6.20:** Pulse height spectra of a  ${}^3\text{He}$  proportional counter exposed to  ${}^{137}\text{Cs}$  sources of different strengths. Above channel 30 the spectral shape can be fitted very well by a straight line. Below channel 30 electronic noise dominates and therefore the spectrum is independent of the source intensity.

### 6.3.2 Intercalibration

Three different  ${}^3\text{He}$  proportional counters were used in this work, all of spherical shape, purchased from Centronic Limited, UK, with the following specifications:

- *2 atm-detector*: 2 atm  ${}^3\text{He}$ , HV=812 V
- *4 atm-detector*: 4 atm  ${}^3\text{He}$ , HV=890 V
- *B-detector*: 2 atm  ${}^3\text{He}$ , HV=824 V

In order to compare the counter readings of the three detectors intercalibration measurements were performed at the PTB in February 2001. The set-up used for the measurements was constructed especially for intercalibration purposes and provided a high accuracy of positioning. Each detector was placed in the centre of a 12.7 cm (=5 inch) Bonner sphere from the PTB and irradiated by an  ${}^{241}\text{Am-Be}$  source. The derived intercalibration factors are given in Table 6.7.

**Table 6.7:** Intercalibration of the  ${}^3\text{He}$  proportional counters used within this work. They are labelled as 2 atm-, 4 atm- and B-detector [Witt01].

|              | Intercalibration factor |
|--------------|-------------------------|
| 2 atm/4 atm  | $0.739 \pm 0.007$       |
| 2 atm/B-det. | $0.984 \pm 0.011$       |
| B-det./4 atm | $0.751 \pm 0.011$       |

## 6.4 Electronics

The electronics needed for a Bonner sphere system are a preamplifier, an amplifier, a single or multi channel analyzer (SCA/MCA), a counter and the power supply. In order to discriminate the gamma ray and electronic noise contribution from the neutron signal a threshold is set by the SCA/MCA usually below the edge of the neutron pulse height spectrum (see Figure 6.21) and only the integral counts above the threshold are recorded. In radiation fields exclusively dominated by neutrons a small displacement of the threshold is not critical and the variation of the integrated counts is much less than 1 %. On the other hand, in mixed fields with a large contribution of gammas a slight variation of the threshold can increase or decrease the number of counts due to gammas significantly. It is therefore advisable to raise the threshold in such environments; although a few percent of the total neutron counts will be lost, the gamma contribution can be suppressed by up to a factor 100 (see Figure 6.21).

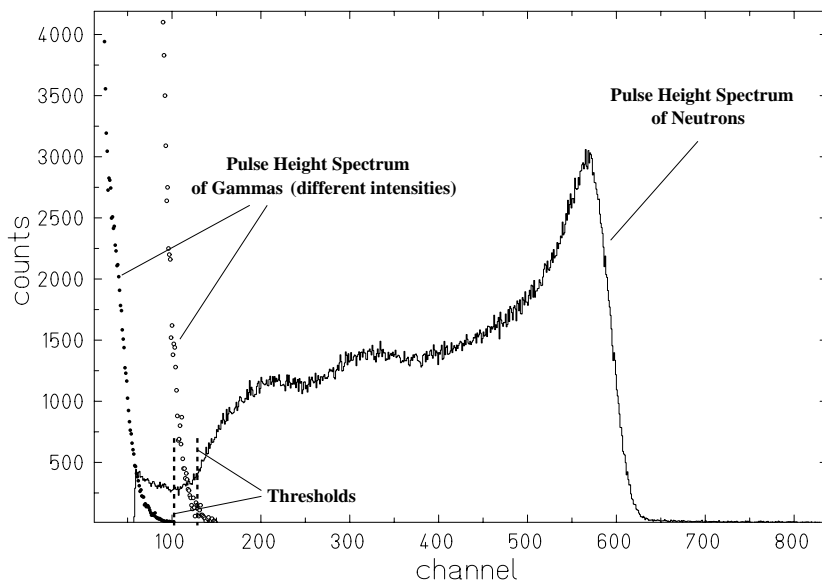


**Figure 6.21:** Pulse height spectrum of a  ${}^3\text{He}$  proportional counter in a mixed radiation field. The gammas are discriminated from the neutrons by an electronic threshold. The threshold is set according to the intensity of the gamma radiation.

Apart from the preamplifier (Ortec 142) two types of electronics were used for the Bonner sphere set. For the first tests in May 2000 electronics which originally belongs to the LINUS [Bir98a] was used. This was based on NIM standard and consists of an amplifier (Ortec 570), a single channel analyzer (Ortec 550A), a counter (Ortec 994) and the power supply (I+P) assembled in a portable NIM crate. The settings of this system were adjusted for the LINUS which has the

same type of  ${}^3\text{He}$  proportional counter as the Bonner spheres but a different operating voltage. Because of the lack of a MCA at that time it was impossible to re-adjust the thresholds which is necessary when using a different operating voltage. For this reason the LINUS settings were kept at the beginning. They are listed in Table D.1 of the Appendix.

A compact electronic device which could be operated via a PC and included a MCA was purchased later from Münchner Apparate Bau – MAB, Germany. The block diagram in Figure 6.22 sketches the arrangement of the components. The electronic settings of the MAB device for the three  ${}^3\text{He}$  proportional counters are summarized in Table D.2, the technical specifications of the components in Table D.3 of the Appendix.

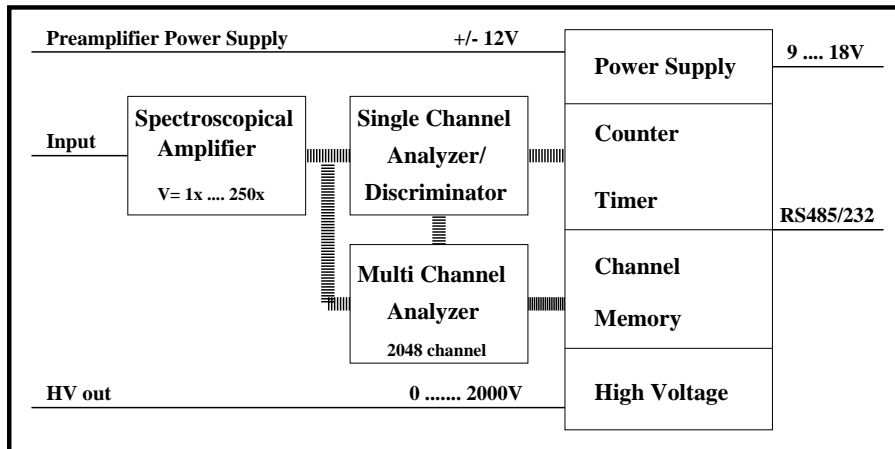


**Figure 6.22:** Block diagram of the MAB device (Mikro Messkanal 2100/MCA).

The MAB device can be operated either in a single-channel/discriminator mode or in a multi-channel/analyizer mode. In order to verify whether the two modes give the same results the detector was irradiated with a Pu-Be source and the subsequent data acquisition was run in both modes. Within the statistical uncertainties both modes resulted in the same signal rate, as seen in Table 6.8 and Figure 6.23.

**Table 6.8:** Data acquisition with the MAB device running both in discriminator and analyzer mode. Both acquisition modes gave the same detector count rate.

|                    | Mean count-rate [ct/s] | Error of mean [ct/s] |
|--------------------|------------------------|----------------------|
| Discriminator mode | 170.6                  | 0.6                  |
| Analyzer mode      | 171.3                  | 0.4                  |

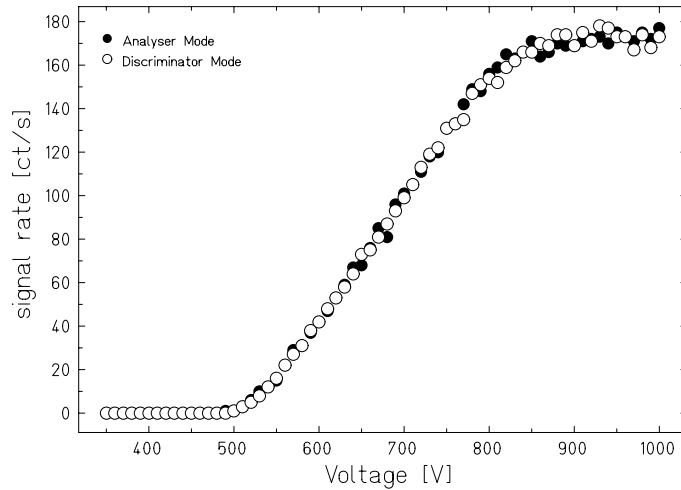


**Figure 6.23:** Detector characteristics of the 4 atm-detector performed with the MAB electronic device. Data was acquired both in discriminator mode and analyzer mode.

## 6.5 Sphere support

The original supports for the conventional Bonner spheres were plastic cylindrical pipes with a wall thickness of 3 mm. The diameters and heights of the supports depend on the sphere they are used for. Table 6.9 summarizes the dimensions of the plastic supports for the different spheres.

**Table 6.9:** Dimensions of the plastic supports of the Bonner spheres.

| Diameter | Height  | Sphere                  |
|----------|---------|-------------------------|
| 12 cm    | 14 cm   | 233 mm, Ollio           |
| 12 cm    | 18 cm   | 178 mm                  |
| 7 cm     | 19.7 cm | 108 mm, 133 mm, Stanlio |
| 5.9 cm   | 21.8 cm | 81 mm, 81Cd             |

As it can be seen some supports are used for more than one sphere. This is inconvenient for experiments that require all sphere centres to be aligned exactly at the same height. The material - plastics - also increases neutron scattering due to the large amount of hydrogen in it. Simulations were therefore carried out in order to investigate the extent of neutron scattering on such a plastic support and to compare it to scattering on an aluminium one. The geometry used for the calculations is shown in Figure 6.24.

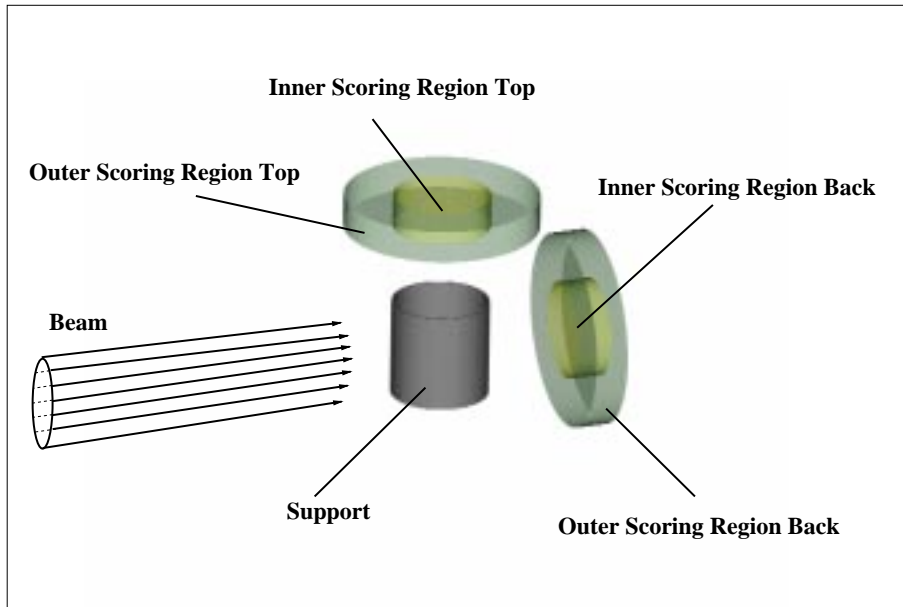


**Figure 6.24:** Geometry configuration used for the simulation of the neutron scattering due to the sphere supports. A circular beam hits the sphere support, either aluminium or polyethylene. Four scoring regions record the outgoing spectra.

The primary neutrons originate from a circular surface of radius  $r=7.5$  cm with a flat energy spectrum. The beam hits a pipe made of either polyethylene or aluminium with radius  $r=7.5$  cm, height  $h=15$  cm and wall thickness  $d=3$  mm. After the interaction the neutron spectra are scored in four regions. The first one is located behind the support and has the same dimensions as the beam,  $r=7.5$  cm (inner back region). If the interactions of the beam with the support would be negligible the neutron spectrum in that scoring region should be very similar to the spectrum of the input beam. The second region is annular with  $r_i=7.5$  cm and  $r_o=15$  cm (outer back region). It gives information about the broadening of the beam due to scattering. The other two scoring regions are above the sphere support - inner top region ( $r=7.5$  cm) and outer top region ( $r_i=7.5$  cm and  $r_o=15$  cm) - where the spheres are placed. The spectra recorded there provide an estimation of the neutrons scattered into the sphere during measurements.

The results of the simulations are shown in Figures 6.25 and 6.26. It can be seen that the plastic support increases drastically the amount of neutrons below  $E=1$  MeV in all four scoring regions, whilst the aluminium support has negligible effect. For the latter the neutrons in the inner back scoring region show the same spectral shape as the primary ones, and the differential neutron fluences in the other scoring regions are more than one order of magnitude lower than compared to those in the inner back region.

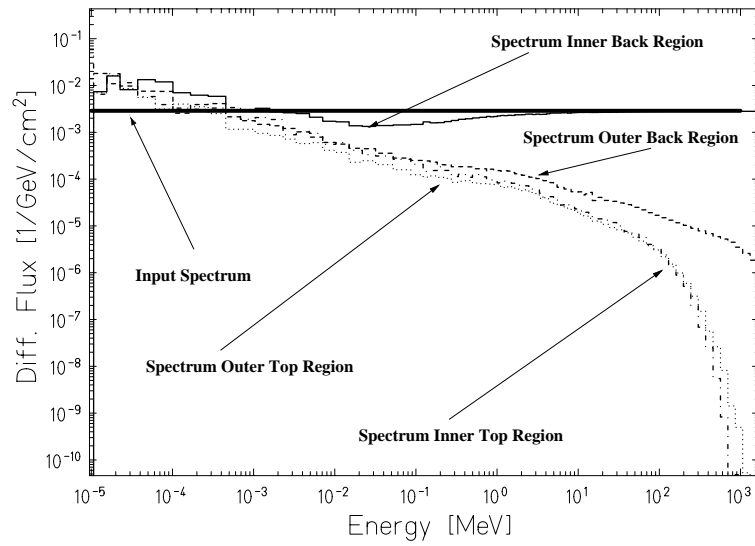


**Figure 6.25:** The input spectrum flat in differential flux and the outcoming scattered spectra for the polyethylene sphere support. The spectra in the top scoring regions show a large fraction of low-energy neutrons due to scattering in the support material.

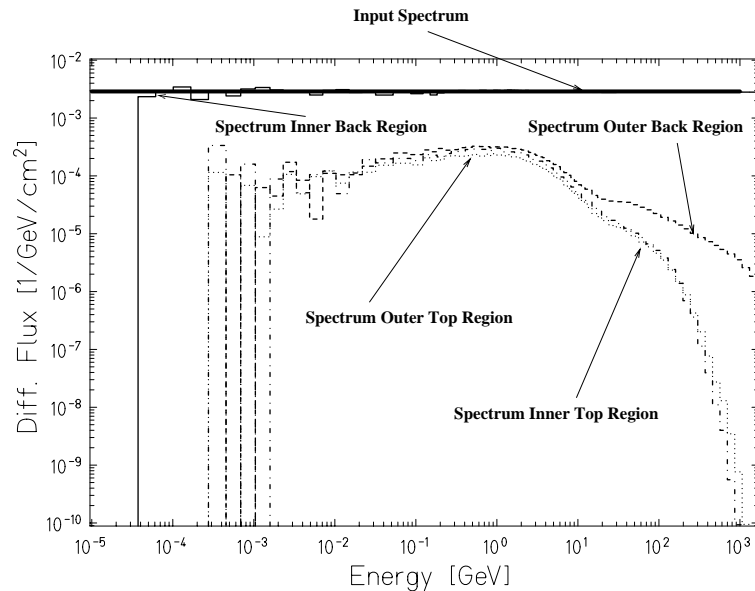


**Figure 6.26:** The input spectrum flat in differential flux and the outcoming scattered spectra for the aluminium sphere support. No significant scattering can be observed. The outcoming spectrum in the inner back region shows the same shape as the input spectrum. The spectra in the other scoring regions are at least one order of magnitude lower than the input one.

For this reason new sphere supports made of aluminium were constructed for each sphere. The dimensions of the supports were chosen in such a way that the centre of each sphere is located at 25 cm above the ground (Table 6.10).

**Table 6.10:** *Dimensions of the aluminium supports of the Bonner spheres including a 12 mm thick base plate for mounting.*

| Diameter | Height | Sphere      |
|----------|--------|-------------|
| 55 mm    | 218 mm | 81 mm, 81Cd |
| 65 mm    | 205 mm | 108 mm      |
| 65 mm    | 191 mm | 133 mm      |
| 120 mm   | 182 mm | 178 mm      |
| 120 mm   | 148 mm | 233 mm      |
| 65 mm    | 198 mm | Stanlio     |
| 120 mm   | 136 mm | Ollio       |

# Chapter 7

## Calibration measurements with reference neutron beams

Any instrument has to be properly calibrated before it can be employed routinely. The calibration of the Bonner sphere system has two goals: first, if the ratios of the calculated to measured response is constant at all energies for a certain sphere, the shape of the simulated response functions is verified. Second, the value of this ratio is the calibration factor for this Bonner sphere system with this specific  $^3\text{He}$  proportional counter. For these reasons calibration measurements of the new extended-range Bonner sphere system were carried out in May 2001 at the PTB irradiation facility [Bre80].

### 7.1 Experimental set-up

Monoenergetic neutrons of  $E=14.8$  MeV, 5 MeV, 1.2 MeV and 144 keV were produced by proton or deuteron induced reactions on different targets. In general, solid targets were used consisting of thin layers of metallic LiOH and Ti, loaded with deuterium or tritium and evaporated on Ta, Ag or Al backings. Only for the production of  $E=5$  MeV neutrons a gas target was used [Gul94]. Table 7.1 summarizes the target composition, the production reaction, the energy of the projectile and the mean neutron energy. To achieve a higher beam intensity the targets were wobbled.

The measurements were performed in the experimental hall of the accelerator facility of PTB. The irradiation location is placed on a grid floor in the centre of the hall (see Figure 7.1). Due to its large dimensions,  $V=24\text{ m}\times 30\text{ m}\times 14\text{ m}$ , the scattering on the thick concrete walls is small.

**Table 7.1:** Characteristic data for the accelerator produced monoenergetic neutrons at PTB.  $E_p$  is the energy of the projectile,  $E_n$  is the nominal neutron energy and  $\Delta E_n$  the corresponding energy width (FWHM).

| $E_p$     | Target | Reaction                             | $\langle E_n \rangle$ | $\Delta E_n$ |
|-----------|--------|--------------------------------------|-----------------------|--------------|
| 0.242 MeV | Ti(T)  | T(d,n) <sup>4</sup> He               | 14.8 MeV              | 0.9 MeV      |
| 2.30 MeV  | Gas    | D(d,n) <sup>3</sup> He               | 5.0 MeV               | 0.18 MeV     |
| 2.05 MeV  | Ti(T)  | T(p,n) <sup>3</sup> He               | 1.2 MeV               | 0.098 MeV    |
| 1.95 MeV  | LiOH   | <sup>7</sup> Li(p,n) <sup>7</sup> Be | 144 keV               | 12 keV       |

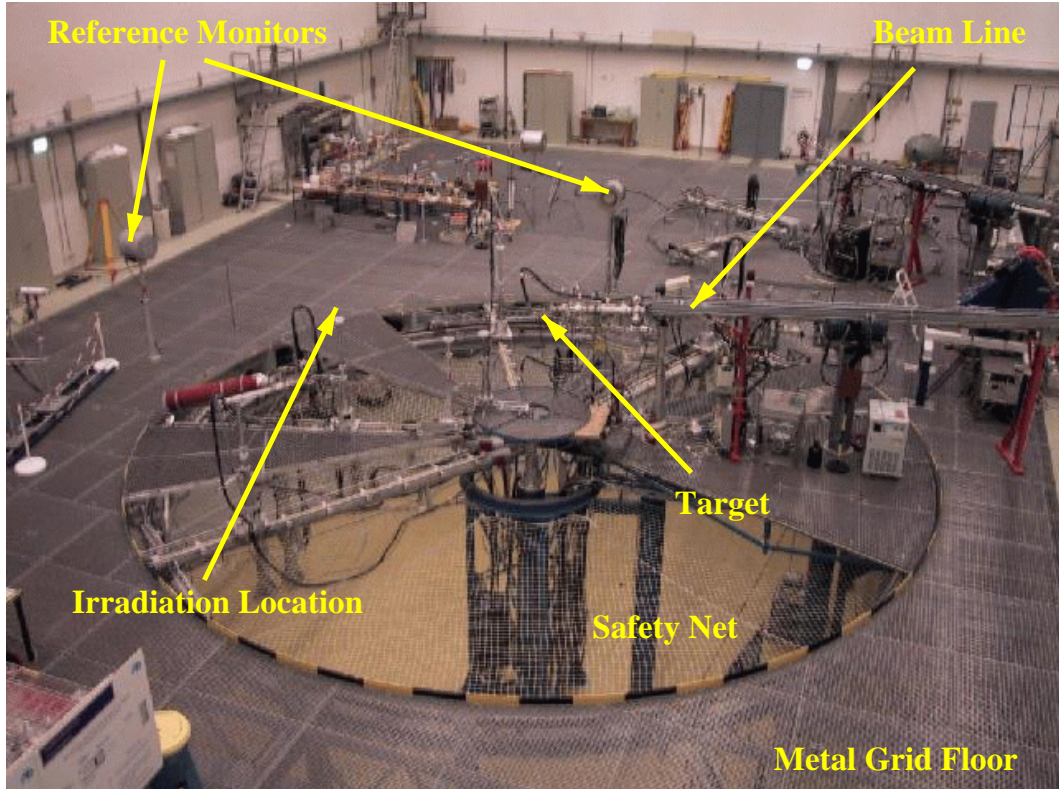


**Figure 7.1:** Photograph of the measuring hall of the PTB accelerator facility.

The calibration of the Bonner sphere system was performed with the 2 atm-detector and the B-detector, which was normalized to the 2 atm-detector using the intercalibration factors of Table 6.7. The spheres were mounted on a detector support which could be moved around the target on a circle of maximum 5.2 m radius. This allows the Bonner spheres to be displaced in a polar and radial

direction with respect to the neutron producing target (Figure 7.2). The spheres were exposed to neutrons emitted in the forward direction at a distance of 2 m from the production target.

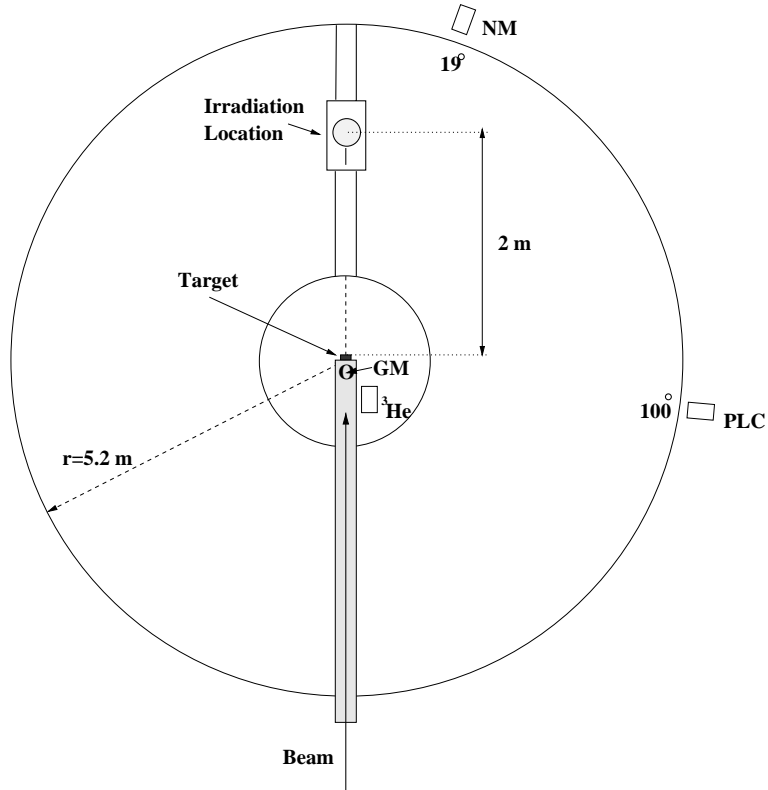


**Figure 7.2:** Experimental set-up for the calibration measurements. The monitors are the precision long counter (PLC), the new monitor (NM), the Geiger-Müller counter (GM) and the  ${}^3\text{He}$  counter. The intensity of the beam was recorded by a charge monitor which is placed in the beam line (not shown). The figure is not to scale.

The smallest Bonner sphere, 81 mm, was always exposed in two orientations with respect to the beam in order to see possible angular dependencies. In the first exposure, the connector of the  ${}^3\text{He}$  proportional counter was placed perpendicular to the beam axis; in the second one, it was behind the sphere with respect to the incoming beam, *i.e.* parallel to the beam axis. As can be seen in Figure 7.3 the results were the same, within the experimental uncertainties, for both exposure positions. The other spheres were exposed with the connector always perpendicular to the beam, a set-up which was also simulated by Monte-Carlo.

The neutron fluence was measured by a proton recoil proportional counter for the energies  $E=144$  keV and 1.2 MeV and by means of a proton recoil telescope for  $E=5$  MeV. With these measurements five reference monitors were calibrated,

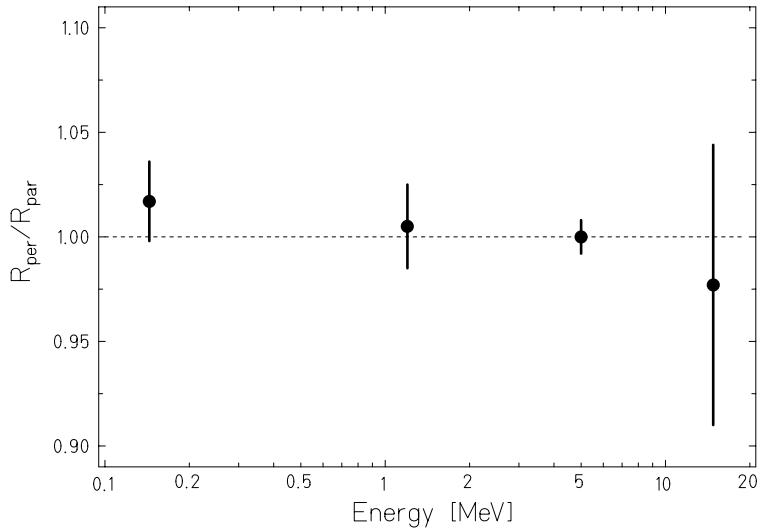


**Figure 7.3:** Ratio of the 81 mm sphere responses with the connector of the  $^3\text{He}$  counter placed perpendicular to the beam axis and parallel to it.

to which all readings of the Bonner spheres were normalized. No fluence measurements were carried out for  $E=14.8$  MeV on the day of the Bonner sphere calibration but former known calibration factors were used [Gul01]. Figure 7.2 sketches the position of the monitors with reference to the beam and the irradiation location.

## Reference monitors

The following instruments were used as reference monitors [Gul98, Gul01]:

### 1. Precision long counter

The precision long counter (PLC) consists of a long  $\text{BF}_3$  proportional counter placed inside a large, specially shaped, moderating cylinder made of polyethylene, boron loaded polyethylene, aluminium and cadmium. It is placed at a distance of about 5.5 m from the target, at an angle of 100 degrees.

### 2. New monitor

The new monitor (NM) consists of a long cylindrical  $^3\text{He}$  proportional counter surrounded by a cylindrical polyethylene layer 15 cm thick. It is mounted at a distance of 5.5 m from the target at an angle of 19 degrees.

### 3. The $^3\text{He}$ proportional counter

A  $^3\text{He}$  proportional counter embedded inside a polyethylene moderator (50 mm in diameter and 233 mm long) was placed on the right hand side to the beam line, just beside it and upstream of the target.

#### 4. The Geiger-Müller counter

In order to measure the photon contribution a Geiger-Müller counter was mounted on top of the production target.

#### 5. The charge monitor

A charge monitor, which is placed in the beam line, is used for monitoring the charge and thus the intensity of the beam impinging on the target. It is not shown in Figure 7.2.

## 7.2 Background measurements

The various components of the neutron field which contribute to the reading of a Bonner sphere are shown schematically in Figure 7.4.

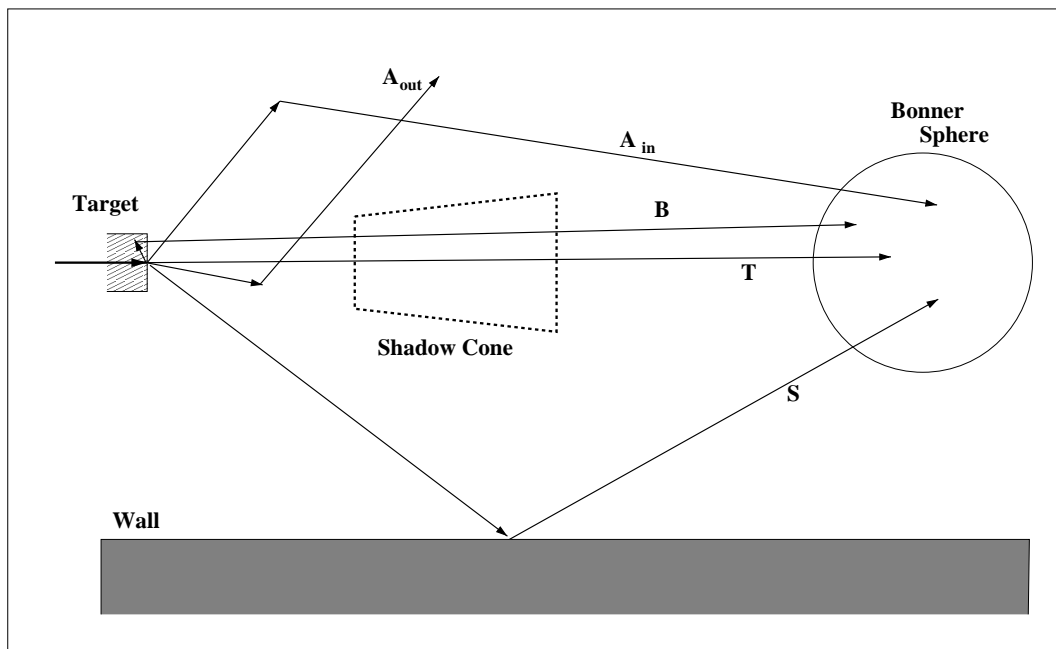


**Figure 7.4:** Schematic representation of various neutron components. T: direct neutrons, B: neutrons scattered within the target into the detector,  $A_{out}$ : neutrons scattered by air away from the detector,  $A_{in}$ : neutrons scattered by air into the detector, S: neutrons scattered by the walls of the experimental hall into the detector.

The contribution of neutrons scattered by the air away from the detector is small as compared to the other neutron components and thus it was not considered further. Besides the neutrons coming directly from the neutron producing target (T), there are also contributions from neutrons scattered in the target, in

particular in the target backing ( $B$ ), in the air ( $A_{in}$ ) and from the walls of the experimental hall ( $S$ ). If a shadow cone is placed between target and detector, the detector can be shielded from the neutron components  $T$  and  $B$ . Thus the contributions from  $S$  and  $A_{in}$  to the counter reading can be measured and subtracted. For precise measurements the aperture and position of the shadow cone must be optimized with respect to the target and detector geometry to avoid both unwanted neutron transmission and overshadowing. This method is usually employed at large source-to-detector distances. Corrections for beam divergence and non-isotropy of the neutron emission can therefore be neglected. Table 7.2 shows the parameters of the shadow cones which were used for the calibration measurements of the extended-range Bonner sphere spectrometer.

**Table 7.2:** Geometrical parameters of the shadow cones used in the measurements: cone aperture, distance from the front of the cone to the target centre, appropriate Bonner sphere.

| Aperture<br>degree | $d_{T-SC}$<br>[mm] | Spheres                      |
|--------------------|--------------------|------------------------------|
| 1.875              | 320                | 81 mm, 81Cd, 108 mm, Stanlio |
| 3.2                | 181                | 133 mm, 178 mm               |
| 5                  | 110                | 233 mm, Ollio                |

The difference of the readings without,  $M$ , and with shadow cone,  $M_S$ , both normalized to the same number of monitor counts, corresponds to the sum of the readings  $M_T$  and  $M_B$ , due to the neutron components  $T$  and  $B$ , respectively:

$$M - M_S = M_T + M_B = R_\Phi \Phi_T + \int R_{\Phi,B}(E) (d\Phi_B(E)/dE) dE \quad (7.1)$$

with  $\Phi_T$ , the fluence of direct neutrons at the detector position;  $\Phi_B$ , the fluence of target-scattered neutrons at the centre of the detector;  $R_\Phi$ , the fluence response to direct neutrons;  $R_{\Phi,B}$ , the fluence response to target-scattered neutrons.

The ratio of the detector readings with and without shadow cone depends on the sphere and on the neutron energy and is summarized in Table 7.3. It can be seen that the small spheres are more sensitive to scattered neutrons, since these neutrons have obviously much lower energies than the direct ones.

The fluence measurements at  $E=144$  keV, 1.2 MeV and 5 MeV provided calibration factors for the reference monitors for direct neutrons, while at  $E=14.8$  MeV the calibration factors are given for total neutrons above  $E=13.5$  MeV, which are

**Table 7.3:** Contribution to the counter reading due to neutrons scattered by the air and the walls of the calibration facility into the detector.

| Sphere  | Energy   |       |         |         |
|---------|----------|-------|---------|---------|
|         | 14.8 MeV | 5 MeV | 1.2 MeV | 144 keV |
| 81Cd    | 62 %     | 22 %  | 25 %    | 15 %    |
| 81 mm   | 71 %     | 26 %  | 29 %    | 17 %    |
| 108 mm  | 48 %     | 13 %  | 18 %    | 14 %    |
| 133 mm  | 34 %     | 8 %   | 13 %    | 11 %    |
| 178 mm  | 21 %     | 5 %   | 10 %    | 10 %    |
| 233 mm  | 12 %     | 3 %   | 7 %     | 8 %     |
| Stanlio | 30 %     | 15 %  | 24 %    | 16 %    |
| Ollio   | 8 %      | 3 %   | 5 %     | 6 %     |

anyway dominated by the direct ones. By means of measurements with and without shadow cone it cannot be distinguished between direct and target-scattered neutrons or neutrons below and above  $E=13.5$  MeV. Thus these contributions have to be subtracted from the detector reading,  $M - M_s$ , in the data analysis by folding the response function with the fluence spectra of the target scattered neutrons or total neutrons above  $E=13.5$  MeV, respectively.

The calculated fluence spectra of target-scattered neutrons and direct neutrons were provided by Schlegel [Sch01] using the TARGET code [Sch98]. The calculation includes proton transport, neutron production and transport in the target, and the attenuation in air. The spectral distribution of direct neutrons,  $T$ , which reach the detector without any collisions (unscattered),  $\Phi_{us}(E)$ , and the contribution of neutrons scattered in the target,  $B$  or  $\Phi_{sc}(E)$ , are calculated separately. The results of these calculations are shown in Figure 7.5. Knowing this, the detector reading due to the direct neutrons can be easily determined for the energies  $E=144$  keV and 1.2 MeV by calculating  $\int R_{\Phi,B}(E)(d\Phi_B(E)/dE)dE$  from equation 7.1. In contrast, for  $E=14.8$  MeV the total contribution of neutrons above  $E=13.5$  MeV has to be considered which is given by  $\int_{13.5}^{\infty} R_{\Phi}(E)(d\Phi(E)/dE)dE$ . For  $E=5$  MeV the effect of neutron scattering in the target is negligible since a gas target was used (see Figure 7.6).

Thus at  $E=144$  keV and 1.2 MeV the correction for the target-scattered neutrons is given by the fraction of the response due to direct neutrons to the total response (direct plus target-scattered neutrons) derived from equation 7.1 and the data of Figure 7.5 by

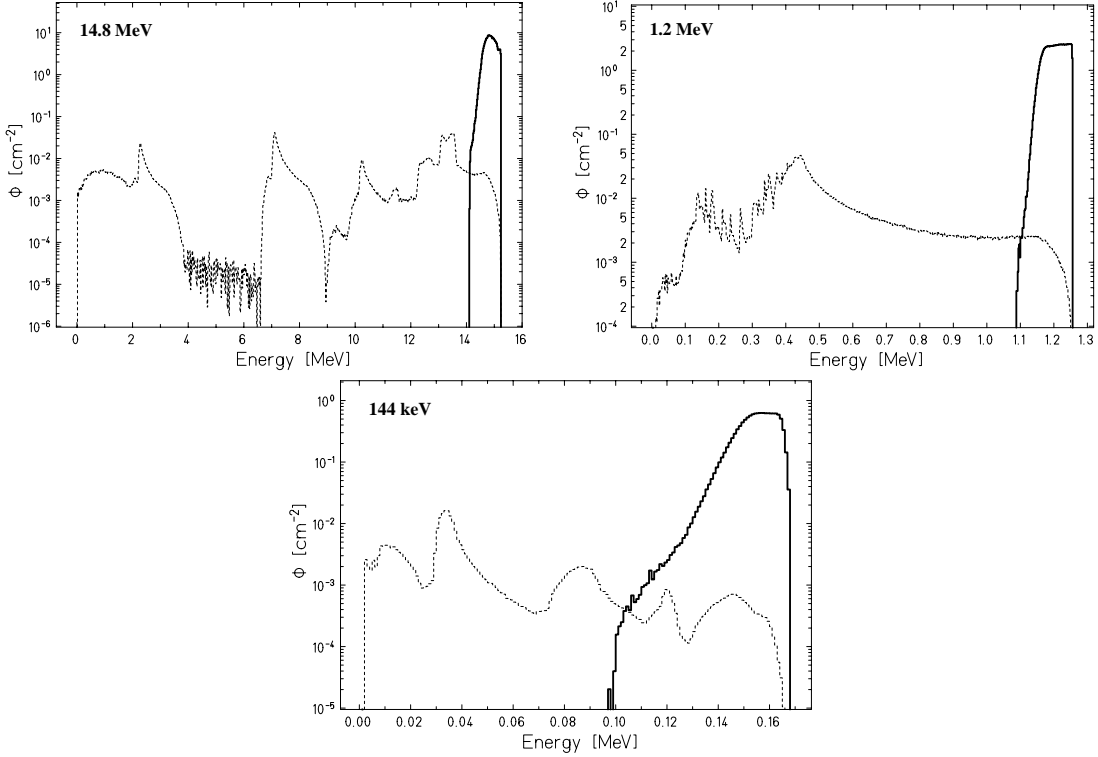


**Figure 7.5:** Unscattered (solid line) and target-scattered (dotted line) neutron spectral distributions at the centre of the detector calculated by TARGET for mean neutron energies:  $E=14.8$  MeV (top left),  $E=1.2$  MeV (top right) and  $E=144$  keV (bottom).

$$f(E)_{us} = \frac{\sum_i R_i \Phi_{i,us}}{\sum_i R_i (\Phi_{i,us} + \Phi_{i,sc})} \quad (7.2)$$

where  $R_i$  is the detector response,  $\Phi_{i,us}$  the unscattered neutron fluence and  $\Phi_{i,sc}$  the target-scattered neutron fluence in a given energy bin. For 14.8 MeV the factor

$$f_{E>13.5} = \frac{\sum_{E_i>13.5 \text{ MeV}} R_i \Phi_i}{\sum_i R_i \Phi_i} \quad (7.3)$$

has to be applied to correct the detector reading due to target-scattered neutrons. Here again,  $R_i$  is the response and  $\Phi_i$  is the sum of the unscattered and scattered neutron fluence for a certain energy bin. The values of the correction factors  $f_{us}$  and  $f_{>13.5}$  are summarized in Table 7.4.

**Table 7.4:** Ratio of the response of the Bonner spheres to direct neutrons to the response to direct and target-scattered neutrons. The Table gives  $f(E)_{us}$  as it is defined in Equation 7.2 for  $E=1.2$  MeV and 144 keV and  $f_{E>13.5}$  as it is defined in Equation 7.3 for  $E=14.8$  MeV.

| Sphere  | Energy    |           |           |
|---------|-----------|-----------|-----------|
|         | 14.8 MeV  | 1.2 MeV   | 144 keV   |
| 81Cd    | 0.96±0.03 | 0.94±0.01 | 0.97±0.02 |
| 81 mm   | 0.95±0.03 | 0.94±0.01 | 0.97±0.01 |
| 108 mm  | 0.96±0.02 | 0.95±0.01 | 0.98±0.01 |
| 133 mm  | 0.97±0.01 | 0.96±0.01 | 0.98±0.01 |
| 178 mm  | 0.98±0.01 | 0.97±0.01 | 0.98±0.01 |
| 233 mm  | 0.98±0.01 | 0.98±0.01 | 0.98±0.01 |
| Stanlio | 0.99±0.02 | 0.94±0.02 | 0.97±0.02 |
| Ollio   | 0.99±0.01 | 0.98±0.01 | 0.99±0.03 |

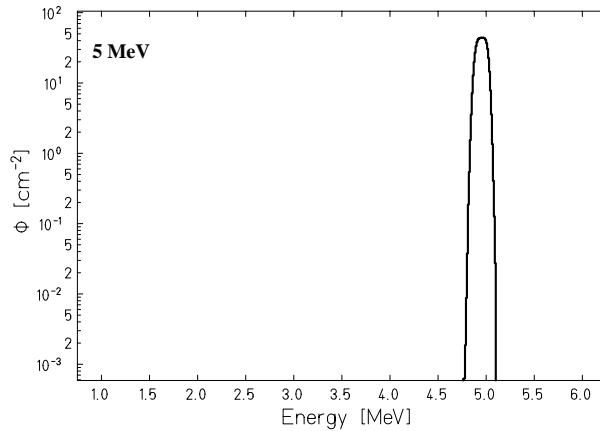


**Figure 7.6:** Unscattered neutron spectral distribution at the centre of the detector provided by [Sch01] for the mean neutron energy of  $E=5$  MeV.

At  $E=5$  MeV measurements done without gas filling become important in order to evaluate the contribution of neutrons that are produced in the entrance window. Table 7.5 shows the percentage of the detector reading from neutrons produced in a gas target without filling to one with gas filling, which is of the order of 1-2 %.

**Table 7.5:** Contribution of neutrons produced in the entrance window for a nominal neutron beam energy of  $E=5$  MeV. The table gives the percentage of the detector readings without gas filling compared to the ones with gas filling.

| Energy | Spheres |       |        |        |        |        |         |       |
|--------|---------|-------|--------|--------|--------|--------|---------|-------|
|        | 81Cd    | 81 mm | 108 mm | 133 mm | 178 mm | 233 mm | Stanlio | Ollio |
| 5 MeV  | 2.0 %   | 1.8 % | 1.4 %  | 1.3 %  | 1.2 %  | 1.0 %  | 1.4 %   | 0.9 % |

### 7.3 Data analysis and results

For all measurements with the Bonner spheres a pulse height spectrum of the  $^3\text{He}$  proportional counter was acquired in order to verify the proper functioning of the electronics. The count rates obtained were between 16 and 3200 ct/s for measurements without shadow cone, between 0.8 and 600 ct/s for measurements with shadow cones and between 3 and 30 ct/s for measurements without gas filling in the target. Thus no pile up in the counter occurred and no dead time corrections had to be applied as measurements in a high-intensity calibration field have shown (Chapter 9). The integral detector counts above threshold were for measurements without the shadow cone usually between 60000 and 100000 ct, for measurements with shadow cone between 10000 and 40000 ct and for measurements without gas filling usually between 5000 and 25000 ct in order to keep the statistical uncertainties of the measurements low.

The readings of the Bonner spheres were normalized to four of the five reference monitors which were running in parallel. Thus, a mean fluence response  $\langle R \rangle$  of each measurement was evaluated by using the calibration factors of the reference monitors obtained from the fluence measurements [Gul01]. The Geiger-Müller counter was not used for normalization, because it is a photon detector and cannot provide precise results in a neutron field.

Measurements without shadow cone lead to a raw fluence response  $\langle R_x \rangle$ , which results from direct neutrons, from neutrons scattered from the walls, in the air and in the target material. In order to obtain the fluence response of the Bonner spheres to direct neutrons only,  $\langle R \rangle$ , all contributions of the background, as studied in Section 7.2, have to be subtracted from the raw fluence response:

$$\langle R_{E=14.8} \rangle = (\langle R_x \rangle - \langle R_s \rangle) \cdot f_{E>13.5} \quad (7.4)$$

$$\langle R_{E=5} \rangle = \langle R_x \rangle - \langle R_s \rangle - \langle R_{ng} \rangle \quad (7.5)$$

$$\langle R_{E=1.2} \rangle = (\langle R_x \rangle - \langle R_s \rangle) \cdot f_{us}(1.2) \quad (7.6)$$

$$\langle R_{E=144} \rangle = (\langle R_x \rangle - \langle R_s \rangle) \cdot f_{us}(144) \quad (7.7)$$

where  $\langle R_{E=14.8} \rangle$ ,  $\langle R_{E=5} \rangle$ ,  $\langle R_{E=1.2} \rangle$  and  $\langle R_{E=144} \rangle$  are the mean fluence responses to direct neutrons of the energies  $E=14.8$  MeV, 5 MeV, 1.2 MeV and 144 keV, respectively,  $\langle R_s \rangle$  the mean fluence response from measurements with shadow cone,  $\langle R_{ng} \rangle$  the mean fluence response from measurements without gas filling,  $f_{E>13.5}$  the fraction of fluence response due to neutrons above  $E=13.5$  MeV and  $f(E)_{us}$  the fraction of fluence response due to direct neutrons. The results of the calibration measurements are shown in Table 7.6

**Table 7.6:** Experimental absolute mean fluence responses  $\langle R_{E=14.8} \rangle$ ,  $\langle R_{E=5} \rangle$ ,  $\langle R_{E=1.2} \rangle$  and  $\langle R_{E=144} \rangle$  for the nominal neutron energies  $E=14.8$  MeV, 5 MeV, 1.2 MeV and 144 keV, respectively, of the extended-range Bonner sphere set.

| Sphere  | Counts per unit neutron fluence [cm <sup>2</sup> ] |             |             |             |
|---------|--|-------------|-------------|-------------|
|         | 14.8 MeV   | 5 MeV       | 1.2 MeV     | 144 keV     |
| 81Cd    | 0.051±0.002  | 0.113±0.002 | 0.404±0.008 | 1.197±0.028 |
| 81 mm   | 0.041±0.002  | 0.119±0.008 | 0.421±0.008 | 1.199±0.033 |
| 108 mm  | 0.178±0.005  | 0.476±0.037 | 1.337±0.022 | 2.386±0.052 |
| 133 mm  | 0.396±0.007  | 1.008±0.052 | 2.201±0.030 | 2.848±0.102 |
| 178 mm  | 0.835±0.013  | 1.808±0.086 | 2.808±0.039 | 2.182±0.051 |
| 233 mm  | 1.241±0.016  | 2.226±0.113 | 2.263±0.031 | 0.984±0.030 |
| Stanlio | 0.179±0.004  | 0.159±0.005 | 0.369±0.008 | 0.951±0.020 |
| Ollio   | 0.816±0.010  | 1.085±0.039 | 0.909±0.012 | 0.192±0.006 |

## 7.4 Comparison of simulated to measured response

The comparison of the simulated responses with the measured ones allows to draw the following conclusions. If the ratio of the calculated to measured response is constant at all energies for a given sphere, the shape of the simulated response functions is correct. Then the value of this ratio is the wanted calibration factor for the Bonner sphere system.

In Section 6.2 two sets of response functions were presented. The first one is based on nominal sphere parameters, *i.e.* for *ideal* Bonner spheres, made of polyethylene of the same density and without significant gaps between the moderator layers. As it was shown in Section 6.2.1 this situation does not represent the reality. The

spheres are not completely spherical, the polyethylene density varies between the different spheres and an air-gap exists between the counter and the moderator, which was not possible to measure precisely. Therefore, a maximum deviation of these parameters was determined which resulted in a modified set of response functions. These modified response functions take into account the major sources of uncertainties. These are the air-gap which affects all spheres and additionally for Stanlio a slightly different polyethylene density. It is assumed that the true response functions are in between these two sets. The other uncertainties, like diameter and density (apart from Stanlio) variations, are of minor magnitude and therefore only their upper limits were calculated to be applied to the final results.

Figures 7.5 and 7.6 have shown that the direct neutrons produced in the target are not  $\delta$ -function like but show an energy distribution with a FWHM as given in Table 7.1 and characterized as  $\Phi_{us}$  in Section 7.2. The measured fluence responses, as presented in Section 7.3, are therefore not exactly discrete fluence responses at the energies  $E=14.8$  MeV, 5 MeV, 1.2 MeV and 144 keV, but responses to the spectral neutron fluences  $\Phi_{us}$ , which are very narrowly peaked around the nominal energies anyway. Hence the calculated response functions have to be folded with  $\Phi_{us}$  in order to match the experimental conditions. Tables 7.7 and 7.8 list these results for the nominal and modified response functions.

**Table 7.7:** Calculated absolute fluence response of the Bonner sphere set using the nominal response functions as described in Section 6.2. The quoted uncertainties are only statistical.

| Sphere  | Counts per unit neutron fluence [ $cm^2$ ] |                   |                   |                   |
|---------|--|-------------------|-------------------|-------------------|
|         | 14.8 MeV                                   | 5 MeV             | 1.2 MeV           | 144 keV           |
| 81Cd    | 0.060 $\pm$ 0.001                          | 0.169 $\pm$ 0.004 | 0.577 $\pm$ 0.013 | 1.334 $\pm$ 0.031 |
| 81 mm   | 0.051 $\pm$ 0.001                          | 0.172 $\pm$ 0.004 | 0.612 $\pm$ 0.014 | 1.435 $\pm$ 0.033 |
| 108 mm  | 0.187 $\pm$ 0.004                          | 0.553 $\pm$ 0.013 | 1.538 $\pm$ 0.035 | 2.533 $\pm$ 0.059 |
| 133 mm  | 0.404 $\pm$ 0.009                          | 1.102 $\pm$ 0.025 | 2.468 $\pm$ 0.055 | 2.899 $\pm$ 0.067 |
| 178 mm  | 0.832 $\pm$ 0.018                          | 1.977 $\pm$ 0.045 | 3.070 $\pm$ 0.068 | 2.235 $\pm$ 0.052 |
| 233 mm  | 1.241 $\pm$ 0.027                          | 2.412 $\pm$ 0.055 | 2.448 $\pm$ 0.054 | 1.006 $\pm$ 0.024 |
| Stanlio | 0.231 $\pm$ 0.014                          | 0.219 $\pm$ 0.012 | 0.511 $\pm$ 0.024 | 1.192 $\pm$ 0.043 |
| Ollio   | 0.907 $\pm$ 0.030                          | 1.261 $\pm$ 0.040 | 1.082 $\pm$ 0.034 | 0.209 $\pm$ 0.006 |

From Tables 7.7 and 7.8 it can be seen that the differences between nominal and modified response is largest for the small spheres such as the 81 mm and 81Cd

**Table 7.8:** Calculated absolute fluence response of the Bonner sphere set using the modified response functions as described in Section 6.2.1. The quoted uncertainties are only statistical.

| Sphere  | Counts per unit neutron fluence [ $cm^2$ ] |             |             |             |
|---------|--|-------------|-------------|-------------|
|         | 14.8 MeV                                   | 5 MeV       | 1.2 MeV     | 144 keV     |
| 81Cd    | 0.046±0.001                                | 0.126±0.002 | 0.453±0.005 | 1.186±0.014 |
| 81 mm   | 0.035±0.001                                | 0.116±0.002 | 0.435±0.005 | 1.177±0.011 |
| 108 mm  | 0.177±0.002                                | 0.534±0.003 | 1.539±0.009 | 2.642±0.014 |
| 133 mm  | 0.402±0.002                                | 1.125±0.003 | 2.569±0.009 | 3.111±0.023 |
| 178 mm  | 0.884±0.005                                | 2.106±0.007 | 3.370±0.012 | 2.483±0.014 |
| 233 mm  | 1.341±0.004                                | 2.653±0.008 | 2.785±0.012 | 1.212±0.009 |
| Stanlio | 0.166±0.002                                | 0.150±0.002 | 0.373±0.004 | 0.938±0.011 |
| Ollio   | 0.884±0.007                                | 1.265±0.004 | 1.088±0.004 | 0.219±0.004 |

spheres and Stanlio. These spheres are those most affected by the air-gap, as it is also illustrated in Figure 7.7, which shows the ratios between measured and calculated responses ( $R_m/R_c$ ) of each sphere for both the nominal and modified responses as a function of neutron energy. The straight lines indicate the weighted mean of the two sets of data, which are plotted with their weighted error. The nominal and modified responses differ by  $\sim 20\%$  for the 81Cd and 81 mm spheres and by  $\sim 25\%$  for Stanlio. For the other spheres the difference is less than 10 %, being smallest for Ollio. It should also be noted that the ratios,  $R_m/R_c$ , for the 81Cd and 81 mm spheres show large fluctuations around their mean values.

The weighted error of the mean ratio,  $\langle R_m/R_c \rangle$ , is 6.7 % for the 81Cd sphere and 5.1 % for the 81 mm sphere considering the nominal response functions. This can be reduced to 3.8 % for the 81Cd and to 2.9 % for the 81 mm sphere taking the modified response function into account. This fact suggests that the modified response is actually closer to the real situation than the nominal one.

In Figure 7.8 the same data are plotted, however, in a different way. The figure shows the ratio between measured and calculated response,  $R_m/R_c$ , considering the nominal and modified response functions for each energy for the different spheres. The straight lines are again the weighted mean,  $\langle R_m/R_c \rangle$ , of the ratios between measured and calculated nominal as well as modified responses. It can be seen that for  $E=14.8$  MeV, 1.2 MeV and 144 keV the weighted mean changes by less than 7 % between the nominal and modified data.

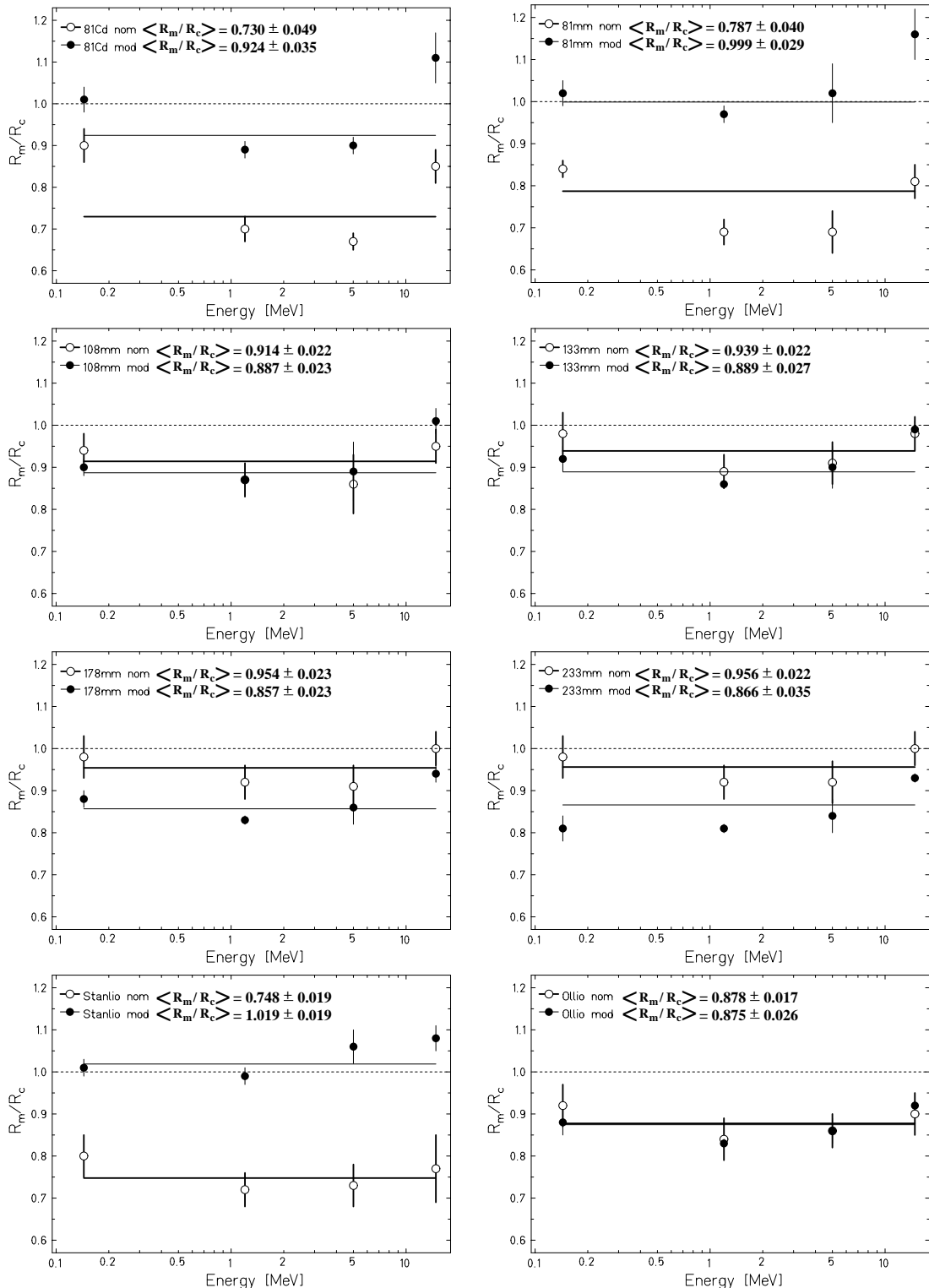


**Figure 7.7:** Ratios of the measured to the calculated nominal and modified responses of each Bonner sphere as a function of the neutron energy. The weighted mean and its weighted error are indicated as well for the two sets of data.

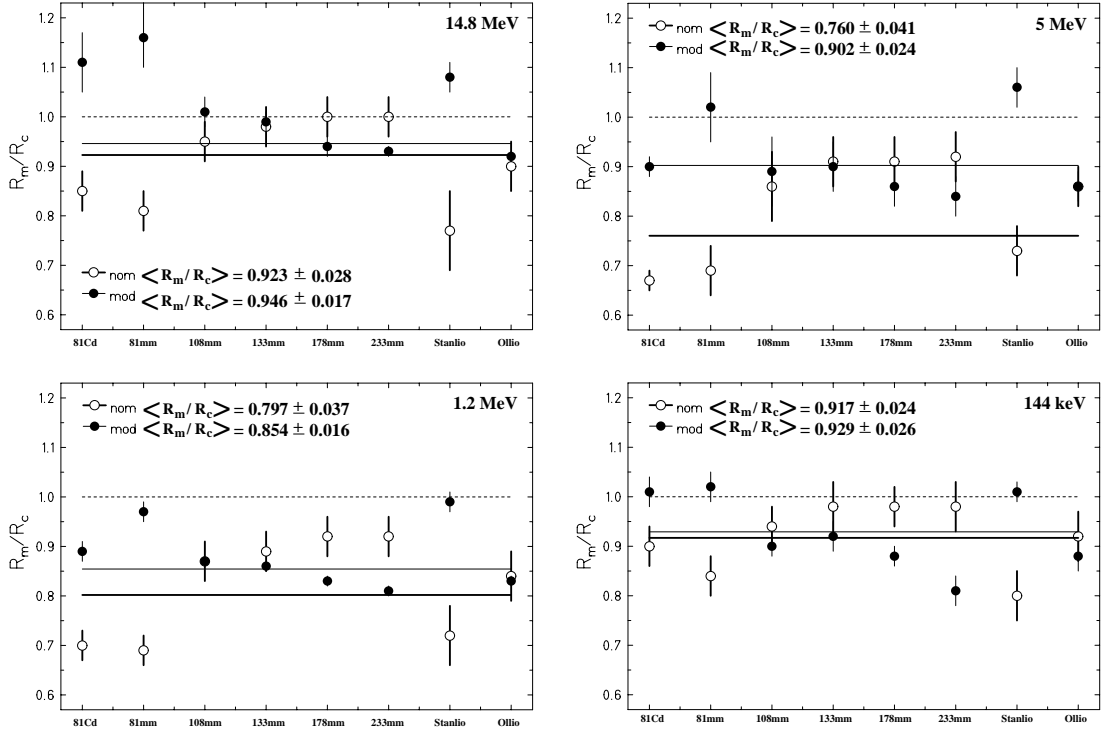


**Figure 7.8:** Ratios of the measured to the calculated nominal and modified responses for neutron energies  $E=14.8$  MeV, 5 MeV, 1.2 MeV and 144 keV given for the various Bonner spheres. The weighted mean and its weighted error are indicated as well for the two sets of data.

For  $E=5$  MeV in Figure 7.8 the difference is larger as compared to the other energies since the weighted mean of the nominal responses is ‘pulled down’ by the small statistical uncertainty of the 81Cd sphere. In general, the weighted errors of the mean ratios are reduced by up to a factor 2 for the modified responses as compared to the nominal ones, except for  $E=144$  keV where the two weighted errors are comparable.

Combining Figures 7.7 and 7.8 into two plots results in Figure 7.9. The plots show the average ratios of the measured to calculated responses,  $r = \langle R_m/R_c \rangle$ , over either all calibration energies for the different spheres or over all spheres at a given calibration energy. It can be observed that the weighted mean value of the average ratios,  $\langle r \rangle$ , do not differ much regarding the nominal and modified data set. Its difference is smaller than 5 %. The weighted errors of  $\langle r \rangle$  are in the left plot 3.2 % and in the right one 4.2 % considering the nominal response function data. It can be reduced to 2.6 % and 2.3 %, *i.e.* almost a factor 2, taking the modified response function data into account.

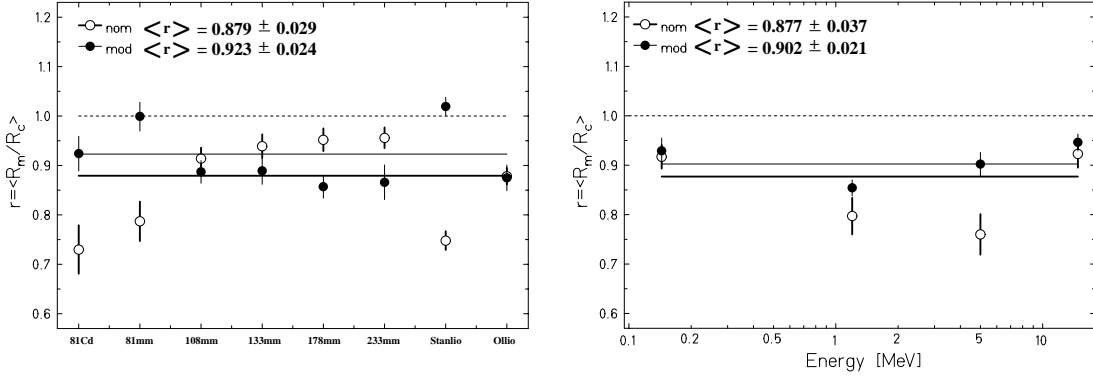


**Figure 7.9:** Mean ratios of the measured to the calculated nominal and modified responses. **Left:** averaged over all calibration energies for a given sphere. **Right** averaged over all spheres at a given calibration energy. The weighted mean of the mean ratios and its weighted error are indicated as well for both sets of data.

**Table 7.9:** Calculated mean absolute fluence response of the Bonner sphere set including the statistical uncertainties of the Monte-Carlo simulations as well as uncertainties due to variations of the sphere geometry, density and diameter.

| Sphere  | Counts per unit neutron fluence [ $cm^2$ ] |                   |                   |                   |
|---------|--|-------------------|-------------------|-------------------|
|         | 14.8 MeV                                   | 5 MeV             | 1.2 MeV           | 144 keV           |
| 81Cd    | 0.053 $\pm$ 0.008                          | 0.148 $\pm$ 0.023 | 0.515 $\pm$ 0.069 | 1.260 $\pm$ 0.104 |
| 81 mm   | 0.043 $\pm$ 0.008                          | 0.144 $\pm$ 0.029 | 0.524 $\pm$ 0.094 | 1.306 $\pm$ 0.149 |
| 108 mm  | 0.182 $\pm$ 0.014                          | 0.544 $\pm$ 0.042 | 1.539 $\pm$ 0.115 | 2.588 $\pm$ 0.200 |
| 133 mm  | 0.403 $\pm$ 0.022                          | 1.114 $\pm$ 0.064 | 2.519 $\pm$ 0.149 | 3.005 $\pm$ 0.199 |
| 178 mm  | 0.858 $\pm$ 0.053                          | 2.042 $\pm$ 0.131 | 3.220 $\pm$ 0.233 | 2.359 $\pm$ 0.181 |
| 233 mm  | 1.291 $\pm$ 0.087                          | 2.533 $\pm$ 0.186 | 2.617 $\pm$ 0.222 | 1.109 $\pm$ 0.120 |
| Stanlio | 0.199 $\pm$ 0.037                          | 0.185 $\pm$ 0.038 | 0.442 $\pm$ 0.076 | 1.065 $\pm$ 0.145 |
| Ollio   | 0.896 $\pm$ 0.057                          | 1.263 $\pm$ 0.076 | 1.085 $\pm$ 0.065 | 0.214 $\pm$ 0.014 |

As already mentioned the nominal and modified response functions represent the two extremes of the real situation. Thus one can specify a calculated mean response by taking the mean value of the nominal and modified response. Its uncertainty is given by several independent factors: the half difference between the minimum and maximum of the two responses, the statistical uncertainties of the Monte-Carlo simulations and the uncertainties due to variations in density and diameter of the spheres for which, apart from Stanlio, only an upper limit was estimated (details can be found in Section 6.2). Table 7.9 shows the calculated mean responses of the Bonner spheres for the four calibration energies.

The calculated mean responses (Table 7.9) can be compared to the experimental ones (Table 7.6) in the same way as already done before. Figure 7.10 shows the ratio between the experimental responses and calculated mean responses,  $R_m/R_c$ , for each sphere as a function of energy. The errors have been evaluated in analogous way to those stated in Tables 7.6 and 7.9. The straight lines indicate the weighted mean value of the data points,  $\langle R_m/R_c \rangle$ . Compared to Figure 7.7 it can clearly be seen that the fluctuation of the ratios,  $R_m/R_c$ , around their mean value is reduced. Also, the weighted mean values agree for each sphere within the uncertainties. Figure 7.10 also shows that for some spheres, especially for the 81 mm sphere and Stanlio, the uncertainties of the single data points have been estimated too conservatively (see also Section 6.2).

The weighted average of all 32 ratios  $R_m/R_c$ , which are plotted in Figure 7.10, results to an overall factor  $f$  which describes the difference between experimental and calculated data. It is for the 2 atm-detector:

$$f = \frac{R_m}{R_c} = 0.899 \pm 0.014 \quad \text{with} \quad \chi^2 = 0.42 \quad (7.8)$$

The error of 0.014 represents the weighted error on the average of all 32 measurements. The  $\chi^2$  value of  $\chi^2=0.42$  also indicates that in general the errors were estimated conservatively.

As it can be seen,  $f$ , the ratio between the experimental and calculated response of the Bonner sphere system is not unity. The reasons can be diverse: *e.g.* for the MC simulations the effective volume of the  $^3\text{He}$  proportional counter was considered as the total spherical volume of the counter. Since the  $^3\text{He}$  proportional counter was a commercial one the technical drawings of it were not available. However, the inner structure of the counter, *i.e.* the exact placement of the electrodes, can affect the effective volume of the detector. In addition, the real  $^3\text{He}$  partial pressure cannot be measured and therefore applied precisely to the MC simulations since the counter is sealed. The MC simulations implement only the nominal pressure of the counter. However, measurements with thermal neutrons [Tho88, Tho94] have shown that counters of the same type and the same nominal pressure behave (with respect to fluence response) as if they have various pressures, the dispersion observed being about 12 %.

The factor  $f$ , the ratio between the calibration measurements and the calculations, determines indirectly the unmeasurable detector parameters like the effective volume or the gas pressure of the counter. The reciprocal value of  $f$  gives the calibration factor of the Bonner sphere system for this specific  $^3\text{He}$  proportional counter. It has to be applied to all the experimental data in order to compare them correctly to the simulated one.

$$f_c = 1.112 \pm 0.017 \quad (7.9)$$

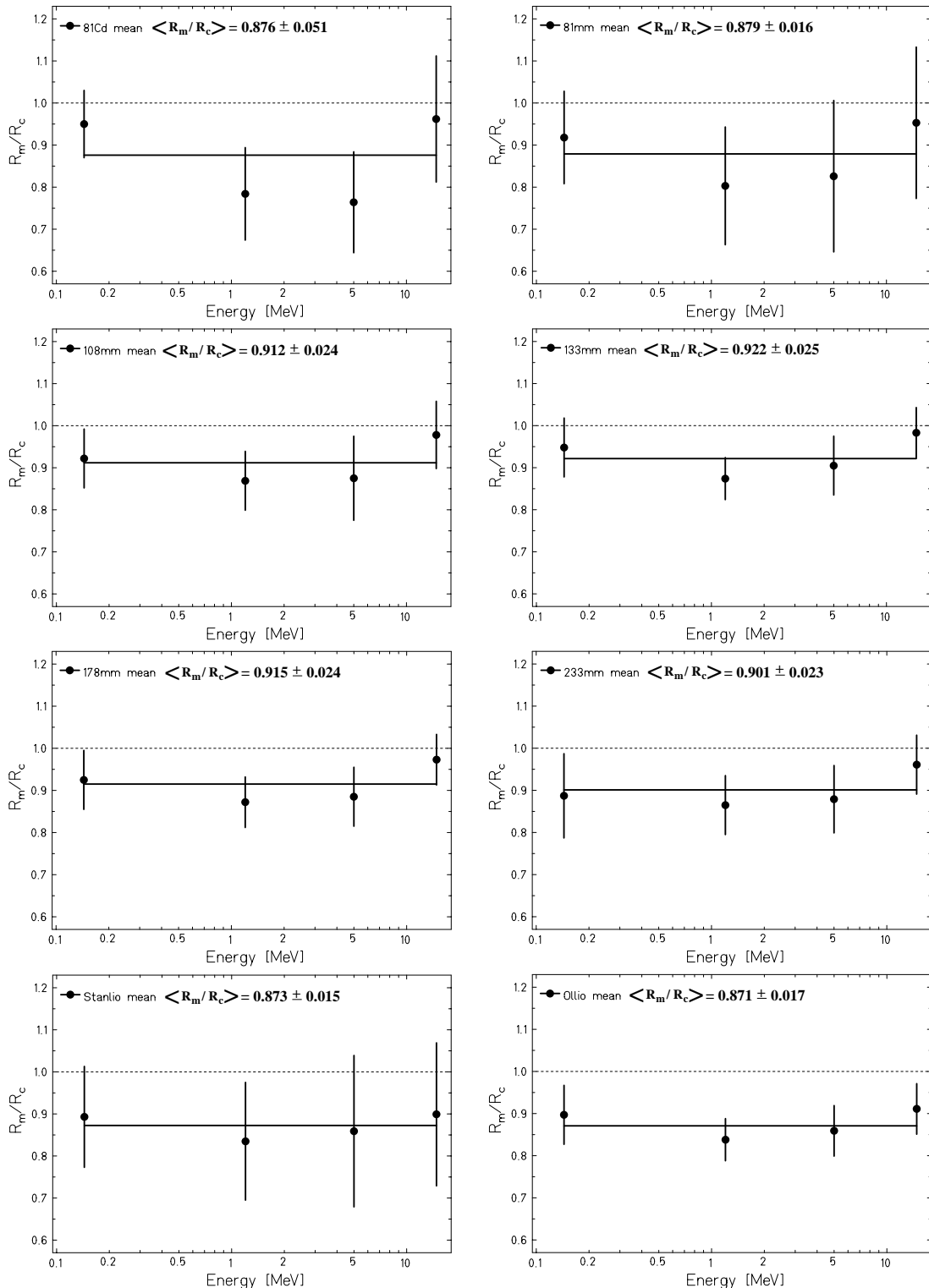


**Figure 7.10:** Ratios of the measured responses to the calculated mean responses of each Bonner spheres as a function of neutron energy. The error bars include the statistical uncertainties of the measurement, the Monte-Carlo simulations as well as the uncertainties due to the variations of the sphere geometry, density and diameter.

# Chapter 8

## Measurements with radionuclide neutron sources

Experiments of the extended-range Bonner sphere spectrometer with radionuclide neutron sources were performed in collaboration with the University of Milan and another CERN group and are extensively described in [Cap00] and [Bir01]. The analysis of these measurements included only the nominal response functions of the spheres. This chapter gives a brief summary of the results and revises them according to the modified response functions developed in this work.

### 8.1 Experimental set-up

The measurements were carried out in the calibration laboratory at CERN. A  $^{241}\text{Am}$ -Be source was used with an emission rate of  $6.94 \times 10^5$  neutrons per second, *i.e.* a flux of  $5.52 \text{ s}^{-1}\text{cm}^{-2}$  at 1 m distance. In order to evaluate the response of the BSS to the pure Am-Be field the reading had to be corrected for all additional effects, including those originating from the detector size and from neutron scattering in the air and by the laboratory walls. This was done by applying the semi-empirical method of calibration procedures described in the report [ISO99b] of the International Organization for Standardization.

### 8.2 Results

The computed response functions of the extended BSS to monoenergetic neutrons were folded with the spectral fluences of an  $^{241}\text{Am}$ -Be source for the comparison of the experimental and calculated detector response to the source. The spec-

**Table 8.1:** Experimental and calculated detector responses (counts per unit fluence) of the extended-range Bonner sphere spectrometer to neutrons from an Am-Be source using both the nominal and the modified response functions for the analysis including the statistical uncertainties of the experiment and the MC simulations. The last column gives the mean of the previous two. Its error includes the statistical uncertainties of the MC simulations as well as uncertainties due to variations of the sphere geometry, density and diameter.

| Sphere  | Counts per unit neutron fluence [cm <sup>2</sup> ] |                     |                     |                      |
|---------|--|---------------------|---------------------|----------------------|
|         | Experimental                                       | Calc <sub>nom</sub> | Calc <sub>mod</sub> | Calc <sub>mean</sub> |
| 81Cd    | 0.280±0.006  | 0.34±0.02           | 0.28±0.001          | 0.31±0.04            |
| 81 mm   | 0.274±0.008  | 0.36±0.03           | 0.27±0.003          | 0.32±0.06            |
| 108 mm  | 0.835±0.022  | 0.91±0.06           | 0.88±0.044          | 0.90±0.10            |
| 133 mm  | 1.502±0.029  | 1.48±0.10           | 1.53±0.015          | 1.51±0.13            |
| 178 mm  | 2.180±0.043  | 2.14±0.15           | 2.31±0.139          | 2.23±0.22            |
| 233 mm  | 2.241±0.045  | 2.26±0.16           | 2.47±0.207          | 2.37±0.30            |
| Stanlio | 0.319±0.008  | 0.36±0.03           | 0.26±0.044          | 0.31±0.07            |
| Ollio   | 1.016±0.020  | 1.08±0.08           | 1.11±0.088          | 1.10±0.13            |

trum of the Am-Be source was taken from [ISO99a]. Table 8.1 summarizes the detector response obtained by using the nominal and modified response functions in the folding. The experimental data and the calculated data using the nominal response functions,  $Calc_{nom}$ , were taken from [Bir01], while the calculated data using the modified response functions,  $Calc_{mod}$ , and the mean ones,  $Calc_{mean}$ , were calculated from the result of this thesis. From Table 8.1 and Figure 8.1 it can be seen that the measurements with the smallest spheres (81Cd, 81 mm and Stanlio) show large deviations from the calculations with the nominal response functions. This result was interpreted in [Bir01] as the limitation of the semi-empirical method in correcting large influences of scattering neutrons from the laboratory walls. The neutron scattering was for the 81Cd and 81 mm spheres of the same order as the reading to direct neutrons, for the Stanlio ~60 % and for all the others less than 6 %.

However, applying the modified response functions and comparing experimental and calculated data (Figure 8.1) shows that the experimental detector response of the smallest sphere changes by up to 30 %. As already mentioned, the two sets of response functions represent the two extremes of the real situation. Thus, a mean

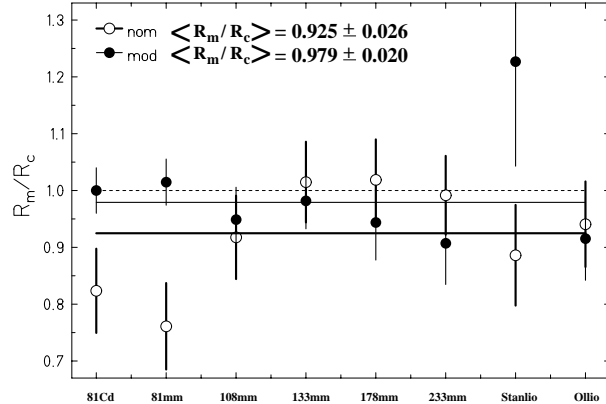


**Figure 8.1:** Ratio of the measured detector responses to the calculated ones derived from both the nominal and the modified response functions for the Bonner spheres exposed to  $^{241}\text{Am-Be}$ .

response  $\text{Calc}_{\text{mean}}$  was calculated from the average of  $\text{Calc}_{\text{nom}}$  and  $\text{Calc}_{\text{mod}}$  (Table 8.1). The uncertainty is given by half the difference between minimum and maximum, the statistical uncertainties from the Monte-Carlo calculations and the uncertainties due to variation of the density and the diameter as described in sections 6.2 and 7.3. The calculated mean detector response can be compared to the experimental ones in the same way as already done in Figure 8.1. This leads to an overall factor between experiment and simulation of  $f_{\text{Am-Be}}=0.949\pm 0.038$ .  $f_{\text{Am-Be}}$  is comparable to  $f=0.899\pm 0.014$  (Equation 7.8) determined by the calibration measurements, but less reliable since the measurement conditions in the CERN calibration laboratory were not as precise as at the PTB calibration facility. Nevertheless  $f_{\text{Am-Be}}$  and  $f$  agree very well within their uncertainties.

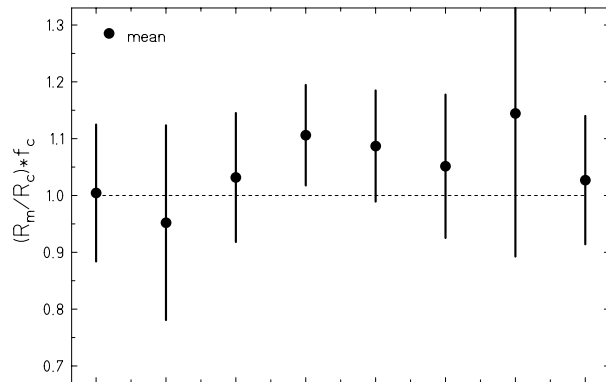


**Figure 8.2:** Ratio of the normalized measured response to the calculated mean one for the Bonner spheres exposed to  $^{241}\text{Am-Be}$ .

Figure 8.2 shows the ratio of the normalized experimental response compared to the calculated mean response after applying the calibration factor  $f_c$  from Equation 7.9. It can be seen that the experimental and calculated responses of the Bonner spheres agree very well within the uncertainties.

# Chapter 9

## Measurements in reference fields

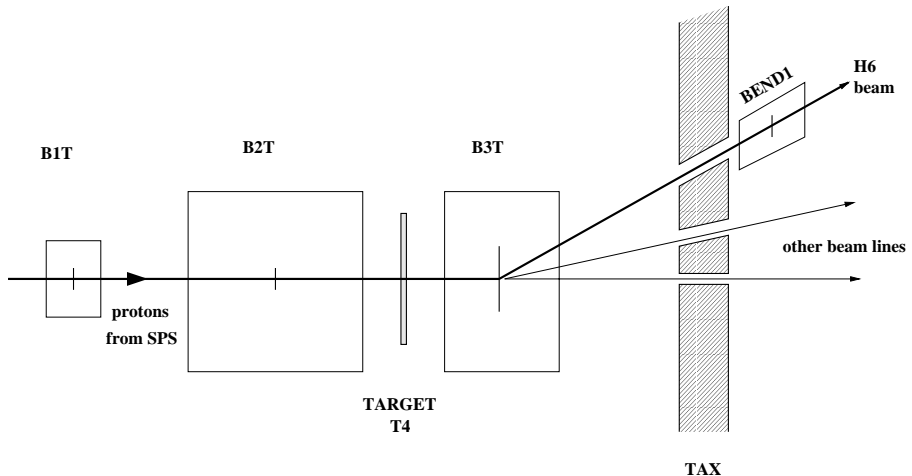
After the calibration at the PTB, the new extended-range Bonner sphere spectrometer was tested in a well characterized high-energy neutron field. Such a reference facility is available at CERN since 1992. This ‘High Energy Reference Field’ (CERF) facility is located in one of the H6 beam lines in the North Experimental Area of the SPS.

### 9.1 H6 area

The H6 beam is derived from the T4 target station served by a primary proton beam with a momentum of  $p=450$  GeV/c and since July 2000 by protons of  $p=400$  GeV/c with typical intensities of several  $10^{12}$  protons per spill. The target is made of a  $2\text{ mm} \times 160\text{ mm}$  beryllium plate 300 mm long. The beam line can be operated to transport secondary particles in the momentum range  $5\text{ GeV/c} \leq p \leq 205\text{ GeV/c}$ . The CERF facility is situated about 405 m downstream of the Be-target [Els98b].

The layout of the target station T4 is shown schematically in Figure 9.1. The direction of incidence of the primary proton beam onto the target is governed by two magnets, B1T and B2T. Magnets B3T and BEND1(H6) serve to direct the secondary particles of wanted sign, momentum and production angle into the H6 line and to deviate the remaining beam onto the dump. Production angles up to 15 mrad are attainable with protons impinging on the target along the beam axis [Amb99]. Larger production angles (up to 30 mrad) can be obtained by changing the angle of incidence of the primary beam on the target by means of the magnets B1T and B2T.

Three kinds of collimators serve to define the horizontal and vertical acceptance and the transmitted momentum interval. They can be opened up to  $\pm 45$  mm.



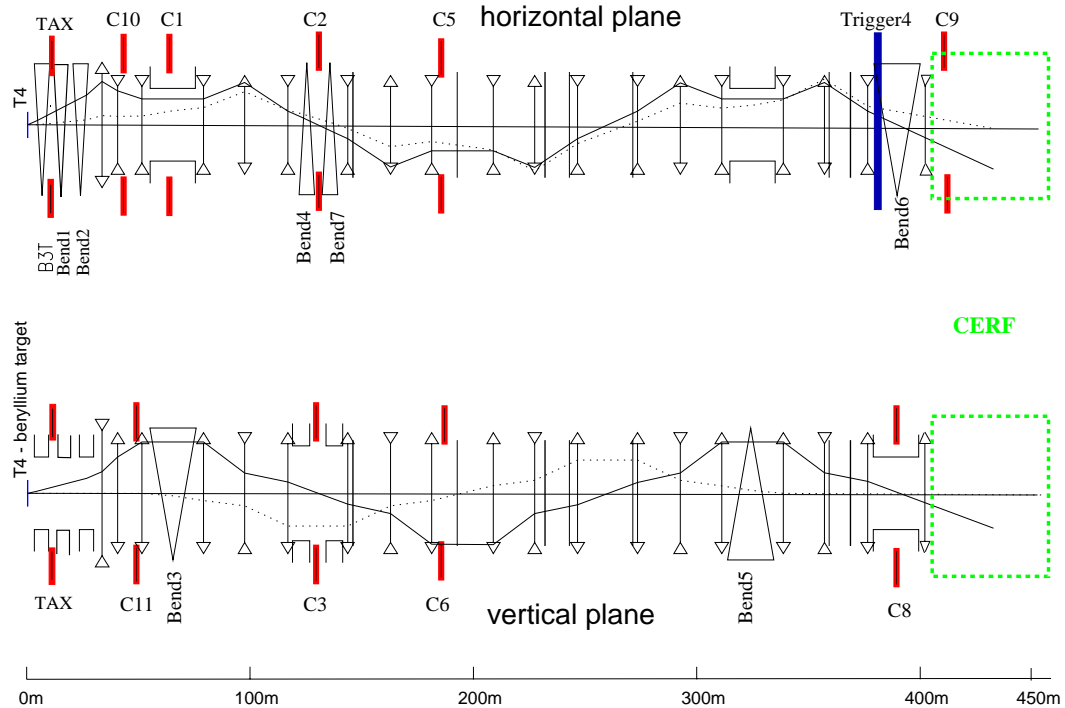
**Figure 9.1:** Schematic plan of target station T4 [Amb99].

Table 9.1 gives a summary of the collimator settings that are required for CERF measurements.

**Table 9.1:** Collimator settings for CERF measurements.

| Collimator | Acceptance   | Setting     | Distance from T4 |
|------------|--------------|-------------|------------------|
| C1         | horizontal   | $\pm 20$ mm | 64 m             |
| C2         | $\Delta p/p$ | $\pm 20$ mm | 125 m            |
| C3         | $\Delta p/p$ | tunable     | 125 m            |
| C5         | horizontal   | tunable     | 188 m            |
| C6         | vertical     | $\pm 30$ mm | 188 m            |
| C8         | $\Delta p/p$ | $\pm 45$ mm | 380 m            |
| C10        | horizontal   | $\pm 45$ mm | 44 m             |
| C11        | vertical     | $\pm 45$ mm | 48 m             |

Several scintillators and Multiwire Proportional Chambers (MWPC) located along the beam line are used to monitor the steering of the beam and to record the spot size and the position of the beam. The scintillator *Trigger4* (called Tr4) served to calibrate the beam monitor of CERF, a Precision Ionization Chamber (PIC), in 1999. Figure 9.2 shows the layout of the H6 beam line indicating the position of magnets, collimators, beam scintillators, MWPCs and the CERF facility.



**Figure 9.2:** Elements of the H6 beam optics in the horizontal and vertical planes. Not to scale. The solid line indicates the excursion of a particle with an angular offset at T4 (1 mrad) and the dotted line shows the trajectories of on-axis particles with a momentum different from the nominal one ( $\Delta p/p \sim 1\%$ ) [Amb99].

## 9.2 CERF beam monitor

The beam at CERF is monitored by a Precision Ionization Chamber (PIC), which is installed about 405 m downstream the T4 production target. It is an open air ionization chamber with cylindrical shape. Its sensitive volume is 0.86 litres (diameter: 185 mm, active length: 32 mm). The exact design of the PIC is described in [Aro93]. The charge produced by ionization of the beam in this volume is collected at a capacitor. Whenever this charge attains a predefined threshold, the capacitor is discharged and issues one count that is a measure of the number of beam particles which have produced this charge.

The PIC serves to normalize the experimental data to the number of particles in the H6 beam. Thus an exact knowledge of the PIC performance and its calibration factor is essential.

### 9.2.1 Performance tests of the CERF beam monitor

The proper functioning of the PIC was tested in the calibration laboratory of CERN with gamma sources, in order to investigate the warming-up time, the noise, the linearity, the leakage current and the region of ion saturation of the chamber.

The voltage of the PIC was set to the nominal value of  $U=250$  V for all measurements; only for determining the region of ion saturation the voltage was varied between  $U=11$  V and  $U=330$  V. The chamber was irradiated with gamma sources of different activity in order to cover four orders of magnitude in air kerma rate. The measuring time differed depending on the type of measurements. The experiments were performed on two different days (25th November and 14th December 1999). During these measurements the air pressure, the room temperature and the relative humidity were  $p=982 \pm 1$  hPa,  $T=294.65 \pm 0.3$  k,  $rH=25.7 \pm 1.5\%$  and  $p=951 \pm 1$  hPa,  $T=296.75 \pm 0.4$  k,  $rH=28.7 \pm 1.5\%$ , respectively. The factor for correcting variations of temperature and pressure for an open air ionization chamber is:

$$k_p = \frac{p_0}{p} \cdot \frac{T}{T_0}. \quad (9.1)$$

Since it was of interest in comparing only the results relative to each other:

$$\frac{R_1}{R_2} = \frac{T_1}{T_2} \cdot \frac{p_2}{p_1} \quad \Rightarrow \quad \frac{R_1}{R_2} = 0.96 \pm 0.03 \quad (9.2)$$

was obtained, where  $R_1$ ,  $T_1$ ,  $p_1$  and  $R_2$ ,  $T_2$ ,  $p_2$  are the count rate, the absolute temperature and the air pressure during the measurements in November and December, respectively.

#### 9.2.1.1 Stabilisation tests

On 14th December 1999, data were taken immediately after switching on the PIC. This gives information about the warming-up time of the electronics until it reaches stable working conditions. The measurements were performed at air kerma rates ranging from  $\dot{K}_a=5$   $\mu\text{Gy}/\text{h}$  to 400  $\mu\text{Gy}/\text{h}$ . Figure 9.3 shows the sensitivity of the PIC as a function of air kerma rate. The values obtained from the PIC were corrected for variation of temperature and pressure according to equation 9.2. The solid line in the plot is drawn to guide the eye. As can be clearly seen it takes about two hours until stable experimental conditions are established.

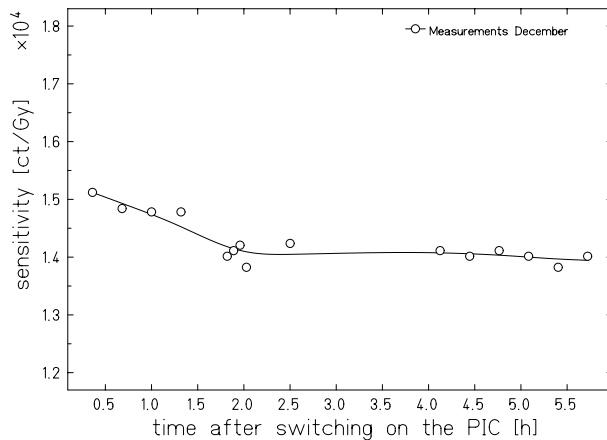


**Figure 9.3:** Sensitivity of the PIC as a function of time after switching on the power (symbols). The solid line is drawn to guide the eye.

### 9.2.1.2 Noise

Long term measurements in the calibration laboratory showed that the electronics of the PIC is not affected by any electronic noise. There were no counts due to noise during this period.

### 9.2.1.3 Linearity tests

The linearity tests for the PIC were performed during both measurements by irradiating the PIC with sources of the isotope  $^{137}\text{Cs}$  of different activities to obtain an air kerma rate ranging from  $K_a=5 \mu\text{Gy}/\text{h}$  up to  $30 \text{ mGy}/\text{h}$ . The results of these experiments are presented in Figure 9.4.

It shows the number of counts per second as a function of air kerma rate for the two measurements. The data from the second measurement were additionally corrected for temperature and pressure variation (see Equation 9.2) in order to be able to compare the results. The fit through the two data sets gives straight lines with the following parameters for  $y = k_1 \times x + k_0$ :

Measurement November:

$$\begin{aligned}
 k_0 &= (-0.06 \pm 0.01) \frac{ct}{s} \\
 k_1 &= (0.0146 \pm 0.0001) \frac{ct \cdot h}{s \cdot \mu\text{Gy}} \\
 \chi^2/ndf &= 0.85
 \end{aligned} \tag{9.3}$$

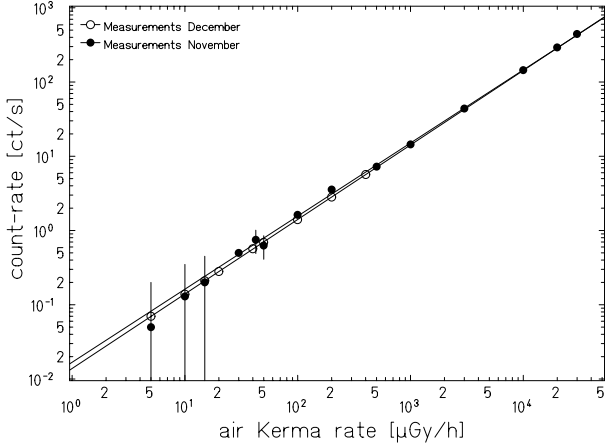


**Figure 9.4:** Measured count rate as a function of air kerma rate for the two measurements (symbols). The lines are linear fits through the experimental data points.

Measurement December:

$$\begin{aligned}
 k_0 &= (-0.0007 \pm 0.0025) \frac{ct}{s} \\
 k_1 &= (0.0141 \pm 0.0002) \frac{ct \cdot h}{s \cdot \mu Gy} \\
 \chi^2/ndf &= 0.11
 \end{aligned} \tag{9.4}$$

Thus the results of the fits in Figure 9.4 prove the linearity of the PIC in the effective range between an air kerma of rate  $\dot{K}_a=5 \mu\text{Gy}/\text{h}$  and  $30 \text{ mGy}/\text{h}$ . It can also be seen that the two fits coincide very well which confirms the reproducibility of the ionization chamber.

#### 9.2.1.4 Leakage currents

Another important task was to investigate if any leakage currents occur in the PIC. This is of major interest for experiments in the H6 beam with extremely low beam intensities, *e.g.* 10-50 PIC counts per SPS spill. Under these conditions, a leakage of the capacity of the digitizer in the PIC during the time between two spills ( $\sim 12 \text{ s}$ ) could falsify the PIC response dramatically.

In order to investigate this effect, the results obtained from the linearity tests (see Chapter 9.2.1.3) were divided by the used air kerma rate. The values at  $\dot{K}_a=5, 10$  and  $15 \mu\text{Gy}/\text{h}$  of the November measurements were dismissed since they show error bars of more than 100%. Figure 9.5 shows the number of counts

per unit dose as a function of air kerma rate for the measurements in November and December. The solid line gives the fit of the experimental data with fit parameter  $k_0$ :

$$k_0 = (5.20 \pm 0.06) \times 10^7 \frac{ct}{Gy} \quad (9.5)$$

$$\chi^2/ndf = 0.94$$

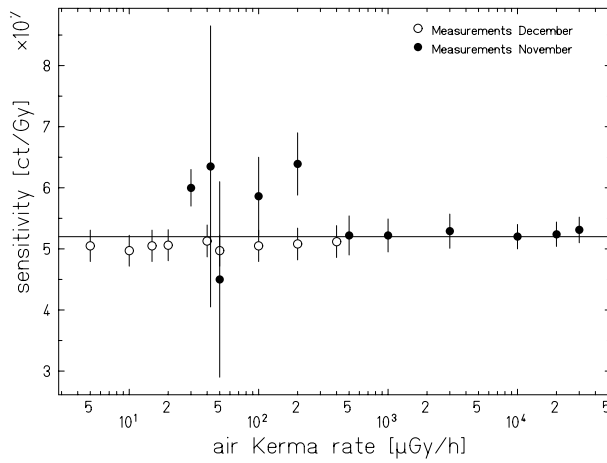


**Figure 9.5:** Count rate as a function of air kerma rate of measurements in November and December (symbols). The solid line is a fit through the experimental data.

For these data an additional error had to be taken into account to the usual statistical errors of the measurements, which was derived from the uncertainty of the air kerma rate  $\dot{K}_a$  of 2.2 % [Ott99]. The lowest air kerma rate  $\dot{K}_a = 5 \mu\text{Gy}/\text{h}$  correlates to about 1 count every  $t = 13 \text{ s}$ . This reproduces very well the spill cycle in H6 of about  $t = 14 \text{ s}$ . If there was a leakage current of the PIC during this period a decrease of the count rate towards low air kerma rates would be observed. As seen from Figure 9.5 this is not the case. This means that the collecting capacitor of the PIC does not have any significant leakage between two SPS spills.

### 9.2.1.5 Region of ion saturation

In an ionization chamber one can always find an equilibrium between recombination and separation of the produced ion pairs depending on the applied voltage. The separated ion pairs are collected at the electrode and thus contribute to an ion current. At a sufficiently high applied voltage, the electric field is strong

enough to suppress recombination and all the originally produced charges contribute to the ion current. Increasing the voltage further cannot increase the ion current because all charges are already collected. This is called the region of ion saturation in which an ionization chamber should be operated [Kno79]. Under these conditions the ion current indicates correctly the rate of formation of all charges due to ionization within the active volume of the chamber. If that is not the case correction factors have to be applied to obtain correct results. These correction factors depend strongly on the dose rate to which the ionization chamber is exposed. The higher the dose rate and thus the space charge, the higher is the recombination probability and the electric field needed to suppress the recombination.

In the following experiment it was investigated whether the PIC is still working in the region of ion saturation for the maximum obtainable air kerma rate in the calibration laboratory. For this purpose the PIC was irradiated with an air kerma rate of  $\dot{K}_a=30$  mGy/h for different voltages between  $U=11$  V and 330 V.

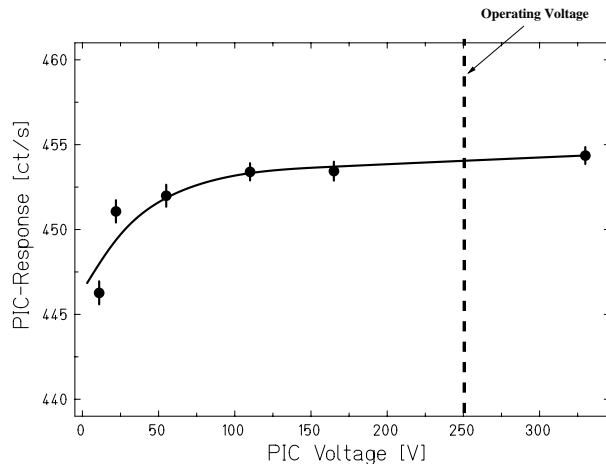


**Figure 9.6:** PIC count rate as a function of PIC voltage. The operating voltage of  $U=250$  V lies in the region of ion saturation.

Figure 9.6 gives the results of these measurements in a plot of PIC count rate as a function of the PIC voltage. It can be seen that the PIC operating voltage of  $U=250$  V lies within the region of ion saturation for air kerma rates up to 30 mGy/h produced by photon irradiation.

### 9.2.2 Recombination losses of the CERF beam monitor operating in the H6 beam

The measurements discussed in Section 9.2.1.5 have shown that the PIC is operating within the region of ion saturation for homogeneous gamma irradiation with air kerma rates up to  $K_a=30$  mGy/h. Since at CERF the beam consists of hadrons with dimensions of typically a few centimetres the results obtained from the gamma measurements are not easily adaptable to the H6 environment. Therefore voltage characteristic curves of the PIC for different H6 beam intensities were recorded. For this purpose the collimator settings were varied in order to obtain PIC count rates between  $\sim 310$  and  $\sim 22400$  counts/spill (see Table 9.2).

**Table 9.2:** Parameters during the measurements of the voltage characteristic curves of the PIC.

| Saturation PIC-Rate<br>[ct/spill] | Beam Fluctuation<br>[%] | Settings    |             |
|-----------------------------------|-------------------------|-------------|-------------|
|                                   |                         | Collimator3 | Collimator5 |
| $\sim 310$                        | 2.4                     | 1           | 3           |
| $\sim 6300$                       | 7.5                     | 15          | 20          |
| $\sim 10800$                      | 3.2                     | 30          | 20          |
| $\sim 16800$                      | 5.2                     | 20          | 15          |
| $\sim 19600$                      | 4.1                     | 20          | 20          |
| $\sim 22400$                      | 3.3                     | 25          | 25          |

For each collimator setting data were taken for the voltages  $U=25$  V, 50 V, 100 V, 150 V, 200 V, 300 V, 400 V and 500 V. Additionally, the number of primary protons on the T4 target was recorded in order to correct the PIC reading due to beam intensity fluctuations. Although, the measurements were performed in a period of very stable beam conditions. The half difference between the maximum and minimum beam intensity during the data acquisition of each saturation curve lies between 2.4% and 7.5%.

For each voltage setting up to five PIC responses per spill and the respective proton intensities on T4 per spill were recorded. In order to correct slight beam fluctuations, the quantity

$$\left\langle \left. \frac{\text{PICcount/spill}}{p_{T4}/\text{spill}} \right|_V \right\rangle \cdot \left. \langle p_{T4}/\text{spill} \rangle \right|_{\text{collset}} \quad (9.6)$$

which is the average of the PIC count rates ( $PIC_{count}/spill$ ) normalized to the proton rate on T4 ( $p_{T4}/spill$ ) for one voltage setting, multiplied with the mean proton rate for each collimator setting is plotted in Figure 9.7 as a function of PIC voltage and beam collimator setting. The uncertainty derives from error propagation of the single standard deviations.

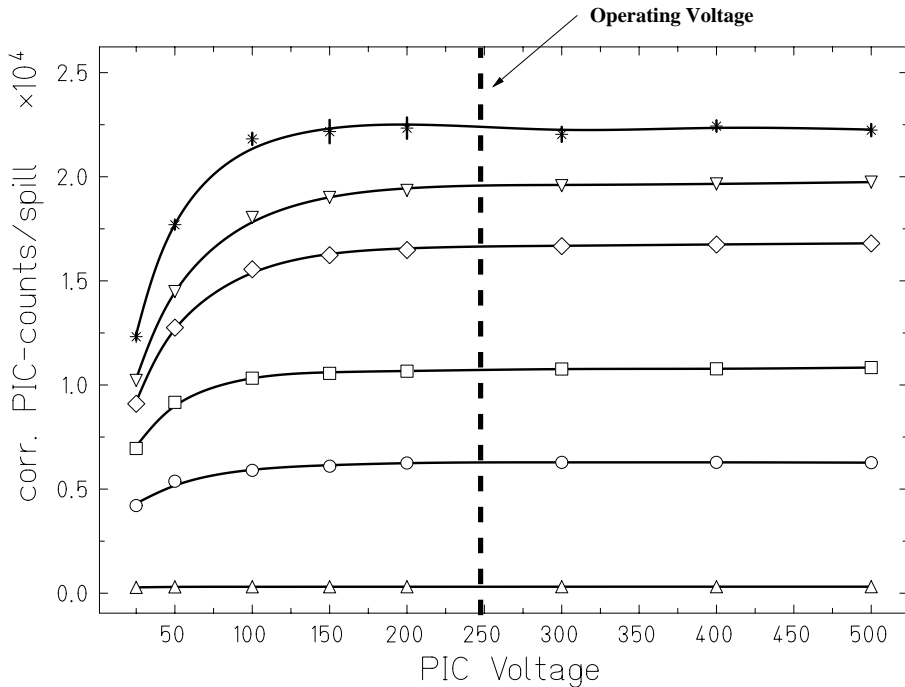


**Figure 9.7:** Voltage characteristic curves of the PIC for different beam intensities, *i.e.* different collimator settings (symbols) as given in Table 9.2. The PIC count rate is corrected for slight beam fluctuations.

Figure 9.7 shows clearly that the nominal voltage setting of the PIC  $U=250$  V lies within the uncertainties in the region of ion saturation for all measured H6 beam intensities. Thus up to about  $22400$  PIC counts per spill no correction factors due to recombination losses are required for the CERF beam monitor.

### 9.2.3 Calibration of the CERF beam monitor

The PIC was calibrated for the first time in 1993/94 in a series of activation measurements, using plastic scintillators, graphite plates and polyethylene foils [Car93, Hoo93, Liu93, Roe94, Ste94a, Ste94b]. These measurements gave a calibration factor of  $2.2 \times 10^4$  beam particles per PIC count, with an uncertainty of  $\pm 10\%$ . In 1998 a verification of the PIC calibration was done by comparing the responses of the PIC with three scintillators installed in the H6-beam line

[Els98a]. The results of these measurements showed that the calibration factor is in agreement with the 1993/94 measurements.

In 1999 the PIC was calibrated again with beam scintillators, however in a more precise way, *i.e.* by measuring the background and subtracting it from the detector signals, by correcting the scintillator signal according to its dead time, and by performing a detailed error analysis.

### 9.2.3.1 Experimental set-up

Low-intensity measurements were carried out in the H6 beam line from 5 to 13 August 1999 within the ATLAS background benchmarking measurements [Gsc00a] with a beam of  $p=120$  GeV/c and  $p=40$  GeV/c positive hadrons. The total SPS cycle had a period of  $t=14.4$  s with a spill of  $t=2.58$  s. Details about the data acquisition and analysis can be found in [Gsc00b]. Here only the high-intensity measurements are presented and compared with the results of the low-intensity ones.

The high-intensity measurements were performed in the H6 beam line on 27 May 1999 within the CERF runs with positive hadrons of  $p=120$  GeV/c. The total SPS cycle of  $t=14.4$  s had a spill of  $t=2.37$  s [Ard00].

The H6 beam consists of different fractions of protons, pions and kaons depending on the beam momentum. The composition of the beam at the position of the PIC is shown in Table 9.3 [Vin99].

**Table 9.3:** *H6 beam particle composition for  $p=40$  GeV/c and  $p=120$  GeV/c .*

| Beam momentum | pions ( $\pi^+$ ) | protons | Kaons ( $K^+$ ) |
|---------------|-------------------|---------|-----------------|
| 40 GeV/c      | 85%               | 12%     | 3%              |
| 120 GeV/c     | 61%               | 35%     | 4%              |

The beam scintillator Tr4 which is situated closest to the PIC was chosen for the calibration. It is installed 40 m upstream of the PIC and routinely used for aligning the beam. This scintillator has a diameter of 10 cm, a thickness of 2 mm and is partly surrounded by a light-guide. The beam scintillator gives a signal for each particle in the beam but saturates already at about  $1.5 \times 10^7$  particles per spill. First, the operating point of the scintillation counter had to be chosen by varying the high-voltage of the photomultiplier (PMT) and by recording the counts of the scintillator normalized to the primary particles hitting the T4 target. As it can be seen from Figure 9.8 a good operating voltage is between  $U=-2.15$  kV and  $-2.05$  kV. For the calibration measurements the high-voltage of the scintillator was set to  $U=-(2.10 \pm 0.05)$  kV.

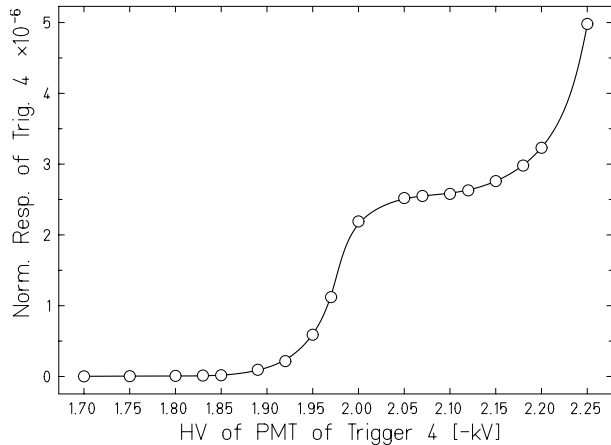


**Figure 9.8:** Counts of the beam scintillator Trigger4 normalized to the primary particles on the production target T4 as a function of high-voltage (HV) of the photomultiplier (PMT). A good operating point of the beam scintillator lies between  $U=-2.15\text{ kV}$  and  $-2.05\text{ kV}$ .

### 9.2.3.2 Measurements

In order to calculate the calibration factor  $\Gamma$  of the PIC, *i.e.* the relation between PIC counts and the number of particles in the beam, the number of counts of the PIC were compared with those of the beam scintillator.

The PIC counts were read out online with a LabView Programme running on a PC. The number of beam scintillator counts were received directly from the SPS beam-control programme. The counting time lasted the entire spill length of  $t=2.37\text{ s}$ . The beam intensity was changed by adjusting the aperture of collimators C3 and C5. The other collimators were set according to the CERF standard settings (see Table 9.1). For each C3 and C5 setting data of 3 spills were taken. The beam intensity range of 55 to 8000 PIC counts per SPS spill corresponds to about  $1.2 \times 10^6$  to  $1.8 \times 10^8$  beam particles per spill, assuming the old calibration factor of  $2.2 \times 10^4$  particles per PIC count.

Figure 9.9 shows the raw data obtained for the different collimator settings: the Tr4 counts per spill as a function of beam intensity, *i.e.* PIC counts per spill. At about 700 PIC counts per spill, which corresponds to approximately  $1.5 \times 10^7$  beam particles per spill, the response of the scintillator decreases already significantly due to its dead time losses. This is reflected in Figure 9.9 by the deviation of the points from linearity. Above about 2000 PIC counts per spill, which corresponds to about  $8.8 \times 10^7$  beam particles per spill, the response of the scintillator Tr4 breaks down completely. In this condition the anode current in the photomultiplier tube is so high that the potentials of the dynodes cannot be kept at their nominal values.

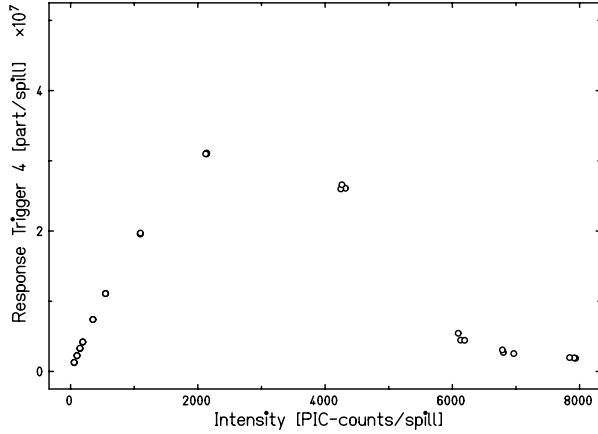


**Figure 9.9:** Trigger4 counts as a function of the beam intensity measured by the PIC. The counting time was the total spill length.

### 9.2.3.3 Analysis

Due to the high beam intensities during the measurements the correction for dead time losses of the scintillator Tr4 is the most important task. When calculating the effects of dead time the entire detector system must be taken into account. Usually each element of a detector system has its own dead time which can be either *extendable* (paralysable dead time model) or *non extendable* (non paralysable dead time model) [Leo87]. The difficulties which often arise are to determine which model is applicable for the entire detector system. Many detector systems are combinations of both, having some elements which are paralysable and others which are not.

Since no information about the detector components and their dead times was available the data analysis was done with both models. It was assumed that they are the two extremes of the experimental set-up, and the true set-up lies in between:

**non paralysable model (npm)**

$$f' = \frac{f}{1 + \tau f}$$

**paralysable model (pm)**

$$f' = f \cdot e^{-\tau f}$$

where  $f'$  is the measured count rate (in particles per second),  $f$  the true count rate (in particles per second) and  $\tau$  the dead time (in seconds) of the scintillator Tr4. Because the PIC does not saturate at these intensities the true count rate of Tr4 is proportional to the PIC count rate. The factor of proportionality is in fact the wanted calibration factor  $\Gamma$  of the PIC. This gives:

non paralysable model

$$f' = \frac{\Gamma \cdot PICcountrate}{1 + \tau\Gamma \cdot PICcountrate}$$

paralysable model

$$f' = \Gamma \cdot PICcountrate \cdot e^{-\tau\Gamma \cdot PICcountrate}$$

It was shown by [Gsc00b] that the PIC and Tr4 show a response even if the H6 beam is switched off. The PIC background is so small compared to the high PIC count rate, that it can be neglected. The Tr4 background ( $f'_{bg}$ ), however, has to be subtracted from the measured Tr4 count rates:

$$f' - f'_{bg} = \frac{\Gamma \cdot PICcountrate}{1 + \tau\Gamma \cdot PICcountrate} \Big|_{npm} \quad (9.7)$$

$$f' - f'_{bg} = \Gamma \cdot PICcountrate \cdot e^{-\tau\Gamma \cdot PICcountrate} \Big|_{pm}. \quad (9.8)$$

Therefore,

$$f' = \frac{\Gamma \cdot PICcountrate}{1 + \tau\Gamma \cdot PICcountrate} + f'_{bg} \Big|_{npm} \quad (9.9)$$

$$f' = \Gamma \cdot PICcountrate \cdot e^{-\tau\Gamma \cdot PICcountrate} + f'_{bg} \Big|_{pm}. \quad (9.10)$$

Two equations (9.9 and 9.10) are obtained which can be used as fit functions through the data points in order to get estimates of the PIC calibration factor  $\Gamma$ , the dead time  $\tau$  and the Tr4 background  $f'_{bg}$ . Figure 9.10 shows the fit to the data points with the function for the non paralysable model (left) and for the paralysable model (right).

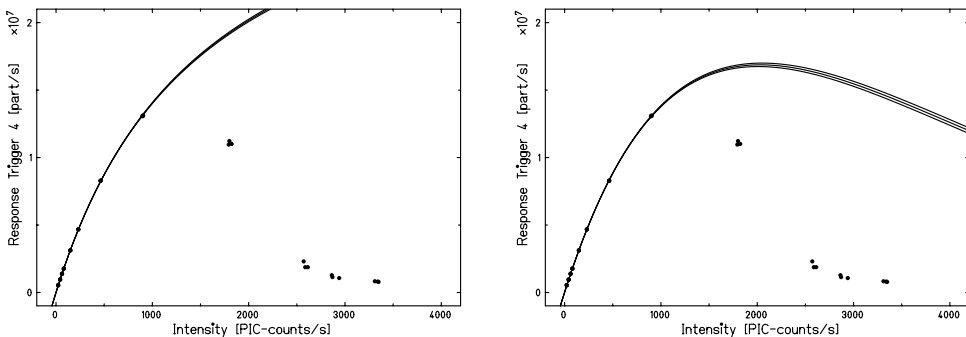


**Figure 9.10:** Measured count rate by Tr4 as a function of the true count rate by the PIC (symbols). **Left:** the solid line is a fit with Equation (9.9) according to the non paralysable model. **Right:** the solid line is a fit with Equation (9.10) according to the paralysable model. The experimental data are given per second.

Data points above 1700 PIC counts per second were excluded from the fit because in this region the limit of the photomultiplier electronics is reached and other effects than the Tr4 dead time are dominating. For the remaining 24 data points only a rounding error of 0.5 % of the Tr4 values was taken into account apart from the statistical uncertainties of the measurements. The results of the fits are summarized in Table 9.4.

**Table 9.4:** Fit results of the data using Equations 9.9 and 9.10 according to the non paralysable model and paralysable model.

| Fit parameter                  | Fit model       |                  |
|--------------------------------|-----------------|------------------|
|                                | non paralysable | paralysable      |
| $\Gamma$ [particles/PIC-count] | $23094 \pm 68$  | $22567 \pm 57$   |
| $\tau$ [ns]                    | $28.0 \pm 0.3$  | $21.8 \pm 0.2$   |
| $f'_{bg}$ [particles/s]        | $8437 \pm 2491$ | $21096 \pm 2299$ |
| $\chi^2/ndf$                   | 2.11            | 1.68             |

Taking the mean value of the calibration factors as obtained from the two fitting models, and assuming the half difference between the two values of  $\Gamma$  plus their errors to be equal to  $\pm 1 \sigma$  uncertainty, the final result becomes

$$\Gamma_{120}^{high} = (22831 \pm 279) \text{ particles/PIC-count.} \quad (9.11)$$

#### 9.2.3.4 Comparison with the low-intensity measurements

For  $p=120 \text{ GeV}/c$ :

For the low-intensity runs [Gsc00b]  $\Gamma$  was measured to be

$$\Gamma_{120}^{low} = (23696 \pm 178) \text{ particles/PIC-count.} \quad (9.12)$$

The high-intensity measurements of this work yield

$$\Gamma_{120}^{high} = (22831 \pm 279) \text{ particles/PIC-count.} \quad (9.13)$$

A final calibration factor  $\Gamma_{120}$  was derived by taking the mean value of these two independent measurements. Its error consists of two contributions: first the error

of the two results and second an additional systematic error of 4 % which comes from the uncertainty of the HV setting. This yields the final calibration factor

$$\Gamma_{120} = (23264 \pm 988) \text{ particles/PIC-count.} \quad (9.14)$$

### For $p=40 \text{ GeV}/c$ :

For completion, the  $p=40 \text{ GeV}/c$  measurements [Gsc00b] are

$$\Gamma_{40} = (24475 \pm 337) \text{ particles/PIC-count.} \quad (9.15)$$

### Comparing $\Gamma$ for $p=40 \text{ GeV}/c$ and $p=120 \text{ GeV}/c$ :

Increasing the energy changes the particle composition of the beam and also the energy loss of the single beam particles. Since the PIC is an ionization chamber, different calibration factors  $\Gamma$  are expected for the two different beam momenta  $p=40 \text{ GeV}/c$  and  $p=120 \text{ GeV}/c$ . Knowing the beam components and their energy losses for different beam energies it is expected that the energy loss in the PIC at  $p=40 \text{ GeV}/c$  is  $\approx 5 \%$  lower than at  $p=120 \text{ GeV}/c$ . This is in agreement with the measurements of  $\Gamma_{40}$  and  $\Gamma_{120}$ , see Equations 9.14 and 9.15.

## 9.3 Experimental set-up

After its calibration at PTB with monoenergetic neutrons the extended-range Bonner sphere spectrometer was extensively tested in the reference field of CERF (CERN-EU high-energy Reference Field). The CERF facility is installed along the H6 beam line  $\sim 405 \text{ m}$  downstream of the T4 production target. A secondary beam of positively charged hadrons and with momentum of  $p=120 \text{ GeV}/c$  is stopped in a copper target which has a diameter of 7 cm and a length of 50 cm. The intensity of the secondary beam is monitored by the PIC which is placed in the beam just upstream of the copper target. The target can be placed at two different positions inside an irradiation cave. The particles produced in the target traverse a shielding on top of these two positions at  $\sim 90^\circ$  with respect to the incoming beam direction. The shielding is made up of either 80 cm concrete or 40 cm iron (Figures 9.11 and 9.12).

These roof-shields produce almost uniform radiation fields over two areas of  $A=2 \times 2 \text{ m}^2$ , each of them divided into 16 squares of  $A=50 \times 50 \text{ cm}^2$ . Each square of these grids represents a reference exposure location. Additional measurement positions are available behind the lateral shielding of the irradiation cave, again at  $\sim 90^\circ$  with respect to the target as for the two roof positions. Shielding is either 80 cm or 160 cm thick concrete. At both positions 8 exposure locations (arranged

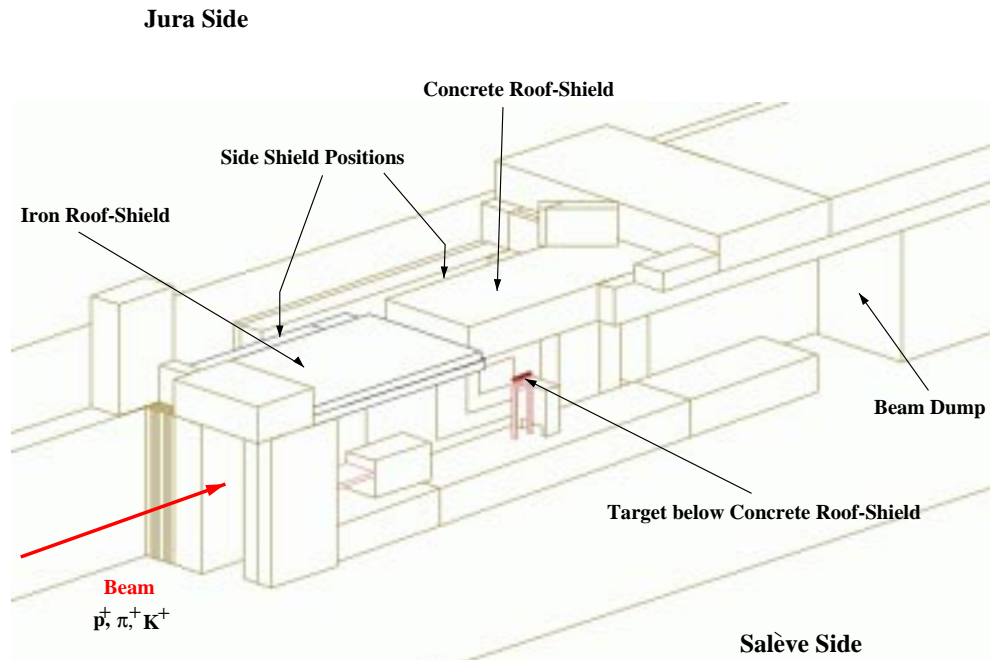


**Figure 9.11:** H6 area as simulated. The target can be placed either under the concrete roof-shield (80 cm thick) as currently shown, or under the iron roof-shield (40 cm thick). Reference positions are available on top of the roof-shields and behind two concrete side-shields, 80 cm and 160 cm thick, respectively.

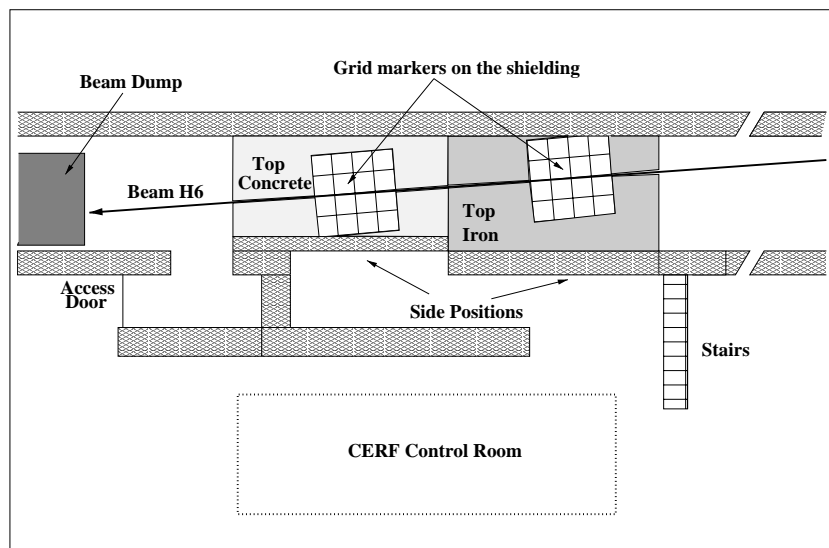


**Figure 9.12:** Plan view of the CERF facility. Not to scale.

in  $2 \times 4$  grids made up of the same  $A=50 \times 50 \text{ cm}^2$  squares) are provided. The nominal measurement locations (the reference field) are at the centre of each square at 25 cm above the floor, *i.e.* at the centre of a  $50 \times 50 \times 50 \text{ cm}^3$  air volume (Figure 9.13). There the energy distributions of the various particles (mainly neutrons,

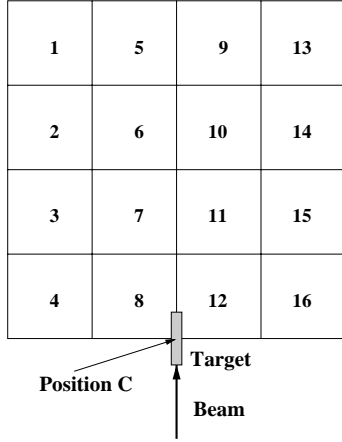


**Figure 9.13:** The reference grid with the 16 exposure positions used on the concrete roof-shield and iron roof-shield. Position C is an additional reference position which was used. It is located on the edge of the reference grid between position 8 and 12. The location of the copper target with respect to the grid is indicated as well.

but also photons, electrons, muons, pions and protons) have been obtained by Monte-Carlo simulations performed with the FLUKA code. Details of the latest simulations are given in [Bir98b]. The neutron and photon energy distributions calculated for a primary beam of positively charged particles with a momentum of  $p=120 \text{ GeV}/c$  (35 % protons, 61 % pions and 4 % kaons) are shown in Figure 9.14.

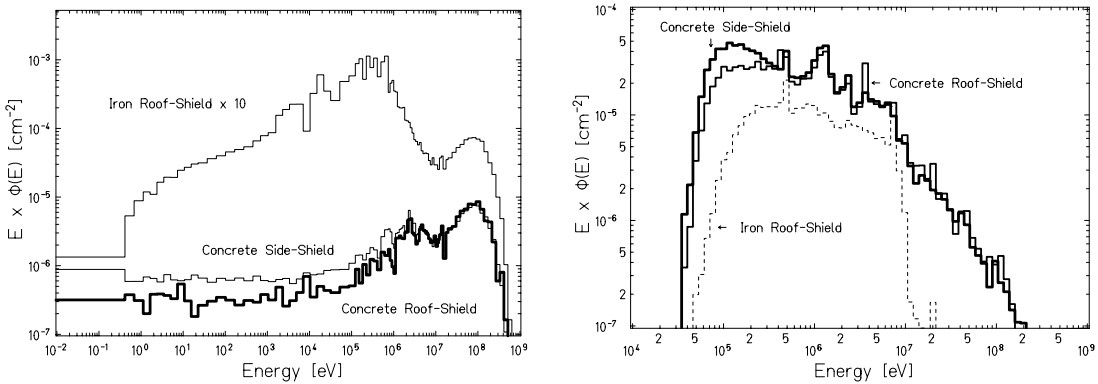


**Figure 9.14:** Neutron (left) and photon (right) spectral fluence calculated with FLUKA outside the concrete and iron shieldings (Figure 9.11) [Bir98b]. For clarity, the spectrum on the iron roof-shield is scaled by a factor 10.

The spectrum outside the iron shield is dominated by neutrons in the 0.1-1 MeV energy range. The energy distribution outside the concrete shield shows additionally a large relative contribution of 10-100 MeV neutrons. Therefore, these

exposure locations provide radiation fields of a wide energy spectrum well suited to test dosimetric instrumentation like Bonner spheres under different conditions. It also reproduces fairly closely the neutron field produced by cosmic rays at commercial flight altitudes [Alb99]. The neutron spectral fluence behind the side concrete shield of 80 cm thickness is similar to the one on the top concrete shield, but shows an increased low-energy tail due to backscattering of neutrons from the concrete wall nearby. The fluence rates of the other hadrons are much lower than that of neutrons.

As seen from Figure 9.14 the photon fluence is almost one order of magnitude lower than the neutron fluence on the iron roof-shield, but almost a factor two higher than the neutron fluence on the concrete roof-shield, because of the contribution of  $(n,\gamma)$  reactions. The electron fluence is about one order of magnitude less than that of neutrons and the muon fluence almost three orders of magnitude less. The accuracy of the calculated neutron spectral fluences was verified in the past by extensive measurements performed by several collaborating institutions and different instrumentation [Bir98b].

The measurements with the extended-range Bonner sphere spectrometer were performed at the nominal locations of positions 6 on concrete top (CT06), position C on concrete top (CTC) and position 6 on iron top (IT06) *i.e.* 25 cm above the centre of the corresponding grid element in order to compare properly the experimental results with the calculations.

## 9.4 Background measurements

When the magnets of the H6 beam line are switched off, the beam coming from the target T4 cannot reach the CERF area. However, the Bonner spheres and the PIC measure a certain amount of counts during the spill. This can be caused by other beam lines with a big halo that are close to the H6 beam, scattered neutrons or some particles from the T4 target that can still reach the counters. These particles, mostly muons, stream over the concrete and iron roof-shields. Their intensity depends on various factors which are not under control of the CERF user, such as the intensity of secondary beams in neighbouring beam lines. The contribution of background to the counter reading can be quantified by two measurement conditions: first by switching off the beam in the CERF area, and second by removing the copper target. Both lead to the similar results as is shown in Figure 9.15.

Since the first method was more feasible, before each measurement the background was recorded by switching off the beam in the area. Measurements with beam but without target were carried out only for some measurements for comparison. The background reading of the PIC averaged over all measurements

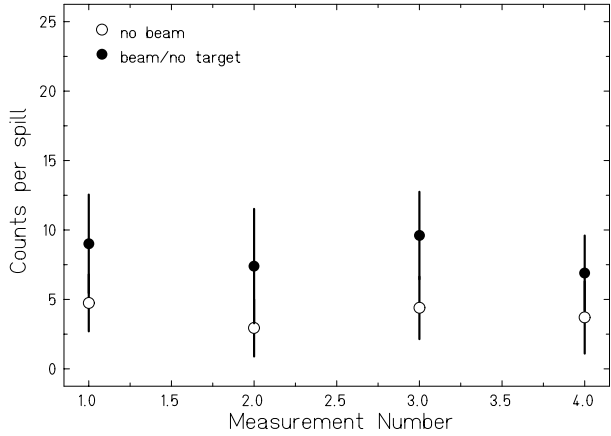


**Figure 9.15:** Reading due to background of the  $^{81}\text{Cd}$  sphere without beam (circles) and with beam but without copper target in the beam line (dots).

without beam gave  $0.61 \pm 0.04$  counts per spill. In order to investigate at which intensities the background corrections become less important measurements with different beam intensities were performed for Ollio. Figure 9.16 shows the counts

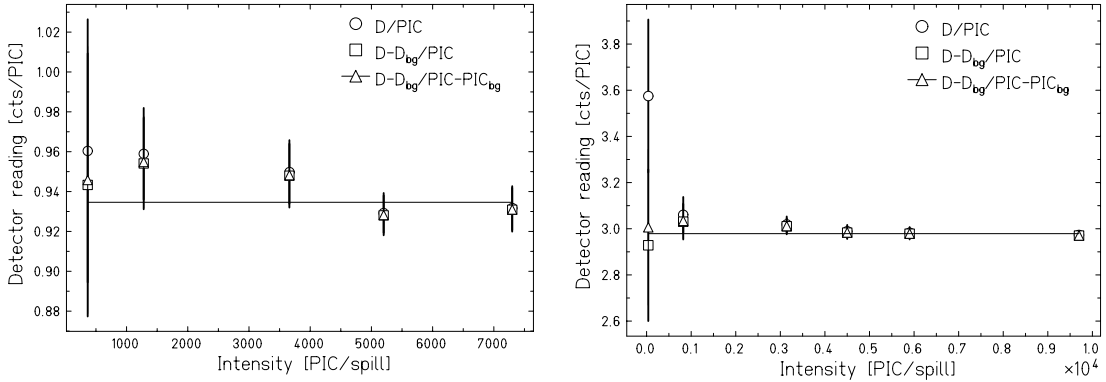


**Figure 9.16:** Reading of Ollio for different ways of background subtraction as a function of beam intensity at position CS02 (left) and IT06 (right).

per spill as a function of different PIC intensities per spill with and without background correction for measurements on the concrete side and iron roof-shields. The background correction was either applied only to the reading of the detector, or both to the detector and the PIC. The straight line is a fit through the data for which the background corrections were performed for both the detector and the PIC. Figure 9.16 shows that above  $\sim 1000$  PIC counts per spill the background of the PIC and of the Bonner sphere can be neglected.

The measurements with the Bonner spheres were performed at beam intensities between  $\sim 1000$  and  $\sim 3000$  PIC counts per spill. In order to verify that no dead

time effects of the electronics or pile up in the detector have occurred, studies of the detector performance as a function of beam intensities up to  $\sim 10000$  PIC counts per spill were performed. Figure 9.17 shows the count rate of Ollio at the concrete side and iron top positions as a function of beam intensity.

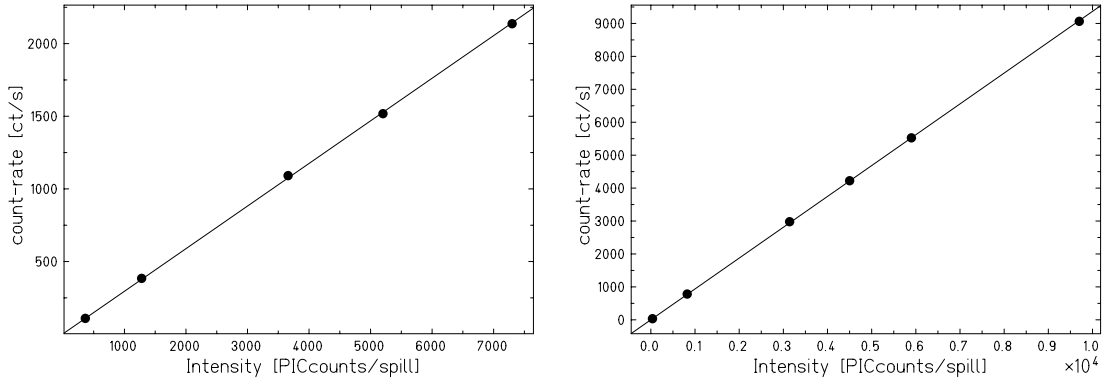


**Figure 9.17:** Background corrected count rate of Ollio as a function of beam intensity at position CS02 (left) and IT06 (right). The straight lines are fits through the data points.

As it can be seen from Figure 9.17 the detector shows a linear response up to a count rate of 9000 counts per second. The straight lines are fits through the experimental data with  $\chi^2/ndf = 0.6$  and  $\chi^2/ndf = 0.4$  for the measurements on the concrete side and iron top positions, respectively.

## 9.5 Data analysis and results

Measurements were performed during two beam-time periods: the first in May 2000 on the concrete roof-shield position C (CTC) using the NIM electronics and the second in July 2000 on the concrete roof-shield positions C (CTC) and 6 (CT06) and on the iron roof-shield position 6 (IT06), acquiring the data with the MAB device. Information about the electronics set-up and their characteristics can be found in 6.4.

During the May 2000 run three independent measurements over several spills were acquired and normalized to the incident beam particles by using the PIC calibration factor determined in Section 9.2.3. The intensity of the beam was varying between 1200 and 5000 PIC/spill. The count rate of the Bonner spheres was 150-1200 ct/s so that no dead time effects and pile-up in the detector occurred. For each sphere a mean value of the background  $\langle C_{m-bg} \rangle$  was recorded and subsequently subtracted from the raw detector reading  $\langle C_{m-r} \rangle$  in order to obtain the background corrected detector counts  $\langle C_m \rangle$ . Table 9.5 summarizes the experimental data obtained in the May run.

**Table 9.5:** Counts per incident beam particle ( $\langle C_m \rangle$ ) of the Bonner spheres exposed at position CTC during the May 2000 run. The quoted uncertainties derive from the standard deviation of the measurements and the uncertainty on the PIC calibration factor.

| Sphere  | $\langle C_m \rangle$            |
|---------|----------------------------------|
| 81Cd    | $(1.38 \pm 0.07) \times 10^{-5}$ |
| 81 mm   | $(2.01 \pm 0.09) \times 10^{-5}$ |
| 108 mm  | $(2.72 \pm 0.12) \times 10^{-5}$ |
| 133 mm  | $(3.19 \pm 0.15) \times 10^{-5}$ |
| 178 mm  | $(3.23 \pm 0.15) \times 10^{-5}$ |
| 233 mm  | $(2.81 \pm 0.13) \times 10^{-5}$ |
| Stanlio | $(1.58 \pm 0.07) \times 10^{-5}$ |
| Ollio   | $(1.93 \pm 0.09) \times 10^{-5}$ |

During the July 2000 run data were acquired with the MAB device spill by spill and during at least 20 spills. This gives better information on the fluctuation of the detector readings. As an example, Figure 9.18 shows the distribution of the count rate for Ollio. For this measurement data during 90 spills were recorded.

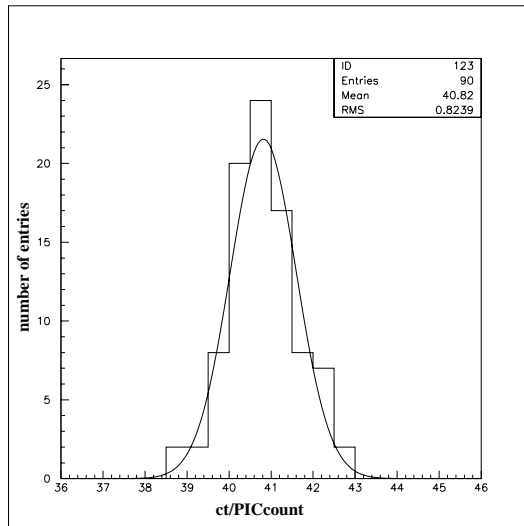


**Figure 9.18:** Distribution of the count rate for Ollio (histogram). Data were acquired during 90 spills. The solid line is a Gaussian fit.

It can be seen that the distribution is very well fitted by a Gaussian with a mean of 40.82 and a r.m.s. of 0.82, *i.e.* 2 %. It shows that the measurement set-up has systematic errors not larger than 2 %.

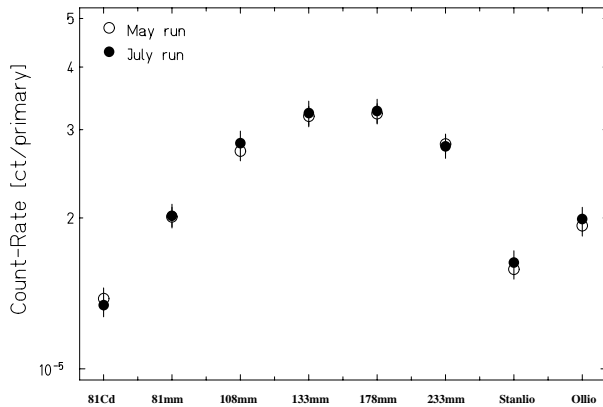
During a series of measurements the collimator settings were kept constant. The beam intensities were  $\sim 1500$  PIC counts per spill for the measurements on the concrete roof-shield and  $\sim 230$  PIC counts per spill at IT06. The count rates of the Bonner spheres thus obtained were 125-470 ct/s for the concrete positions, and 220-1570 ct/s for position IT06.

The readings of the Bonner spheres were normalized to the number of incident beam particles for each spill, and the average over all spills and its weighted uncertainty were calculated. Again, the detector reading due to the background  $\langle C_{m-bg} \rangle$  was subtracted from the raw reading  $\langle C_{m-r} \rangle$  in order to get the corrected one  $\langle C_m \rangle$ . Table 9.6 shows the experimental results ( $\langle C_m \rangle$ ) of the July run. During the analysis of the data obtained from Ollio on CT06 and from 81Cd and 81 mm on IT06 problems with the electronics became manifest and those results were therefore discarded.

**Table 9.6:** Counts normalized to incident beam particle ( $\langle C_m \rangle$ ) of the Bonner spheres exposed at positions CT06, CTC and IT06 during the July 2000 run. The quoted uncertainties derive from the standard deviation of the measurements and the uncertainty on the PIC calibration factor.

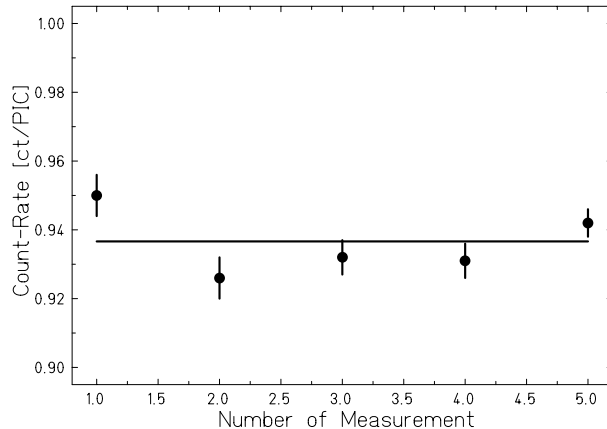
| Spheres | Measured counts per beam particle $\langle C_m \rangle$ |                                  |                                  |
|---------|---|----------------------------------|----------------------------------|
|         | CT06  | CTC                              | IT06                             |
| 81Cd    | $(1.75 \pm 0.09) \times 10^{-5}$                        | $(1.34 \pm 0.07) \times 10^{-5}$ |                                  |
| 81 mm   | $(2.45 \pm 0.14) \times 10^{-5}$                        | $(2.02 \pm 0.11) \times 10^{-5}$ |                                  |
| 108 mm  | $(3.46 \pm 0.19) \times 10^{-5}$                        | $(2.82 \pm 0.16) \times 10^{-5}$ | $(7.75 \pm 0.43) \times 10^{-4}$ |
| 133 mm  | $(4.03 \pm 0.22) \times 10^{-5}$                        | $(3.24 \pm 0.18) \times 10^{-5}$ | $(8.85 \pm 0.49) \times 10^{-4}$ |
| 178 mm  | $(4.11 \pm 0.23) \times 10^{-5}$                        | $(3.27 \pm 0.18) \times 10^{-5}$ | $(7.44 \pm 0.41) \times 10^{-4}$ |
| 233 mm  | $(3.50 \pm 0.19) \times 10^{-5}$                        | $(2.78 \pm 0.15) \times 10^{-5}$ | $(4.36 \pm 0.24) \times 10^{-4}$ |
| Stanlio | $(2.14 \pm 0.12) \times 10^{-5}$                        | $(1.63 \pm 0.09) \times 10^{-5}$ | $(3.76 \pm 0.21) \times 10^{-4}$ |
| Ollio   |   | $(1.99 \pm 0.11) \times 10^{-5}$ | $(1.30 \pm 0.07) \times 10^{-4}$ |

Figure 9.19 shows a comparison between the May and July measurements at position CTC. It can be seen that the two sets of data agree very well within their uncertainties and that they are fully reproducible. In order to investigate the stability of the experimental set-up during one run, measurements in the position



**Figure 9.19:** Counts per incident beam particle of the Bonner spheres measured at CTC during the May and July 2000 runs (see also Tables 9.5 and 9.6).

CT06 were repeated on consecutive days in July for the 133 mm sphere. Figure 9.20 shows the count rate of the sphere for the five repetitive measurements. The straight line is a fit and gives  $0.937 \pm 0.004$  ct/PIC count, which is an uncertainty of less than 1 %. This results also confirms the reproducibility of the experiment.



**Figure 9.20:** Counts per PIC count of the 133 mm sphere measured at CT06 during two consecutive days. The straight line indicates the mean of the measurements. The uncertainties of the single data points derive from the standard deviation of the measurements and the uncertainty on the PIC calibration factor.

Another indication of the stability of the measurements can be obtained from the representation of the conventional Bonner sphere readings as a function of sphere diameter. These are shown for all four measurements in Figure 9.21. The smoothness of the curves also indicates the good stability during the measurements. The readings of the 81Cd, Stanlio and Olio do not lie on the same curve,

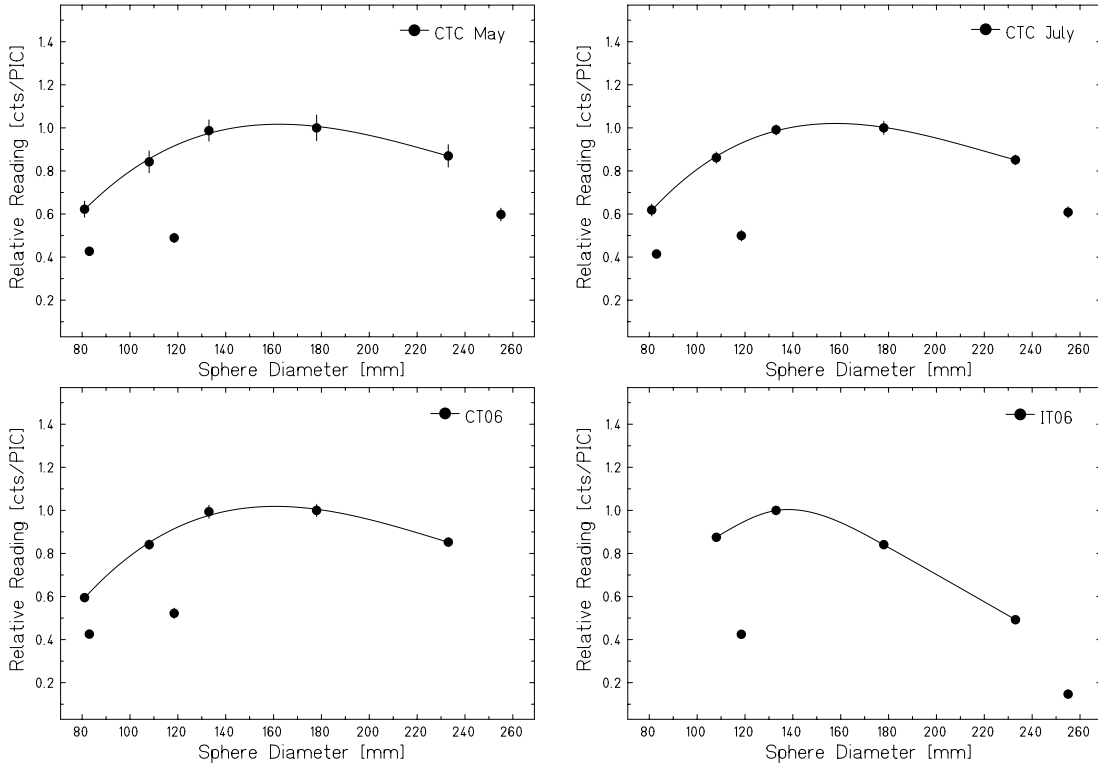


**Figure 9.21:** The relative readings of the Bonner spheres as a function of sphere diameter for the four measurements. The data of the conventional spheres lie on a smooth line. For comparison, the readings of the 81Cd sphere (83 mm diam.), Stanlio (118.5 mm diam.) and Ollio (255 mm diam.) are plotted as well.

of course, because of their additional content of cadmium and lead. The four curves generally differ in shape, but not so much for those obtained on the concrete shielding (CT06 and CTC). As large-diameter conventional spheres and Ollio show rather large readings, considerable contributions to the spectrum are expected in the high-energy region. Above the iron shield this contribution appears to be lower, in agreement with the computed spectral shapes shown in Figure 9.14.

Table 9.7 shows the calculated counts obtained by folding the Monte-Carlo fluence spectra at the exposure positions with the response functions of the Bonner spheres. As in Chapter 7 both the nominal and the modified response functions were considered.

**Table 9.7:** MC calculated counts per incident beam particle of the Bonner spheres at positions CT06, CTC and IT06. The indices  $c\text{-nom}$  and  $c\text{-mod}$  refer to the calculated nominal ( $C_{c\text{-nom}}$ ) and calculated modified ( $C_{c\text{-mod}}$ ) response functions. The quoted uncertainties are only statistical.

| Spheres | CT06               |                    | CTC                |                    | IT06               |                    |
|---------|--------------------|--------------------|--------------------|--------------------|--------------------|--------------------|
|         | $C_{c\text{-nom}}$ | $C_{c\text{-mod}}$ | $C_{c\text{-nom}}$ | $C_{c\text{-mod}}$ | $C_{c\text{-nom}}$ | $C_{c\text{-mod}}$ |
| 81Cd    | $2.01 \pm 0.04$    | $1.93 \pm 0.04$    | $1.56 \pm 0.04$    | $1.51 \pm 0.04$    | $49.1 \pm 0.3$     | $44.8 \pm 0.2$     |
| 81 mm   | $2.91 \pm 0.06$    | $2.92 \pm 0.05$    | $2.29 \pm 0.05$    | $2.30 \pm 0.05$    | $52.9 \pm 0.4$     | $45.1 \pm 0.2$     |
| 108 mm  | $3.69 \pm 0.06$    | $3.91 \pm 0.06$    | $2.88 \pm 0.06$    | $3.05 \pm 0.06$    | $85.6 \pm 0.6$     | $88.1 \pm 0.3$     |
| 133 mm  | $4.13 \pm 0.06$    | $4.48 \pm 0.07$    | $3.22 \pm 0.06$    | $3.50 \pm 0.06$    | $96.6 \pm 0.7$     | $105 \pm 0.4$      |
| 178 mm  | $4.27 \pm 0.07$    | $4.70 \pm 0.07$    | $3.34 \pm 0.06$    | $3.68 \pm 0.06$    | $79.1 \pm 0.6$     | $89.2 \pm 0.3$     |
| 233 mm  | $3.86 \pm 0.06$    | $4.01 \pm 0.08$    | $3.03 \pm 0.06$    | $3.16 \pm 0.07$    | $45.0 \pm 0.3$     | $51.2 \pm 0.2$     |
| Stanlio | $2.70 \pm 0.04$    | $2.25 \pm 0.04$    | $2.04 \pm 0.04$    | $1.72 \pm 0.03$    | $43.3 \pm 0.4$     | $36.2 \pm 0.2$     |
| Ollio   | $3.54 \pm 0.06$    | $3.49 \pm 0.06$    | $2.62 \pm 0.05$    | $2.61 \pm 0.05$    | $15.8 \pm 0.1$     | $15.9 \pm 0.1$     |

The comparison between the measured counts and the two sets of MC calculated counts for the four measurements is shown in Figure 9.22. The straight lines indicate the weighted mean of the two sets of data, which are plotted with their weighted errors. The difference between the weighted means regarding the nominal and modified set of data is less than 2 %. This is much lower than for the calibration measurements, where the difference was up to 20 %. This is understandable when considering that effects due to the variation of the moderator thickness or the polyethylene density are strongly energy dependent (on the one hand these effects increase the response to low-energy neutrons, and on the other hand they reduce it to intermediate and high-energy neutrons, see Section 6.2). In sum the effect of these variations is reduced in a broad neutron field as CERF.

As already mentioned in Section 6.2 the two sets of response functions represent the two extremes of the real situation. Thus one can define calculated mean counts  $C_c$  (Table 9.8) for each sphere at the three exposure positions by taking the average of  $C_{c\text{-nom}}$  and  $C_{c\text{-mod}}$ . Its uncertainty is obtained from the half difference between the minimum and maximum, the statistical uncertainties from the Monte-Carlo calculations and the uncertainties due to variation of the density and the diameter as described in Sections 6.2 and 7.3.

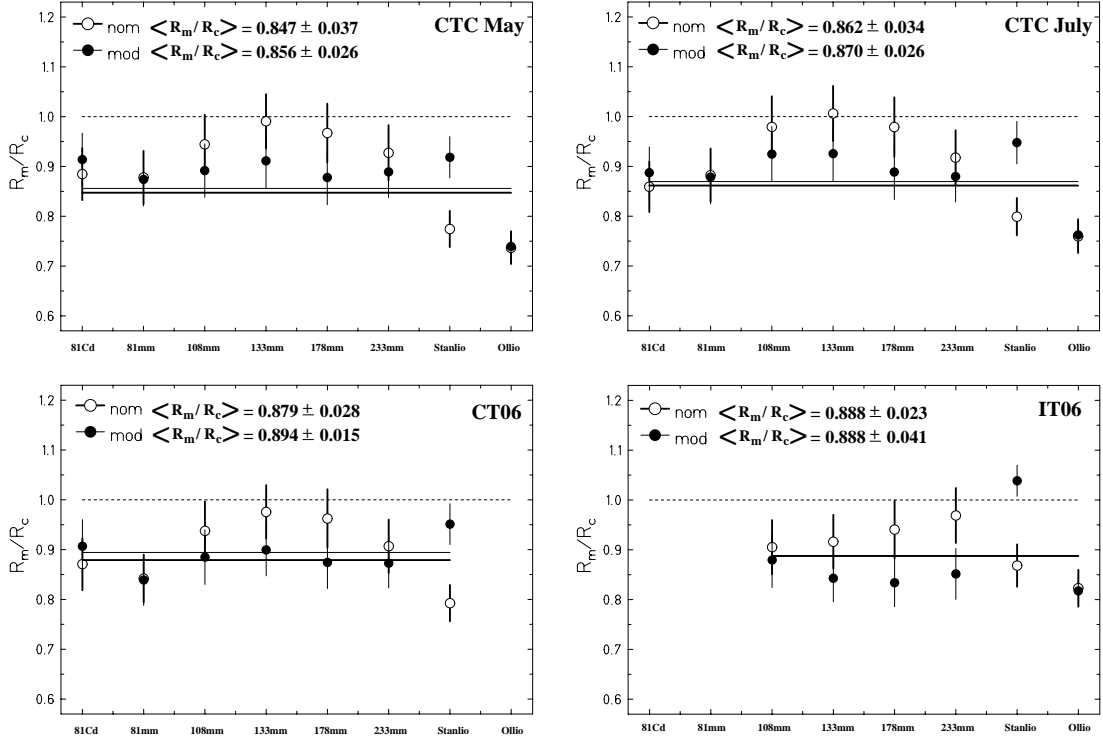


**Figure 9.22:** Ratio of the measured counts to the MC calculated ones derived from both the nominal and the modified response functions for the four different measurements, vs. Bonner sphere.

**Table 9.8:** MC calculated mean counts per incident beam particle ( $C_c$ ) of the Bonner spheres at positions CT06, CTC and IT06. The uncertainties were calculated according to Section 6.2.

| Spheres | Calculated mean counts per incident beam particle $C_c$ |                                  |                                 |
|---------|---|----------------------------------|---------------------------------|
|         | CT06  | CTC                              | IT06                            |
| 81Cd    | $(1.97 \pm 0.12) \times 10^{-5}$                        | $(1.54 \pm 0.10) \times 10^{-5}$ | $(47.0 \pm 3.2) \times 10^{-5}$ |
| 81 mm   | $(2.92 \pm 0.17) \times 10^{-5}$                        | $(2.29 \pm 0.14) \times 10^{-5}$ | $(49.0 \pm 4.7) \times 10^{-5}$ |
| 108 mm  | $(3.80 \pm 0.30) \times 10^{-5}$                        | $(2.96 \pm 0.24) \times 10^{-5}$ | $(86.9 \pm 6.3) \times 10^{-5}$ |
| 133 mm  | $(4.31 \pm 0.30) \times 10^{-5}$                        | $(3.36 \pm 0.24) \times 10^{-5}$ | $(101 \pm 6.7) \times 10^{-5}$  |
| 178 mm  | $(4.49 \pm 0.33) \times 10^{-5}$                        | $(3.50 \pm 0.26) \times 10^{-5}$ | $(84.2 \pm 6.7) \times 10^{-5}$ |
| 233 mm  | $(3.94 \pm 0.24) \times 10^{-5}$                        | $(3.09 \pm 0.19) \times 10^{-5}$ | $(48.1 \pm 4.0) \times 10^{-5}$ |
| Stanlio | $(2.48 \pm 0.26) \times 10^{-5}$                        | $(1.88 \pm 0.20) \times 10^{-5}$ | $(39.8 \pm 4.1) \times 10^{-5}$ |
| Olio    | $(3.52 \pm 0.20) \times 10^{-5}$                        | $(2.61 \pm 0.15) \times 10^{-5}$ | $(15.8 \pm 0.8) \times 10^{-5}$ |

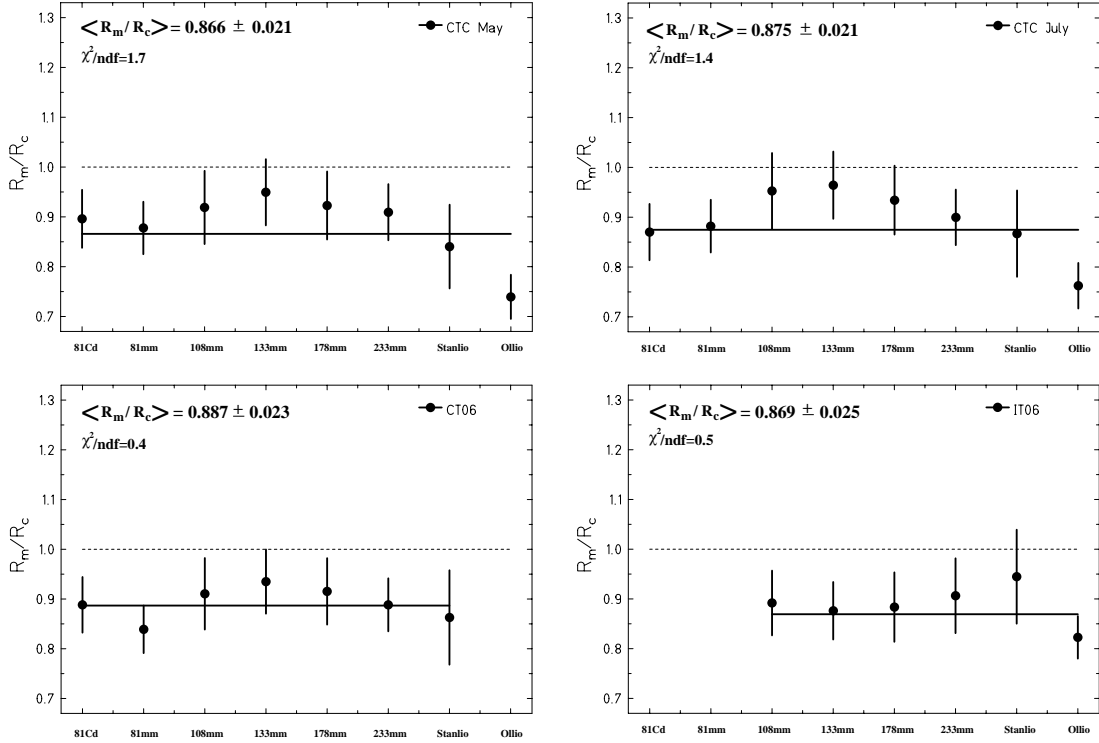


**Figure 9.23:** Ratio of the measured counts to the MC calculated mean ones for the four different measurements vs. Bonner sphere. The uncertainties of the single data points derive from the experimental uncertainties given in Table 9.5 and 9.6 and the calculated ones from Table 9.8.

The MC calculated mean counts can be compared with the experimental ones in the same way as done before. Figure 9.23 shows the ratio between the experimental and MC calculated mean counts for each exposure position vs. Bonner sphere. The uncertainties of the single data points derive from the experimental uncertainties given in Table 9.5 and 9.6 and the calculated ones from Table 9.8. The straight lines are fits through the data points. The fit parameters are plotted in the figure. They show that the fits describe the data very well. The weighted mean of each exposure position is in perfect agreement to the other. Averaged over all exposure positions this gives an overall factor,  $f_{CERF}$ , between experiment and calculation:

$$f_{CERF} = \frac{R_m}{R_c} = 0.874 \pm 0.011 \quad \text{with} \quad \chi^2/ndf = 0.2$$

with its weighted error of the mean value.  $f_{CERF}$  verifies the factor  $f=0.899 \pm 0.014$  (Equation 7.8) determined by the calibration measurements. It shows that the results of the Bonner spheres obtained from two completely different measurements

are consistent. Hence one can apply the calibration factor,  $f_c$ , to the experimental results in order to correctly compare the simulated and experimental counts (Figure 9.24). The results of the May and July measurements at CTC were combined in the Figure. It can be seen that the recalibrated results agree very well with the

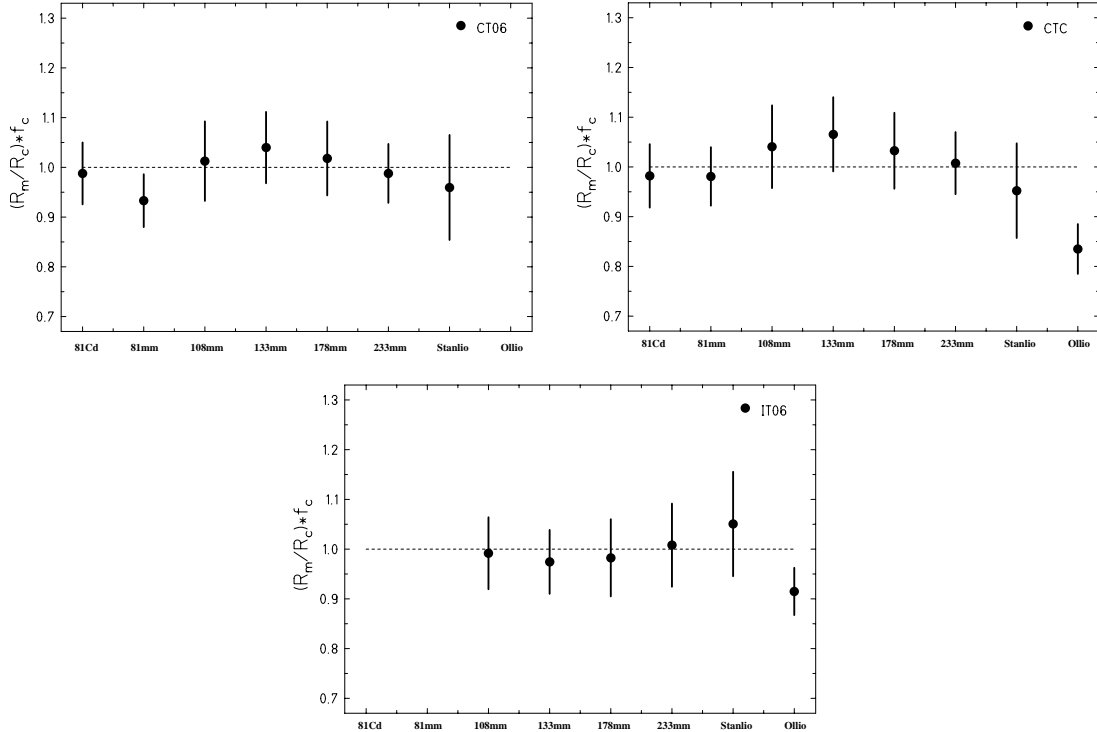


**Figure 9.24:** Ratio of the normalized measured counts using the calibration factor of Equation 7.9, to the calculated mean ones at the three exposure locations versus Bonner sphere. The uncertainties are the same as in Figure 9.23 plus the error on the calibration factor.

FLUKA simulations. Only Olio at CTC and IT06 shows a slight underestimate of the experimental to calculated results by 10-15%. It should be stressed that measurements in a broad neutron field like at CERF are very complex, and the sources of discrepancies between experimental and computed results are not easy to untangle. Considering the uncertainties of the sphere responses as pointed out in Section 6.2 and Chapter 7, these results are fully satisfactory.

For completion the experimental data at CTC were unfolded using the programmes GRAVEL II and MAXED (see Chapter 4). Figure 9.25 shows the spectral fluence obtained by GRAVEL II starting with a flat guess spectrum, including first only the polyethylene spheres and then using the entire extended-range BSS. It can be seen that the conventional spheres do not resolve well the high-energy component of the neutron spectrum, while the results with the extended-range

BSS show a pronounced peak around  $E=100$  MeV. The unfolding procedure was repeated using the FLUKA calculated spectrum as input. The results are shown in Figure 9.26 for GRAVEL II (left) and MAXED (right). The results are the same for both programmes and reproduce the conclusions obtained from Figure 9.24, *i.e.* that the experimental measurements and MC calculations are in very good agreement. Only Ollio which is most sensitive to high-energy neutrons, shows experimental data which are about  $\sim 20\%$  less than the calculations. This effect manifests also in the unfolded spectra where the high-energy peak at  $\sim 70$  MeV is lower than in the input spectrum. Nevertheless these results are satisfactory for radiation protection purposes.

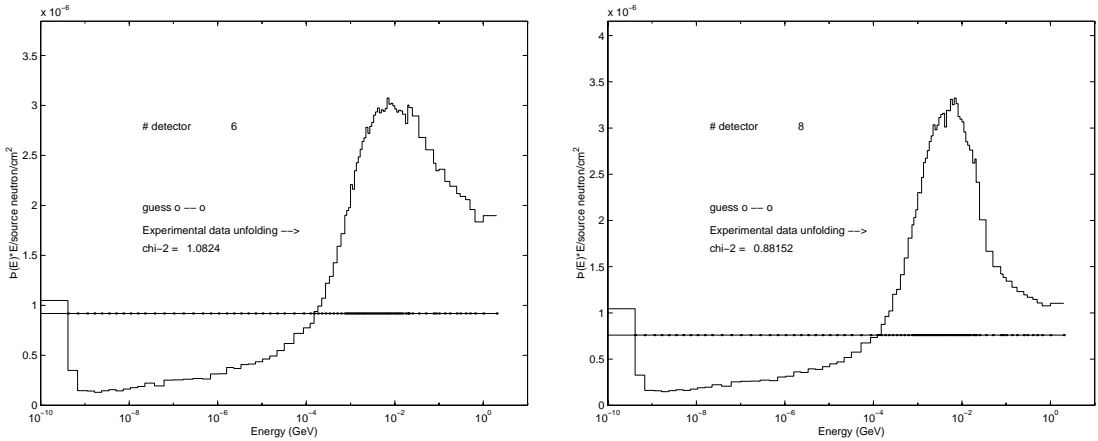


**Figure 9.25:** Neutron fluence per incident hadron on the copper target obtained by unfolding the experimental data with GRAVEL II, either including only the conventional Bonner spheres (left) or using the extended set (right) at the exposure position CTC of CERF. A flat guess was assumed.

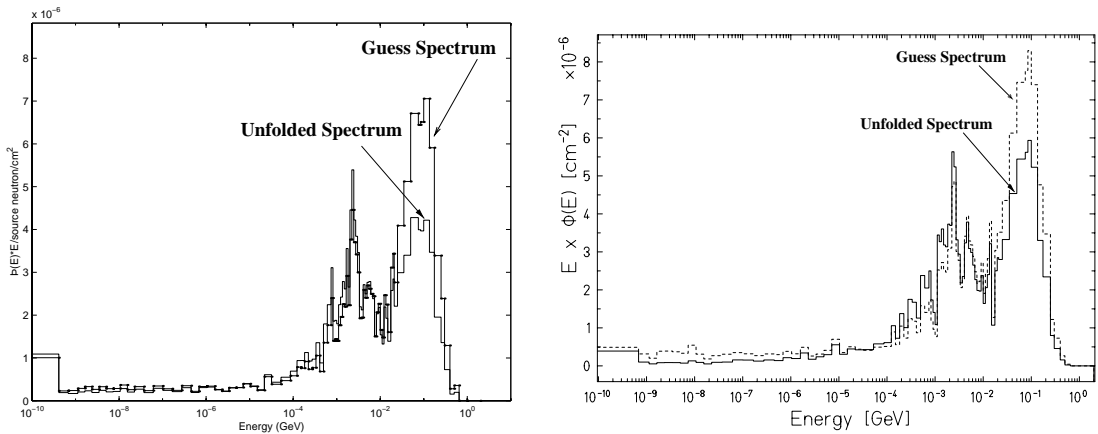


**Figure 9.26:** Neutron fluence per incident hadron on the copper target obtained by unfolding the experimental data from the extended set with GRAVEL II (left) and MAXED (right) at the exposure position CTC of CERF. As guess the spectrum calculated with FLUKA was assumed.

## 9.6 Upgrade of CERF

As shown in the previous section, the well characterized field of CERF can be used successfully for testing active and passive detectors in the context of high-energy particle accelerators. In addition the particle composition and spectral fluences provided at CERF are similar to those in the cosmic radiation field at commercial flight altitudes between 10 and 20 km (Figure 9.27). The International Commission on Radiological Protection (ICRP) has stated that exposures of aircraft personnel during flights at cruising altitudes (from 10000 m to 17000 m) have to be considered as occupational [ICR90]. In fact, a large fraction of the exposure of aircrew is due to neutrons with a comparable energy spectrum to that found around high-energy hadron accelerators. It becomes therefore of interest to test, to inter-compare and to calibrate instrumentation which is subsequently used for in-flight measurements on aircraft.

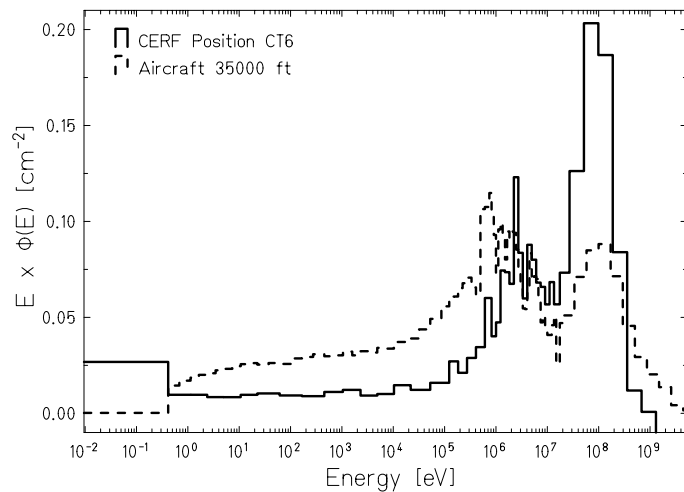


**Figure 9.27:** Comparison of the energy spectrum at commercial flight altitude to the one on the concrete roof-shield at CERF [Bar01].

Furthermore, for the evaluation of dosimeters used in space the calibration value as determined at CERF was taken for fast neutrons because this field is considered to be most similar to that in space. In a manned space station orbiting the earth neutrons constitute an important contribution to the personal dose equivalent. Most of the neutrons inside the station result from nuclear interactions of charged particles (mainly galactic protons and protons trapped by the earth's magnetic field) with the wall material of the vessel. A plot of  $E\Phi(E)$  against  $\log(E)$ , where  $\Phi(E)$  is the neutron fluence, shows peak intensities at about  $E=1$  MeV and 100 MeV, while for protons the peaks show up at about  $E=100$  MeV (trapped proton source) and in the GeV energy region (galactic proton source). Nevertheless, several other particles contribute to the dose in a space station or in a

shuttle orbiting the earth, or in a spacecraft travelling, for example, to Mars. Also, astronauts performing extravehicular activities are directly exposed to the cosmic ray field.

It was thus decided to study whether a different shielding configuration at CERF could produce a radiation field, rich in high-energy particles, more appropriate to the forthcoming measurements in the framework of the space programme. Preliminary Monte-Carlo simulations were performed with FLUKA in order to investigate this possibility. In order to avoid unnecessary waste of computing times, simulations were based on a simplified spherical geometry (Figure 9.28) rather than modelling the complete facility. The aim was to understand whether a given target/shielding combination and angular scoring region would indicate a promising situation which could subsequently be investigated more thorough. Eventually, the real facility will have to be properly modelled.

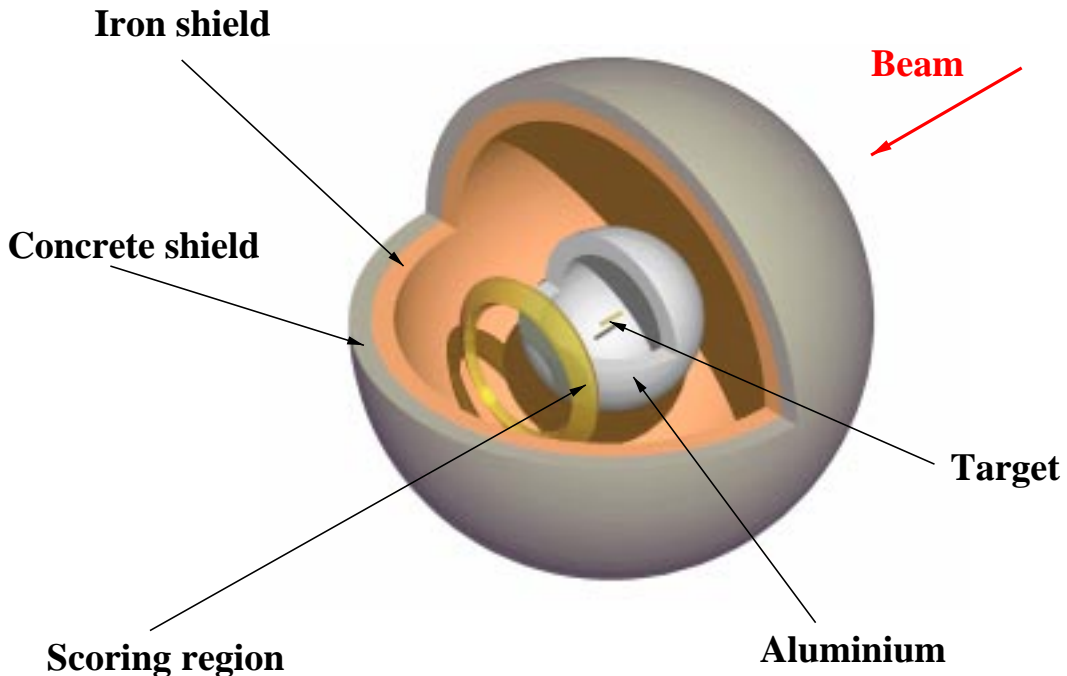


**Figure 9.28:** Simplified geometry for the first CERF upgrade studies.

The study aims at producing a radiation field rich in high-energy protons similar to that found in the stratosphere [Rei93] or high-energy neutrons and other secondary particles as found inside the space station or a spacecraft [Arm98]. The intention is also to increase the available dose equivalent rate at the exposure locations.

Calculations were performed first for the ‘standard’ 50 cm thick, 7 cm in diameter copper target as well as for two smaller targets: one 10 cm long and 7 cm in

diameter, the other 10 cm long and 1 cm in diameter. The target was at the centre of a spherical shield, with scoring done in conical regions  $10^\circ$  wide (from  $0^\circ$  to  $90^\circ$ ). The beam momentum was set to  $p=120$  GeV/c, and a 10 cm thick aluminium shield was placed at 1 m from the target. Neutrons, protons, pions, muons, photons and electrons were scored. Figure 9.29 shows a comparison between the spectral fluences in the  $10^\circ$ - $20^\circ$  angular region after the aluminium shield both for the ‘standard’ copper target and one 10 cm long and 7 cm in diameter. Since the spectral fluences do not differ much, only the ‘standard’ copper target was taken into account for further simulations.

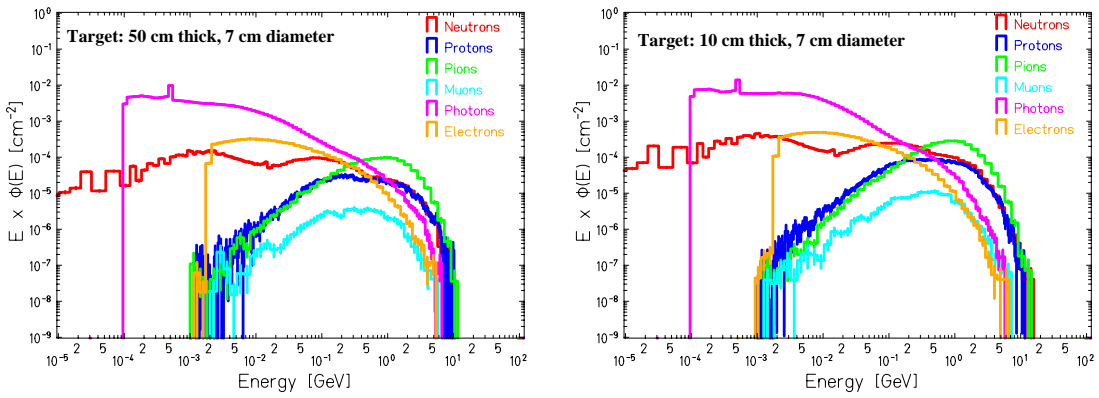


**Figure 9.29:** Particle spectral fluences in the  $10^\circ$ - $20^\circ$  angular region for a positive charged beam of  $p=120$  GeV/c (particles per primary beam particle incident on the target). The target is copper, **Left:** 50 cm thick and 7 cm in diameter and **Right:** 10 cm thick and 7 cm in diameter. A 10 cm aluminium shield is placed at 1 m from the target.

Since in a practical situation the dose equivalent rate produced by such a configuration will be much higher than that presently available at CERF, the new exposure area will have to be shielded. An additional layer of material acting as a back shield was therefore included in the simulations, made up of either 80 cm thick concrete or 40 cm iron backed by 40 cm concrete.

Figure 9.30 shows the spectral fluences for set-ups without back shielding, with a 80 cm concrete shield and with a shield made of 40 cm iron backed by 40 cm concrete. The simulation showed that the shielding is responsible for the low-energy neutron component shown in the figure, which can be reduced significantly by a combination of iron and concrete, in contrast to the pure concrete shield.

In the following all the simulations were carried out with the combined iron and concrete shield. With the standard copper target, a 10 cm thick Al shield and the latter back shield configuration, one should note that the high-energy component (above  $E=100$  MeV) of the proton spectrum in the forward direction (from  $0^\circ$  to  $10^\circ$ ) is similar to the energy spectrum of the galactic cosmic protons (Figure 9.31).

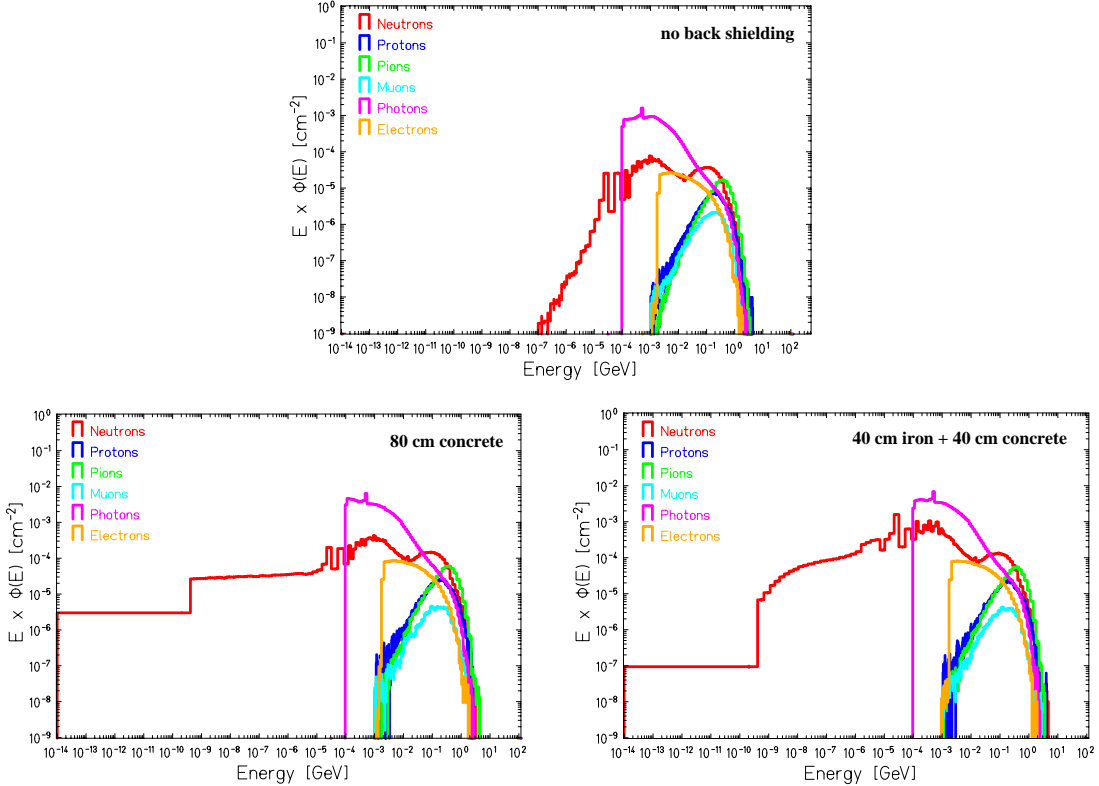


**Figure 9.30:** Particle spectral fluences in the  $40^\circ$ - $50^\circ$  angular region for a positive charged beam of  $p=120$  GeV/c (particles per primary beam particle incident on the target). The target is the ‘standard’ copper target. A 10 cm thick aluminium shield is placed at 1 m from the target; the external shielding is **Top:** none, **Left:** 80 cm thick concrete and **Right:** 40 cm iron backed by 40 cm concrete.

Also the neutron energy distribution extends up to about  $E=100$  GeV, *i.e.* much higher than the few hundreds of MeV at the present CERF configuration on the concrete roof-shield.

The neutron fluence is about  $6.5 \times 10^{-3} \text{ cm}^{-2}$  and  $4.3 \times 10^{-3} \text{ cm}^{-2}$  per primary particle on the copper target, in the forward (from  $0^\circ$  to  $10^\circ$ ) and transverse (from  $80^\circ$  to  $90^\circ$ ) directions, respectively, to be compared with the present figure of  $3.5 \times 10^{-5} \text{ cm}^{-2}$ . On the one hand this configuration has the advantage that an independent exposure area could in principle be built and run in parallel to the present set-up (*i.e.* simultaneously data taking on the concrete roof-shield or on the iron roof-shield). On the other hand, the pion component is too high in comparison to that present in space.

Therefore, another series of simulations were performed with increasing aluminium thickness, aiming at reducing the pion component relative to the other

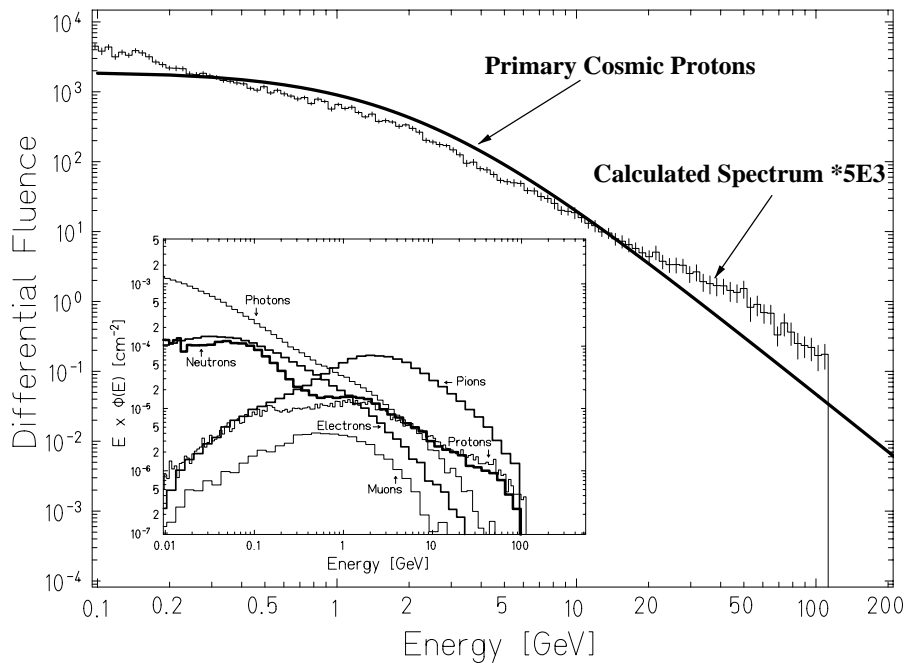


**Figure 9.31:** Particle spectral fluence in the  $0^\circ$  to  $10^\circ$  angular region for a positive charged beam of  $p=120$  GeV/c (particles per primary beam particle incident on the target). The target is the ‘standard’ copper target, the aluminium shield is 10 cm thick.

particles. Figure 9.32 shows the results for 10 cm, 40 cm and 80 cm thick aluminium shield at  $30^\circ$ - $40^\circ$  and  $60^\circ$ - $70^\circ$  emission angles. Note that with increasing aluminium thickness and emission angle the pion as well as the photon components decrease with respect to neutrons.

The influence of the primary beam momentum on the produced secondary particles was investigated in the range  $p=40$ - $400$  GeV/c. The simulations were performed with the actual particle composition of positive charged SPS beams. These are made up of  $\sim 85\%$  pions and  $\sim 15\%$  protons at  $p=40$  GeV/c,  $\sim 2/3$  pions and  $\sim 1/3$  protons at  $p=120$  GeV/c,  $\sim 1/3$  pions and  $\sim 2/3$  protons at  $p=205$  GeV/c and protons only at  $p=400$  GeV/c. It turned out that the spectral shape and the secondary particle composition do not change much with beam momentum (Figure 9.33), but the absolute neutron fluence per beam particle on the target increases: in the  $20^\circ$  to  $30^\circ$  angular region it is  $2.06 \times 10^{-3}$  cm $^{-2}$  for the beam of  $p=40$  GeV/c,  $5.23 \times 10^{-3}$  cm $^{-2}$  for the beam of  $p=120$  GeV/c,  $8.48 \times 10^{-3}$  cm $^{-2}$  for the beam of  $p=205$  GeV/c and  $1.53 \times 10^{-2}$  cm $^{-2}$  for the beam of  $p=400$  GeV/c.

Finally, the spectral fluences produced by a graphite instead of an aluminium shield were studied. Simulations were therefore performed with a 40 cm graphite shield and a beam of  $p=205$  GeV/c. Both, the pion and the photon compo-

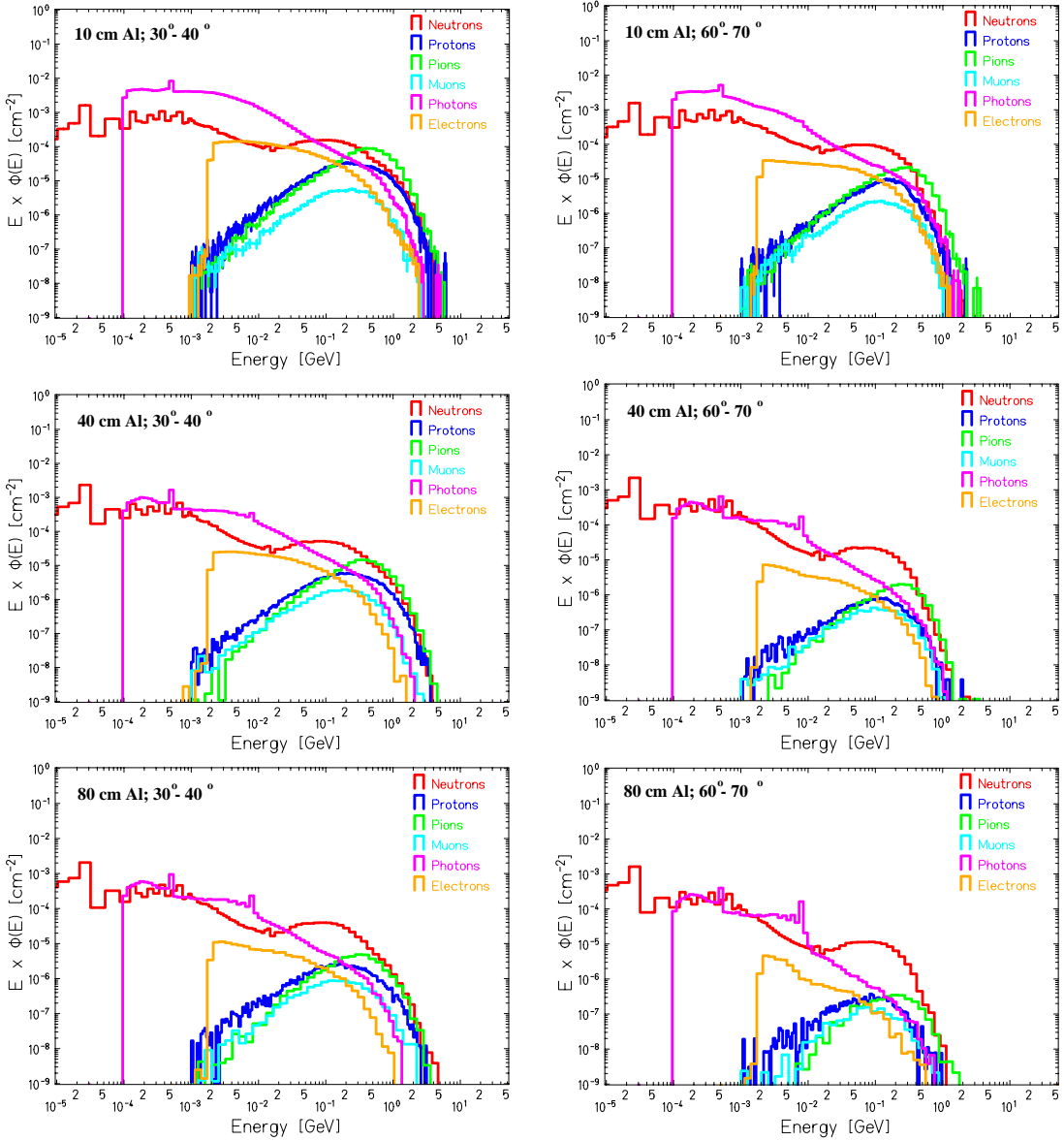


**Figure 9.32:** Particle spectral fluences. **Left:** in the  $30^\circ$  to  $40^\circ$  angular region, **Right:** in the  $60^\circ$  to  $70^\circ$  angular region, for a positive charged beam of  $p=120$  GeV/c (particles per primary beam particle incident on the target). The target is the ‘standard’ copper target. The aluminium shield is **Top:** 10 cm thick, **Middle:** 40 cm thick and **Bottom:** 80 cm thick.

ment slightly increase, so that this material brings no advantages with respect to aluminium (Figure 9.34).

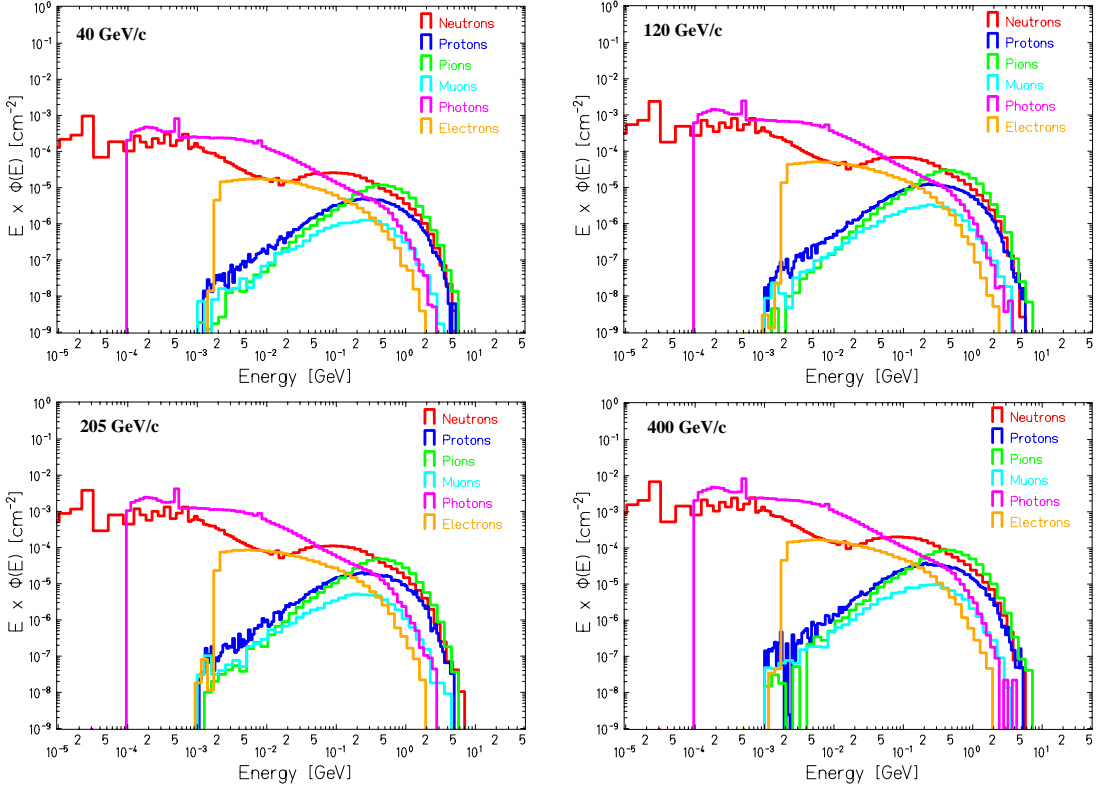


**Figure 9.33:** Particle spectral fluences in the  $20^\circ$ - $30^\circ$  angular region for a positive charged beam of different momenta (particles per primary particle incident on the target). The target is the ‘standard’ copper target, the aluminium shield is 40 cm thick.

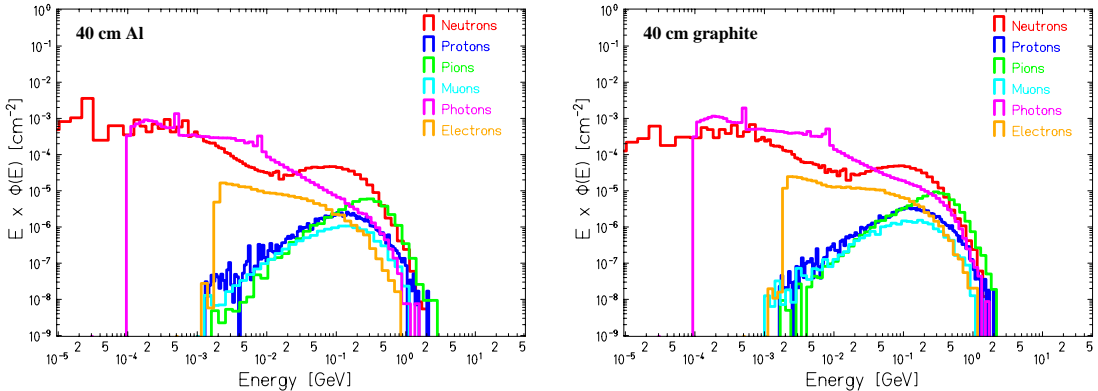


**Figure 9.34:** Particle spectral fluences in the  $50^\circ$ - $60^\circ$  angular region for a positive beam of  $p=205$  GeV/c (particles per primary beam particle incident on the target). The target is the ‘standard’ copper target, the shield is **Left** 40 cm of aluminium and **Right** 40 cm of graphite.

The study for the upgrade of CERF has shown several results: first, it is not necessary to change the ‘standard’ copper target or the present beam momentum of 120 GeV/c. Second, such a high-intensity exposure area needs an additional back shield; the combination of iron backed by concrete fits best in order to reduce the low-energy neutron component. Third, the relative spectral distribution of the particles can be varied significantly by increasing the aluminium thickness and the emission angle. A configuration having 40 cm thick aluminium shield and a scoring region in a forward direction seems to fulfil best the requirements in order to obtain high intensities, high energy particles and high neutron fluence.

# Chapter 10

## Summary and conclusions

The main aim of the work described in this thesis was to put into operation a new extended-range Bonner sphere spectrometer (BSS). The work performed can be grouped in the following topics:

### **The new extended-range Bonner sphere spectrometer**

- The response functions of 19 different detector configurations were studied by using FLUKA which is the state-of-the-art MC programme for shielding and dosimetry purposes in high-energy physics. Two of these configurations were considered to be a good complement of the conventional BSS and were thus built and tested. The first one, called *Ollio*, is a sphere consisting of a  $^3\text{He}$  proportional counter in the centre, surrounded by shells of 3 cm thick polyethylene, 1 mm cadmium, 1 cm lead and 7 cm polyethylene. The configuration of the second sphere, called *Stanlio*, is the  $^3\text{He}$  proportional counter in the centre, surrounded by shells of 2 cm thick polyethylene, 1 mm cadmium and 2 cm lead.
- Uncertainty estimations of the calculated response functions were carried out taking into account deviations in the sphere configuration, the polyethylene density and the sphere diameter from nominal values. It was shown that, especially for the small spheres, additional air-gaps of unknown dimensions between the moderator layers can cause response variations of up to 30 % depending on the energy.
- MC simulations have also shown that the old sphere supports made of plastics increase the neutron scattering and may therefore influence the count rate of the Bonner spheres. Thus, new sphere supports made of aluminium were designed and constructed for each sphere in such a way that the centre of each sphere is located at the same height. This is very convenient for a number of experimental situations.

## Detectors and electronics

- In order to compare the performance of three  ${}^3\text{He}$  proportional counters used in the experiments (*2 atm-detector*, *4 atm-detector* and *B-detector*) their intercalibration factors were determined experimentally. They are: ‘2’/‘4’=0.739±0.007, ‘2’/‘B’=0.984±0.011 and ‘B’/‘4’=0.751±0.011.
- One requirement of the system was to keep it portable and easy to operate. For this purpose a compact electronics of size  $20 \times 7 \times 5 \text{ cm}^3$ , containing an amplifier, a multi and single channel analyzer, a counter and a power supply, was chosen which can be easily operated via a portable PC. Tests of the  ${}^3\text{He}$  proportional counter and the electronics were performed in order to investigate the detector characteristics and the electronic noise of the complete system. Thresholds for the three detectors were determined which allow a good discrimination between neutron signals and gamma ray and noise signals.

## Calibration and experiment

- The calibration of the extended-range Bonner sphere set at the PTB with neutron beams of  $E= 144 \text{ keV}$ ,  $1.2 \text{ MeV}$ ,  $5 \text{ MeV}$  and  $14.8 \text{ MeV}$  resulted in a calibration factor  $f_c = \frac{R_c}{R_m} = 1.112 \pm 0.017$  with  $R_c$  the calculated response and  $R_m$  the measured one.
- The new Bonner sphere set was also tested with an  ${}^{241}\text{Am-Be}$  source in the CERN calibration laboratory and in a high-energy neutron field at CERF. The calculations agree better than 20 % with the measured values.

## Outlook

The extended-range Bonner sphere spectrometer was already successfully used in radiation protection for routine measurements in high-energy neutron fields, such as around present accelerators and experiments, but also for research work related to radiation protection [Ago01]. Thereby the superior performance of the new extended-range BSS compared to the conventional one became clearly visible. For the future the extended BSS will become essential to verify the correct operation of the dose monitors installed around the Large Hadron Collider LHC, where a large amount of high-energy neutrons will be present.

In addition to the work on the Bonner sphere spectrometer, the following studies on CERF were also carried out within this thesis:

## CERF beam monitor PIC

- Performance tests of the CERF beam monitor with radioactive gamma sources showed that the monitor needs about 2 hours to stabilize, it shows no electronic noise, its response is linear up to air kerma rates  $\dot{K}_a = 30 \text{ mGy/h}$  which was the limit of the gamma source, and it shows no leakage currents. Its operating voltage of  $U = 250 \text{ V}$  lies in the region of ion saturation for H6 beam intensities of up to  $5 \times 10^8$  particles per spill.
- Calibration measurements of the PIC yield for a positive charged hadron beam of  $p=120 \text{ GeV/c}$  a calibration factor  $\Gamma_{120} = (23264 \pm 988)$  particles/PIC-count and for  $p=40 \text{ GeV/c}$  a factor of  $\Gamma_{40} = (24475 \pm 337)$  particles/PIC-count.

## Upgrade of CERF

- First MC studies regarding an upgrade of CERF were performed in order to evaluate whether a different target and/or shielding configuration at CERF could produce a radiation field, rich in high-energy particles, more appropriate to the forthcoming measurements in the framework of the space programme. Such a new reference field would also allow to test and to calibrate the Bonner spheres at energies even higher than what was possible in this thesis. The results showed that it is not necessary to change the ‘standard’ copper target or the present beam momentum of  $p=120 \text{ GeV/c}$ , but only replace the 80 cm thick concrete shield by an aluminium shield. Furthermore, a back shielding is needed for the new high-intensity area, for which a combination of iron and concrete suits best in order to reduce the number of scattered neutrons. A configuration having 40 cm aluminium and an exposure region in the forward direction seems to fulfil best the requirements in order to obtain high intensities, high energy particles and a relative high neutron fluence.

# Appendix A

## Quantities used in radiological protection for external radiation

### A.1 Introduction

Two types of quantities are specially defined for the use in radiological protection: protection quantities, which are defined by the ICRP, and operational quantities, which are defined by the ICRU.

The most recent set of protection quantities recommended by the [ICR90] includes the effective dose,  $E$ , and the tissue or organ equivalent doses,  $H_T$ . These quantities are not directly measurable but are accessible to calculation if the conditions of irradiation are known.

The ICRU has defined a set of operational quantities for area and individual monitoring. They are designed to provide an estimate of the protection quantities and to serve as calibration quantities for dosimeters used in monitoring. For area monitoring, the appropriate operational quantities are the ambient dose equivalent,  $H^*(d)$ , and the directional dose equivalent,  $H'(d, \Omega)$ . For individual monitoring, the personal dose equivalent,  $H_p(d)$ , is the appropriate quantity.

The evolution of these protection and operational quantities has led to a system of correlated quantities, which is illustrated in Figure A.1. Both, the protection quantities and operational quantities can be related to the basic physical quantities fluence,  $\Phi$ , air kerma free-in-air,  $K_a$ , and the tissue absorbed dose,  $D$ .

Conversion coefficients, which relate operational and protection quantities to physical quantities, are calculated using radiation transport codes and appropriate mathematical models.

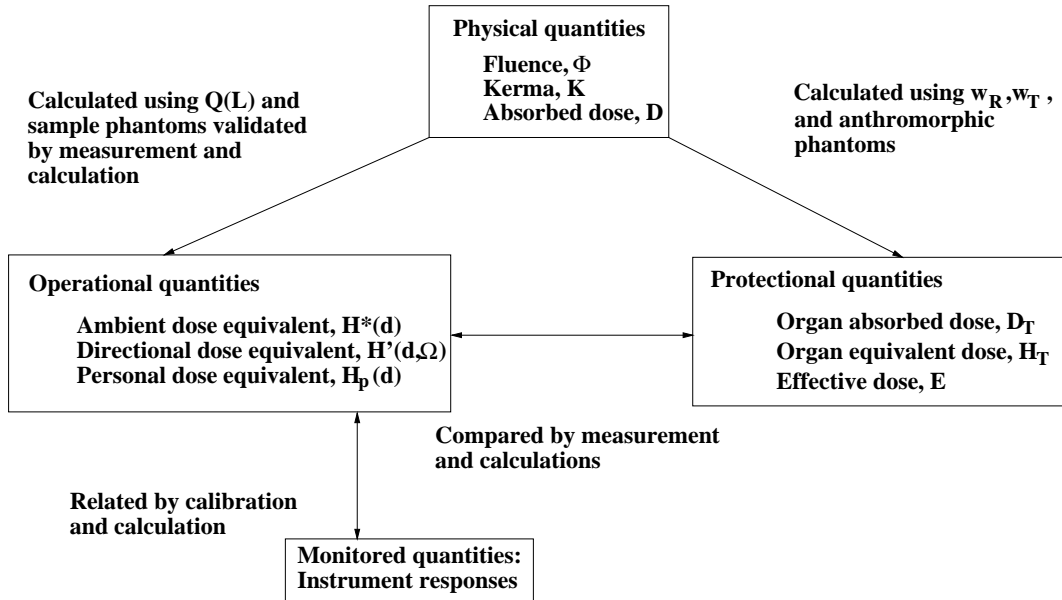


**Figure A.1:** Relationship of quantities for radiological protection monitoring purposes [ICR95].

## A.2 Physical quantities

### Fluence, $\Phi$ ,

is the quotient of  $dN$  by  $da$ , where  $dN$  is the number of particles incident on a sphere of cross-sectional area  $da$ , thus:

$$\Phi = \frac{dN}{da}. \quad (\text{A.1})$$

The unit of the fluence is  $[\text{cm}^{-2}]$ .

### Kerma, $K$ ,

is given by the quotient of  $dE_{tr}$  by  $dm$ , where  $dE_{tr}$  is the sum of the initial kinetic energies of all the charged ionizing particles liberated by uncharged ionizing particles in a volume element of mass  $dm$ , thus:

$$K = \frac{dE_{tr}}{dm}. \quad (\text{A.2})$$

The unit of kerma is  $[\text{J kg}^{-1}]$  and its special name is gray [Gy].

### Absorbed Dose, $D$ ,

is the quotient of  $d\bar{\varepsilon}$  by  $dm$ , where  $d\bar{\varepsilon}$  is the mean energy imparted by ionizing radiation to matter  $dm$ , thus

$$D = \frac{d\bar{\varepsilon}}{dm}. \quad (\text{A.3})$$

The unit of absorbed dose is  $[\text{J kg}^{-1}]$  and its special name is gray [Gy].

## A.3 Protectional quantities

### Organ Dose, $D_T$ ,

is the mean absorbed dose,  $D_T$ , in a specified tissue or organ of the human body,  $T$ , given by

$$D_T = (1/m_T) \int_{m_T} D dm \quad (\text{A.4})$$

where  $m_T$  is the mass of the tissue or organ and  $D$  is the absorbed dose in the mass element,  $dm$ . The unit of organ dose is  $[\text{J kg}^{-1}]$  and its special name is gray  $[\text{Gy}]$ .

### Equivalent Dose, $H_T$ ,

is the absorbed dose in an organ or tissue multiplied by the relevant radiation weighting factor. When the radiation field is composed of radiation with different values of  $w_R$ , the absorbed dose is subdivided into blocks, each multiplied by its own value of  $w_R$  and summed to determine the total equivalent dose, *i.e.*

$$H_T = \sum_R w_R \cdot D_{T,R}. \quad (\text{A.5})$$

The unit of equivalent dose is  $[\text{J kg}^{-1}]$  and its special name is sievert  $[\text{Sv}]$ .

### Effective Dose, $E$ ,

is a summation of the equivalent doses in tissues or organs, each multiplied by the appropriate tissue weighting factors. It is given by the expression

$$E = \sum_T w_T \cdot H_T = \sum_T w_T \cdot \sum_R w_R \cdot D_{T,R} \quad (\text{A.6})$$

where  $H_T$  is the equivalent dose in tissue or organ,  $T$ , and  $w_T$  is the tissue weighting factor for tissue,  $T$ . The unit of effective dose is  $[\text{J kg}^{-1}]$  and its special name is sievert  $[\text{Sv}]$ .

## A.4 Operational quantities

### Dose Equivalent, $H$ ,

at a point is given by

$$H = \int_L Q(L) \cdot \frac{dD}{dL} dL$$

where  $Q(L)$  is the quality factor for particles with linear energy transfer,  $L$ , and  $\frac{dD}{dL} \cdot dL$  is the absorbed dose between linear energy transfer,  $L$ , and  $L+dL$  at the point.

### A.4.1 Area monitoring

**Ambient Dose Equivalent,  $H^*(10)$ ,**

at a point of interest in a real radiation field, is the dose equivalent that would be produced by the corresponding expanded<sup>1</sup> and aligned<sup>2</sup> radiation field, in the ICRU sphere<sup>3</sup> at a depth of 10 mm, on the radius vector opposing the direction of the aligned field. The unit of ambient dose equivalent is  $[J \text{ kg}^{-1}]$  and its special name is sievert [Sv].

#### A.4.1.1 Individual monitoring

**Personal Dose Equivalent,  $H_p(10)$ ,**

is defined as the dose equivalent in ICRU soft tissue at a depth of 10 mm in the body at the location where the personal dosimeter is worn. The unit of personal dose equivalent is  $[J \text{ kg}^{-1}]$  and its special name is sievert [Sv].

## A.5 Correlated quantities

**Radiation Weighting Factor,  $w_R$ ,**

by which the tissue or organ absorbed dose is multiplied to reflect the higher RBE values for neutrons and alpha particles compared to low LET radiations. For neutrons  $w_R$  varies with the neutron energy,  $E_n$  (see Table A.1).

**Table A.1:** Radiation weighting factors  $w_R$  for neutron radiation according to ICRP 60.

| Energy                                   | $w_R$ |
|--|-------|
| $E_n < 10 \text{ keV}$                   | 5     |
| $10 \text{ keV} < E_n < 100 \text{ keV}$ | 10    |
| $100 \text{ keV} < E_n < 2 \text{ MeV}$  | 20    |
| $2 \text{ MeV} < E_n < 20 \text{ MeV}$   | 10    |
| $E_n > 20 \text{ MeV}$                   | 5     |

<sup>1</sup>In the expanded radiation field the spectral fluence and the angular fluence have the same values at all points of a sufficiently large volume as in the actual field at the point of interest.

<sup>2</sup>In the aligned and expanded radiation field all beams are thought to be aligned in the expanded field, so that they are opposed to the radius vector  $\vec{\Omega}$  specified for the ICRU sphere.

<sup>3</sup>The ICRU sphere is a phantom sphere made of tissue equivalent material 30 cm in diameter

**Tissue Weighting Factor,  $w_T$ ,**

by which the equivalent dose to a tissue or organ is multiplied in order to account for the relative stochastic detriment resulting from the exposure of different tissues and organs.

**Conversion coefficients**

link the protection and operational quantities to physical quantities characterizing the radiation field. Relating to this thesis only the neutron fluence to ambient dose equivalent conversion coefficients are shown (Figure A.2) in order to demonstrate the importance of high-energy neutrons.

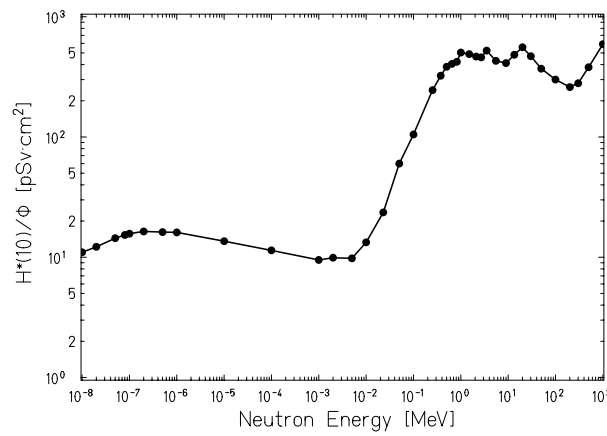


**Figure A.2:** Fluence to ambient-dose-equivalent conversion coefficient.

## Appendix B

### Cross sectional views of the detector configurations

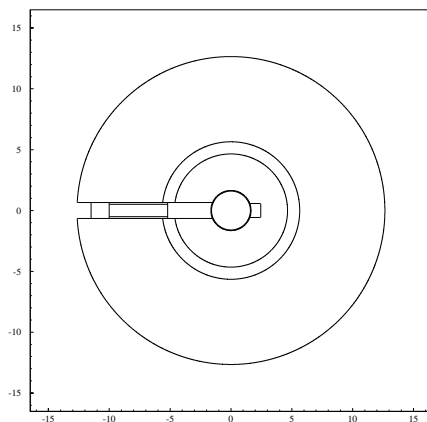


**Figure 1:** From the  ${}^3\text{He}$  proportional counter (3.3 cm in diameter) outwards: 3 cm polyethylene (PE), 1 cm lead, iron or copper, 7 cm PE.

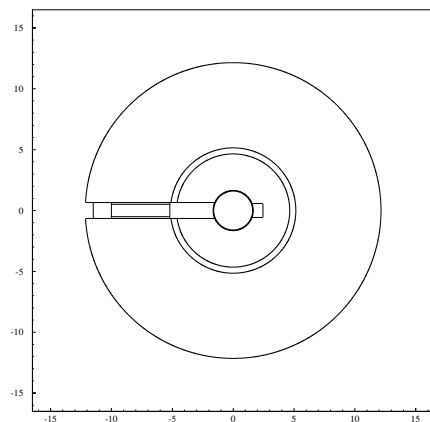


**Figure 2:** From the  ${}^3\text{He}$  proportional counter (3.3 cm in diameter) outwards: 3 cm polyethylene (PE), 5 mm iron, 7 cm PE.

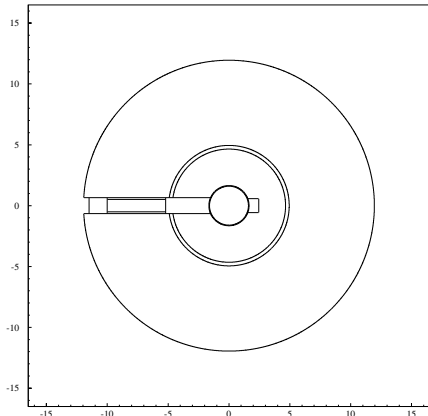


**Figure 3:** From the  ${}^3\text{He}$  proportional counter (3.3 cm in diameter) outwards: 3 cm polyethylene (PE), 3 mm lead, 7 cm PE.

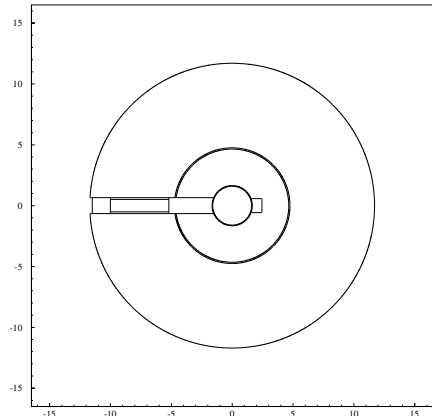


**Figure 4:** From the  ${}^3\text{He}$  proportional counter (3.3 cm in diameter) outwards: 3 cm polyethylene (PE), 1 mm cadmium, 7 cm PE.

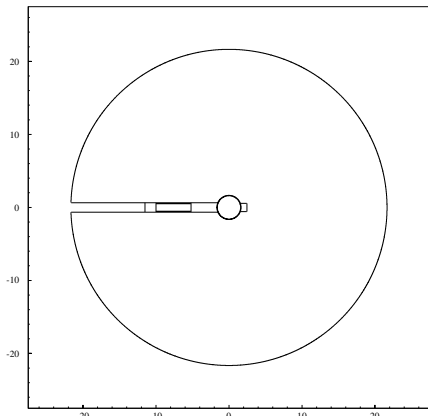


**Figure 5:** From the  ${}^3\text{He}$  proportional counter (3.3 cm in diameter) outwards: 20 cm polyethylene.

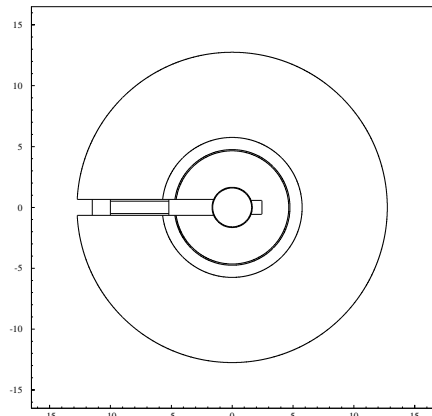


**Figure 6:** From the  ${}^3\text{He}$  proportional counter (3.3 cm in diameter) outwards: 3 cm polyethylene (PE), 1 mm cadmium, 1 cm lead, 7 cm PE ("Ollio" design).

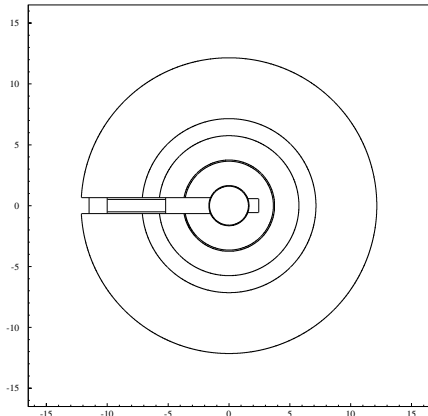


**Figure 7:** From the  ${}^3\text{He}$  proportional counter (3.3 cm in diameter) outwards: 2 cm polyethylene (PE), 1 mm cadmium, 2 cm PE, 1.4 cm lead, 5 cm PE.

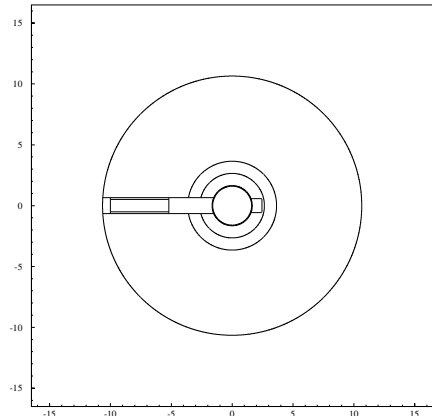


**Figure 8:** From the  ${}^3\text{He}$  proportional counter (3.3 cm in diameter) outwards: 1 cm polyethylene (PE), 1 cm lead, 7 cm PE.

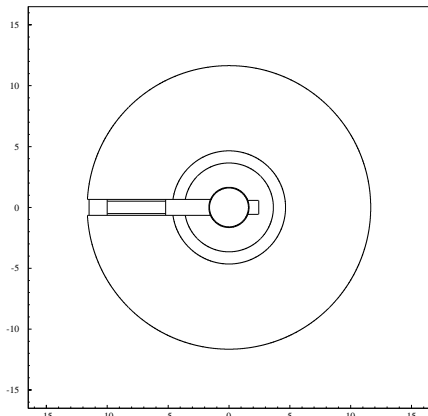


**Figure 9:** From the  ${}^3\text{He}$  proportional counter (3.3 cm in diameter) outwards: 2 cm polyethylene (PE), 1 cm lead, 7 cm PE.

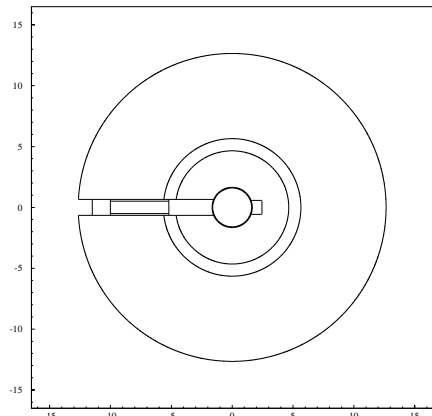


**Figure 10:** From the  ${}^3\text{He}$  proportional counter (3.3 cm in diameter) outwards: 3 cm vacuum, 1 cm lead, 7 cm polyethylene.

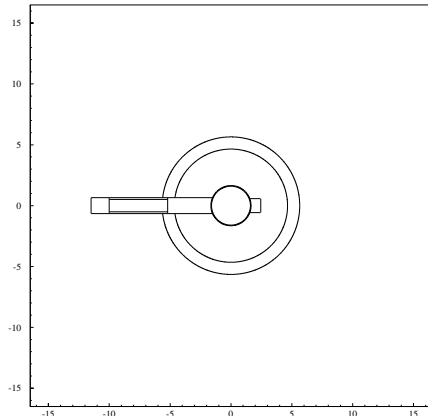


**Figure 11:** From the  ${}^3\text{He}$  proportional counter (3.3 cm in diameter) outwards: 3 cm polyethylene and 1 cm lead.

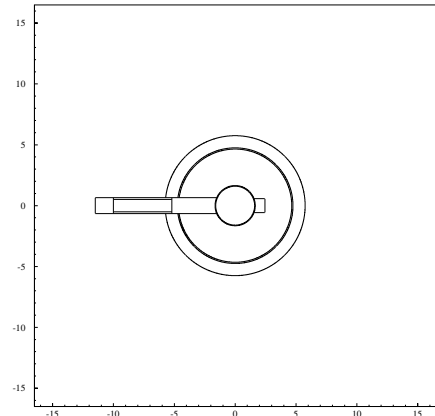


**Figure 12:** From the  ${}^3\text{He}$  proportional counter (3.3 cm in diameter) outwards: 3 cm polyethylene, 1 mm cadmium and 1 cm lead.

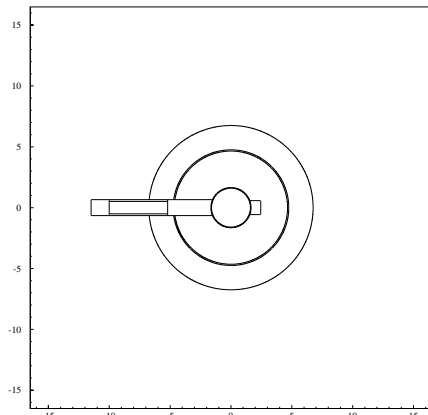


**Figure 13:** From the  ${}^3\text{He}$  proportional counter (3.3 cm in diameter) outwards: 3 cm polyethylene, 1 mm cadmium and 2 cm lead.

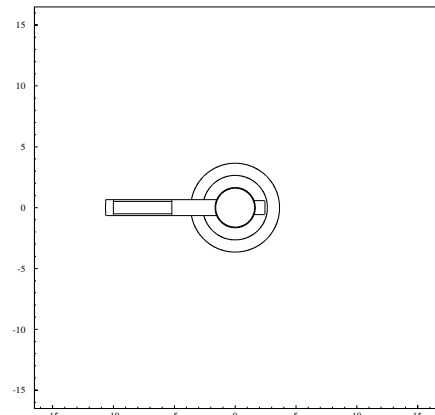


**Figure 14:** From the  ${}^3\text{He}$  proportional counter (3.3 cm in diameter) outwards: 1 cm polyethylene and 1 cm lead.

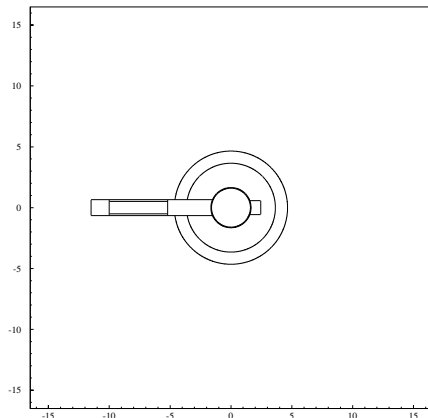


**Figure 15:** From the  ${}^3\text{He}$  proportional counter (3.3 cm in diameter) outwards: 2 cm polyethylene and 1 cm lead.

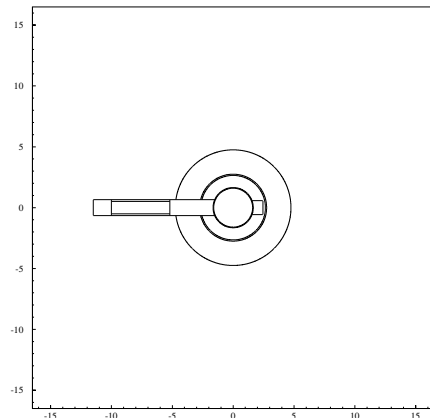


**Figure 16:** From the  ${}^3\text{He}$  proportional counter (3.3 cm in diameter) outwards: 1 cm polyethylene, 1 mm cadmium and 2 cm lead.

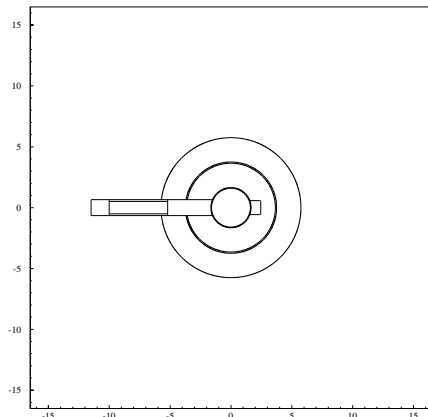


**Figure 17:** From the  ${}^3\text{He}$  proportional counter (3.3 cm in diameter) outwards: 2 cm polyethylene, 1 mm cadmium and 2 cm lead ("Stanlio" design).

# Appendix C

## Response function data

**Table C.1:** Modified response functions of the extended-range BSS. Given is the group response.

| E<br>[MeV] | Fluence Response [cm <sup>2</sup> ] |          |          |          |          |          |          |          |
|------------|-------------------------------------|----------|----------|----------|----------|----------|----------|----------|
|            | 81Cd                                | 81       | 108      | 133      | 178      | 233      | Stanlio  | Ollio    |
| 1.00E-11   |                                     |          |          |          |          |          |          |          |
| 4.14E-07   | 4.04E-02                            | 1.49E+00 | 9.92E-01 | 6.57E-01 | 2.94E-01 | 1.02E-01 | 3.97E-02 | 3.12E-03 |
| 6.83E-07   | 1.30E+00                            | 2.93E+00 | 2.08E+00 | 1.35E+00 | 6.10E-01 | 2.02E-01 | 1.08E+00 | 5.67E-03 |
| 1.13E-06   | 2.73E+00                            | 3.24E+00 | 2.36E+00 | 1.57E+00 | 6.71E-01 | 2.40E-01 | 2.28E+00 | 6.45E-03 |
| 1.64E-06   | 3.23E+00                            | 3.48E+00 | 2.58E+00 | 1.76E+00 | 7.77E-01 | 2.74E-01 | 2.73E+00 | 4.30E-03 |
| 2.38E-06   | 3.42E+00                            | 3.48E+00 | 2.79E+00 | 1.88E+00 | 8.44E-01 | 3.02E-01 | 2.88E+00 | 8.99E-03 |
| 3.47E-06   | 3.50E+00                            | 3.59E+00 | 2.91E+00 | 2.05E+00 | 8.85E-01 | 3.35E-01 | 2.98E+00 | 6.59E-03 |
| 5.04E-06   | 3.56E+00                            | 3.67E+00 | 3.07E+00 | 2.12E+00 | 9.51E-01 | 3.09E-01 | 2.95E+00 | 7.89E-03 |
| 7.34E-06   | 3.53E+00                            | 3.61E+00 | 3.18E+00 | 2.22E+00 | 9.85E-01 | 3.41E-01 | 2.98E+00 | 4.56E-03 |
| 1.07E-05   | 3.57E+00                            | 3.61E+00 | 3.15E+00 | 2.37E+00 | 1.05E+00 | 3.83E-01 | 2.97E+00 | 9.99E-03 |
| 1.55E-05   | 3.51E+00                            | 3.61E+00 | 3.23E+00 | 2.41E+00 | 1.12E+00 | 4.06E-01 | 2.85E+00 | 1.21E-02 |
| 2.26E-05   | 3.36E+00                            | 3.36E+00 | 3.36E+00 | 2.46E+00 | 1.16E+00 | 3.83E-01 | 2.79E+00 | 1.53E-02 |
| 3.73E-05   | 3.20E+00                            | 3.31E+00 | 3.31E+00 | 2.55E+00 | 1.21E+00 | 4.21E-01 | 2.63E+00 | 1.19E-02 |
| 6.14E-05   | 3.20E+00                            | 3.18E+00 | 3.37E+00 | 2.59E+00 | 1.27E+00 | 4.41E-01 | 2.54E+00 | 1.28E-02 |
| 1.01E-04   | 2.69E+00                            | 3.08E+00 | 3.41E+00 | 2.68E+00 | 1.33E+00 | 4.55E-01 | 2.18E+00 | 1.41E-02 |
| 1.67E-04   | 2.70E+00                            | 2.87E+00 | 3.33E+00 | 2.74E+00 | 1.39E+00 | 4.88E-01 | 2.20E+00 | 1.60E-02 |
| 2.75E-04   | 2.70E+00                            | 2.77E+00 | 3.27E+00 | 2.77E+00 | 1.43E+00 | 5.14E-01 | 2.25E+00 | 2.13E-02 |
| 4.54E-04   | 2.47E+00                            | 2.61E+00 | 3.23E+00 | 2.80E+00 | 1.46E+00 | 5.33E-01 | 2.05E+00 | 3.07E-02 |
| 6.89E-04   | 2.50E+00                            | 2.54E+00 | 3.28E+00 | 2.80E+00 | 1.45E+00 | 5.62E-01 | 2.04E+00 | 2.87E-02 |
| 1.04E-03   | 2.33E+00                            | 2.41E+00 | 3.24E+00 | 2.85E+00 | 1.54E+00 | 5.67E-01 | 1.90E+00 | 2.82E-02 |
| 1.58E-03   | 2.25E+00                            | 2.34E+00 | 3.13E+00 | 2.85E+00 | 1.61E+00 | 5.81E-01 | 1.84E+00 | 4.06E-02 |
| 2.31E-03   | 2.16E+00                            | 2.16E+00 | 3.08E+00 | 2.85E+00 | 1.64E+00 | 5.85E-01 | 1.77E+00 | 3.87E-02 |
| 3.35E-03   | 2.08E+00                            | 2.08E+00 | 3.03E+00 | 2.87E+00 | 1.67E+00 | 6.36E-01 | 1.74E+00 | 4.53E-02 |

*Continued.*

| E<br>[MeV] | Fluence Response [cm <sup>2</sup> ] |          |          |          |          |          |          |          |
|------------|-------------------------------------|----------|----------|----------|----------|----------|----------|----------|
|            | 81Cd                                | 81       | 108      | 133      | 178      | 233      | Stanlio  | Ollio    |
| 1.03E-02   | 1.82E+00                            | 1.80E+00 | 2.92E+00 | 2.84E+00 | 1.76E+00 | 6.76E-01 | 1.54E+00 | 6.21E-02 |
| 1.50E-02   | 1.78E+00                            | 1.76E+00 | 2.88E+00 | 2.85E+00 | 1.76E+00 | 7.17E-01 | 1.48E+00 | 6.91E-02 |
| 2.19E-02   | 1.66E+00                            | 1.65E+00 | 2.81E+00 | 2.90E+00 | 1.87E+00 | 7.33E-01 | 1.40E+00 | 7.71E-02 |
| 3.18E-02   | 1.60E+00                            | 1.56E+00 | 2.82E+00 | 2.93E+00 | 1.95E+00 | 7.79E-01 | 1.33E+00 | 8.33E-02 |
| 5.25E-02   | 1.53E+00                            | 1.51E+00 | 2.77E+00 | 2.95E+00 | 2.03E+00 | 8.42E-01 | 1.25E+00 | 1.01E-01 |
| 8.65E-02   | 1.39E+00                            | 1.41E+00 | 2.73E+00 | 3.04E+00 | 2.13E+00 | 9.01E-01 | 1.16E+00 | 1.33E-01 |
| 1.23E-01   | 1.30E+00                            | 1.29E+00 | 2.64E+00 | 3.07E+00 | 2.30E+00 | 1.05E+00 | 1.08E+00 | 1.61E-01 |
| 1.50E-01   | 1.20E+00                            | 1.22E+00 | 2.67E+00 | 3.16E+00 | 2.41E+00 | 1.11E+00 | 1.07E+00 | 2.03E-01 |
| 1.83E-01   | 1.18E+00                            | 1.16E+00 | 2.63E+00 | 3.09E+00 | 2.51E+00 | 1.25E+00 | 1.01E+00 | 2.25E-01 |
| 2.24E-01   | 1.10E+00                            | 1.07E+00 | 2.55E+00 | 3.16E+00 | 2.64E+00 | 1.31E+00 | 9.91E-01 | 2.78E-01 |
| 2.73E-01   | 1.02E+00                            | 1.05E+00 | 2.48E+00 | 3.21E+00 | 2.77E+00 | 1.43E+00 | 9.11E-01 | 3.26E-01 |
| 3.34E-01   | 9.74E-01                            | 9.53E-01 | 2.42E+00 | 3.18E+00 | 2.87E+00 | 1.54E+00 | 8.45E-01 | 3.72E-01 |
| 4.08E-01   | 8.86E-01                            | 8.71E-01 | 2.28E+00 | 3.13E+00 | 3.02E+00 | 1.72E+00 | 8.28E-01 | 4.54E-01 |
| 4.98E-01   | 8.12E-01                            | 7.87E-01 | 2.23E+00 | 3.11E+00 | 3.11E+00 | 1.88E+00 | 7.59E-01 | 5.65E-01 |
| 6.08E-01   | 7.42E-01                            | 7.31E-01 | 2.10E+00 | 3.04E+00 | 3.20E+00 | 2.06E+00 | 6.70E-01 | 6.52E-01 |
| 7.43E-01   | 6.66E-01                            | 6.41E-01 | 1.98E+00 | 2.97E+00 | 3.32E+00 | 2.25E+00 | 5.92E-01 | 7.52E-01 |
| 8.21E-01   | 6.01E-01                            | 5.77E-01 | 1.88E+00 | 2.89E+00 | 3.34E+00 | 2.38E+00 | 5.49E-01 | 8.48E-01 |
| 9.07E-01   | 5.76E-01                            | 5.63E-01 | 1.81E+00 | 2.84E+00 | 3.39E+00 | 2.47E+00 | 5.14E-01 | 9.19E-01 |
| 1.00E+00   | 5.32E-01                            | 5.26E-01 | 1.74E+00 | 2.76E+00 | 3.36E+00 | 2.58E+00 | 5.09E-01 | 9.40E-01 |
| 1.11E+00   | 5.05E-01                            | 4.86E-01 | 1.64E+00 | 2.67E+00 | 3.37E+00 | 2.67E+00 | 4.65E-01 | 1.01E+00 |
| 1.22E+00   | 4.65E-01                            | 4.47E-01 | 1.57E+00 | 2.60E+00 | 3.38E+00 | 2.76E+00 | 4.47E-01 | 1.07E+00 |
| 1.35E+00   | 4.31E-01                            | 4.13E-01 | 1.48E+00 | 2.51E+00 | 3.35E+00 | 2.83E+00 | 4.05E-01 | 1.13E+00 |
| 1.50E+00   | 3.97E-01                            | 3.75E-01 | 1.42E+00 | 2.42E+00 | 3.31E+00 | 2.92E+00 | 3.77E-01 | 1.18E+00 |
| 1.65E+00   | 3.61E-01                            | 3.42E-01 | 1.31E+00 | 2.30E+00 | 3.29E+00 | 2.97E+00 | 3.50E-01 | 1.22E+00 |
| 1.83E+00   | 3.34E-01                            | 3.27E-01 | 1.25E+00 | 2.21E+00 | 3.22E+00 | 3.02E+00 | 3.24E-01 | 1.26E+00 |
| 2.02E+00   | 3.07E-01                            | 2.99E-01 | 1.16E+00 | 2.09E+00 | 3.15E+00 | 3.02E+00 | 3.05E-01 | 1.29E+00 |
| 2.23E+00   | 2.85E-01                            | 2.75E-01 | 1.08E+00 | 1.98E+00 | 3.00E+00 | 2.99E+00 | 2.75E-01 | 1.27E+00 |
| 2.47E+00   | 2.56E-01                            | 2.46E-01 | 1.00E+00 | 1.88E+00 | 2.93E+00 | 3.04E+00 | 2.49E-01 | 1.31E+00 |
| 2.73E+00   | 2.33E-01                            | 2.19E-01 | 9.20E-01 | 1.75E+00 | 2.82E+00 | 2.95E+00 | 2.37E-01 | 1.30E+00 |
| 3.01E+00   | 2.10E-01                            | 1.99E-01 | 8.65E-01 | 1.63E+00 | 2.65E+00 | 2.84E+00 | 2.31E-01 | 1.25E+00 |
| 3.33E+00   | 1.93E-01                            | 1.84E-01 | 7.84E-01 | 1.52E+00 | 2.55E+00 | 2.84E+00 | 2.19E-01 | 1.26E+00 |
| 3.68E+00   | 1.70E-01                            | 1.63E-01 | 7.20E-01 | 1.40E+00 | 2.35E+00 | 2.65E+00 | 2.03E-01 | 1.19E+00 |
| 4.07E+00   | 1.59E-01                            | 1.48E-01 | 6.54E-01 | 1.32E+00 | 2.31E+00 | 2.67E+00 | 1.97E-01 | 1.24E+00 |
| 4.49E+00   | 1.36E-01                            | 1.37E-01 | 6.04E-01 | 1.25E+00 | 2.21E+00 | 2.71E+00 | 1.88E-01 | 1.24E+00 |
| 4.97E+00   | 1.28E-01                            | 1.20E-01 | 5.47E-01 | 1.15E+00 | 2.14E+00 | 2.68E+00 | 1.76E-01 | 1.27E+00 |
| 5.49E+00   | 1.20E-01                            | 1.08E-01 | 5.06E-01 | 1.07E+00 | 2.03E+00 | 2.59E+00 | 1.76E-01 | 1.25E+00 |
| 6.07E+00   | 1.09E-01                            | 9.69E-02 | 4.60E-01 | 9.86E-01 | 1.90E+00 | 2.49E+00 | 1.63E-01 | 1.21E+00 |
| 6.70E+00   | 9.55E-02                            | 8.59E-02 | 4.19E-01 | 9.07E-01 | 1.79E+00 | 2.38E+00 | 1.58E-01 | 1.17E+00 |
| 7.41E+00   | 8.22E-02                            | 7.28E-02 | 3.61E-01 | 7.91E-01 | 1.63E+00 | 2.24E+00 | 1.45E-01 | 1.14E+00 |
| 8.19E+00   | 7.43E-02                            | 6.49E-02 | 3.26E-01 | 7.15E-01 | 1.47E+00 | 2.04E+00 | 1.39E-01 | 1.03E+00 |

*Continued.*

| E<br>[MeV] | Fluence Response [cm <sup>2</sup> ] |          |          |          |          |          |          |          |
|------------|-------------------------------------|----------|----------|----------|----------|----------|----------|----------|
|            | 81Cd                                | 81       | 108      | 133      | 178      | 233      | Stanlio  | Ollio    |
| 9.05E+00   | 6.93E-02                            | 5.41E-02 | 2.75E-01 | 6.58E-01 | 1.35E+00 | 1.94E+00 | 1.63E-01 | 1.02E+00 |
| 1.00E+01   | 5.83E-02                            | 4.84E-02 | 2.50E-01 | 5.54E-01 | 1.20E+00 | 1.75E+00 | 1.75E-01 | 9.67E-01 |
| 1.11E+01   | 5.64E-02                            | 4.73E-02 | 2.32E-01 | 5.19E-01 | 1.13E+00 | 1.68E+00 | 1.87E-01 | 9.79E-01 |
| 1.22E+01   | 5.62E-02                            | 4.30E-02 | 2.20E-01 | 4.97E-01 | 1.05E+00 | 1.56E+00 | 1.96E-01 | 9.44E-01 |
| 1.35E+01   | 4.95E-02                            | 3.47E-02 | 1.84E-01 | 4.24E-01 | 9.37E-01 | 1.40E+00 | 1.95E-01 | 8.96E-01 |
| 1.49E+01   | 4.44E-02                            | 3.61E-02 | 1.79E-01 | 4.04E-01 | 8.97E-01 | 1.36E+00 | 1.90E-01 | 8.81E-01 |
| 1.75E+01   | 4.82E-02                            | 3.43E-02 | 1.73E-01 | 3.98E-01 | 8.63E-01 | 1.31E+00 | 1.90E-01 | 8.87E-01 |
| 1.96E+01   | 4.26E-02                            | 2.87E-02 | 1.43E-01 | 3.26E-01 | 7.34E-01 | 1.12E+00 | 2.20E-01 | 8.62E-01 |

Modified response functions of the extended-range BSS. Given is the point response.

| E<br>[MeV] | Fluence Response [cm <sup>2</sup> ] |          |          |          |          |          |          |          |
|------------|-------------------------------------|----------|----------|----------|----------|----------|----------|----------|
|            | 81Cd                                | 81       | 108      | 133      | 178      | 233      | Stanlio  | Ollio    |
| 21         | 4.04E-02                            | 2.43E-02 | 1.29E-01 | 2.99E-01 |          | 7.62E-01 | 2.63E-01 | 9.51E-01 |
| 25         | 3.54E-02                            | 1.91E-02 | 1.02E-01 | 2.40E-01 | 9.23E-01 | 6.34E-01 | 2.52E-01 | 9.21E-01 |
| 50         | 2.18E-02                            | 7.69E-03 | 4.12E-02 | 9.98E-02 | 4.26E-01 | 2.82E-01 | 3.08E-01 | 9.47E-01 |
| 75         | 2.00E-02                            | 5.85E-03 | 3.20E-02 | 7.77E-02 | 3.28E-01 | 2.15E-01 | 3.11E-01 | 9.62E-01 |
| 100        | 1.85E-02                            | 5.25E-03 | 2.79E-02 | 6.88E-02 | 2.89E-01 | 1.90E-01 | 3.36E-01 | 1.01E+00 |
| 250        | 1.65E-02                            | 3.70E-03 | 2.07E-02 | 5.03E-02 | 2.15E-01 | 1.60E-01 | 4.00E-01 | 1.18E+00 |
| 500        | 1.84E-02                            | 3.50E-03 | 1.90E-02 | 4.67E-02 | 2.09E-01 | 1.34E-01 | 5.41E-01 | 1.59E+00 |
| 750        | 1.87E-02                            | 3.10E-03 | 1.78E-02 | 4.44E-02 | 2.05E-01 | 1.58E-01 | 6.50E-01 | 1.88E+00 |
| 1000       | 1.98E-02                            | 3.10E-03 | 1.78E-02 | 4.37E-02 | 2.04E-01 | 1.30E-01 | 7.23E-01 | 2.11E+00 |
| 1500       | 2.09E-02                            | 3.11E-03 | 1.82E-02 | 4.50E-02 | 2.18E-01 | 1.37E-01 | 8.60E-01 | 2.49E+00 |
| 2000       | 2.10E-02                            | 3.11E-03 | 1.81E-02 | 4.46E-02 | 2.16E-01 | 1.96E-01 | 9.41E-01 | 2.71E+00 |

# Appendix D

## Technical specifications

**Table D.1:** *LINUS settings of the NIM based electronics used in the May 2000 run for Bonner spheres with the 2 atm-detector.*

|                         |             |        |
|-------------------------|-------------|--------|
| High-voltage            | 720 V       |        |
| Amplification           | Coarse Gain | 50     |
|                         | Fine Gain   | 9.80   |
| Shaping time            | 2 $\mu$ s   |        |
| Single channel analyzer | Lower level | 0.20 V |
|                         | Upper level | 9.90 V |

**Table D.2:** *Settings of the MAB electronic device for the three  ${}^3\text{He}$  proportional counters.*

| <b>2 atm-detector</b>   |   |
|-------------------------|---|
| High-voltage            | 812 V   |
| Amplification           | 80  |
| Single channel analyzer | Lower level channel # 107<br>Upper level channel # 2048 |
| <b>4 atm-detector</b>   |   |
| High-voltage            | 890 V   |
| Amplification           | 80  |
| Single channel analyzer | Lower level channel # 107<br>Upper level channel # 2048 |
| <b>B-detector</b>       |   |
| High-voltage            | 824 V   |
| Amplification           | 80  |
| Single channel analyzer | Lower level channel # 97<br>Upper level channel # 2048  |

**Table D.3:** *Technical data of the MAB device components.*

| <b>Spectroscopical amplifier</b> |   |
|----------------------------------|---|
| Input                            | positive 0-5 V  |
| Output                           | positive 0-5 V  |
| Shaping time                     | 3 $\mu$ s   |
| <b>Multi channel analyzer</b>    |   |
| Channels                         | 2048  |
| Max. pulse rate                  | 75000 cps without dead time                           |
| Max. pulses per channel          | $2^{24}$  |
| Preset time                      | 200 ms - 36 h   |
| <b>Power supply</b>              |   |
| Voltage range                    | 0-2000 V  |
| Output current                   | $\leq 0.50$ mA 0-1500 V<br>$\leq 0.25$ mA 1500-2000 V |
| Rising time                      | ca. 200V/s  |
| Stability                        | $\leq 0.01\% / 24h$                                   |
| Polarity                         | positive  |

# Bibliography

[Ago01] S. Agosteo, C. Birattari, A. Foglio-Para, L. Gini, A. Mitaroff, M. Silari, L. Ulrici: *Neutron Production from 158 GeV/c per Nucleon Lead Ions on Thin Copper and Lead Targets in the Angular Range 30°-135°*. Submitted for publication in NIM B

[Alb99] W.G. Alberts, A.V. Alevra, A. Ferrari, T. Otto, U.J. Schrewe, M. Silari: *Calibration Problems, Calibration Procedures and Reference Fields for Dosimetry in Flight Altitudes*. Radiat. Prot. Dosim. **86**, p. 289-295 (1999)

[Amb99] G. Ambrosini et. al.: *Measurements of Charged Particle Production from 450 GeV/c Protons on Beryllium*. European Physical Journal **C10**, p. 604 (1999), CERN-EP/99-19 (1999)

[Apf79] R.E. Apfel: Nucl. Instr. Meth. **162**, p. 603 (1979)

[Ard00] G. Arduini: private communication (2000)

[Arm98] T.W. Armstrong, B.L. Colborn: *Monte-Carlo Prediction of Secondary Neutron Spectra Inside the International Space Station and Comparison with the Space Measurements*. Proc. of Workshop on Predictions and Measurements of Secondary Neutrons in Space. USRA, Houston, Texas, USA 28-30 Sept. 1998, Ed. G.D. Badwhar (1998)

[Aro93] A. Aroua, J. Bourges, C. Raffnsce: *Beam-Monitoring and Data-Logging for the H6 Experiment*. CERN/TIS-RP/TM/93-20 (1993)

[Bar01] D. Bartlett: private communication (2001)

[Bir98a] C. Birattari, A. Esposito, A. Ferrari, M. Pelliccioni, T. Rancati, M. Silari: *The Extended Range Neutron Rem Counter 'Linus': Overview and Latest Developments*. Radiat. Prot. Dosim. **76**, p. 135-148 (1998)

[Bir98b] C. Birattari, A. Ferrari, M. Höfert, T. Otto, T. Rancati, M. Silari: *Recent Results at the CERN-EC High-Energy Reference Field Facility*. Proc. of SATIF-3: Shielding Aspects of Accelerators, Targets and Irradiation Facilities. Sendai, Japan 1997. Ed. NEA/OECD, p. 219-234 (1998)

[Bir01] C. Birattari, P. Cappellaro, A. Mitaroff, M. Silari: *An Extended-Range Bonner Sphere Spectrometer*. Proc. of Advanced Monte-Carlo for Radiation Physics, Particle Transport Simulation and Applications. Lisbon, Portugal 23-26 October 2000. Eds. A. Kling, F. Barao, M. Nakagawa, L. Tavora, P. Vaz, Verlag Springer, p. 1157-1162 (2001)

[Bra60] R.L. Bramblett, R.I. Ewing, T.W. Bonner: Nucl. Instr. Meth. **9**, p. 125 (1960)

[Bre80] H.J. Brede et al.: Nucl. Instr. Meth. **169**, p. 349 (1980)

[Cap00] P. Cappellaro: *Analyse de spectres neutroniques pour la validation des etalonnages dosimétriques dans les installations du CERN*. Tesi di Laurea, politecnico di Milano (2000)

[Car93] A. Carlsson, M.C. Hooper, J. Liu, S. Roesler, G.R. Stevenson: *SL-RP Measurements during the July 1993 CERN-CEC Experiments*. CERN/TIS-RP/TM/93-32 (1993)

[Cha32] J. Chadwick: Proc. Roy. Soc. (London) **136**, p. 692 (1932)

[Col00] G. Collazuol, A. Ferrari, A. Guglielmi, P.R. Sala: *Hadronic Models and Experimental Data for the Neutrino Beam Production*. Nucl. Instr. Meth. **A449**, p. 609-623 (2000)

[Dea63] G. Dearnaley: G.C. Phillips, J.B. Marion, J.R. Risser (Eds.), *Progress in Fast Neutron Physics*. The University of Chicago Press, Chicago, p. 173 (1963)

[Els98a] K. Elsener, M. Heilmann, M. Silari: *Verification of the Calibration Factor of the CERF Beam Monitor*. CERN/TIS-RP/TM/98-22 (1998)

[Els98b] K. Elsener: *Short Introduction to the Use of the H6 Beam*. <http://atlasinfo.cern.ch/Atlas/GROUPS/GENERAL/TESTBEAM/references/H6manual.html> (1998)

[Emm75] M.B. Emmett: *The MORSE Monte Carlo Radiation Transport System*. Oak Ridge National Laboratory, ORNL-4972 (1975)

[Fas97] A. Fassò, et al.: *New Developments in Fluka Modelling of Hadronic and EM Interactions*. Proc. of Third Workshop on Simulating Accelerator Radiation Environments (SARE3). KEK Tsukuba, Japan 7-9 May 1997, Ed. H. Hirayama, KEK Proceedings **97-5**, p. 32 (1997)

[Fas01a] A. Fassò, A. Ferrari, P.R. Sala: *Electron-Photon Transport in FLUKA: Status*. Proc. of Advanced Monte-Carlo for Radiation Physics, Particle Transport Simulation and Applications. Lisbon, Portugal, 23-26 October

2000. Eds. A. Kling, F. Barao, M. Nakagawa, L. Tavora, P. Vaz, Verlag Springer, p. 159-164 (2001).

[Fas01b] A. Fassò, A. Ferrari, J. Ranft, P.R. Sala: *FLUKA: Status and Prospective for Hadronic Applications*. Proc. of Advanced Monte-Carlo for Radiation Physics, Particle Transport Simulation and Applications, Lisbon, Portugal, 23-26 October 2000. Eds. A. Kling, F. Barao, M. Nakagawa, L. Tavora, P. Vaz, Verlag Springer, p. 955-960 (2001).

[Fer91] A. Ferrari, P.R. Sala, R. Guaraldi, F. Padoani: *An Improved Multiple Scattering Model for Charged Particle Transport*. Proc. of Int. Conf. on Radiation Physics. Dubrovnik, 1991, Nucl. Instr. Meth. **B71**, p. 412-426 (1992)

[Fer95] A. Ferrari, P.R. Sala: *Physics of Showers Induced by Accelerator Beams*. Lecture given at the 1995 'Frederic Joliot' Summer School in Reactor Physics. Cadarache, France, 1995.

[Fer97] A. Ferrari, T. Rancati, P.R. Sala: *Fluka Applications in High Energy Problems: From LHC to ICARUS and Atmospheric Showers*. Proc. of Third Workshop on Simulating Accelerator Radiation Environments (SARE3). KEK Tsukuba, Japan, Ed. H. Hirayama, KEK Proceedings **97-5**, p. 165 (1997)

[Gro79] G. Grosshoeg: Nucl. Instr. Meth. **162**, p. 125 (1979)

[Gsc00a] E. Gschwendtner, C.W. Fabjan, T. Otto, H. Vincke: *Measuring the Photon Background in the LHC-Experimental Environment*. Proc. of Inter. Workshop on Neutron Field Spectrometry in Science, Technology and Radiation Protection. 4-8 June 2000, Pisa, Italy. Nucl. Instr. Meth. A (in press)

[Gsc00b] E. Gschwendtner, A. Mitaroff, L. Ulrici: *A New Calibration of the PIC Monitor in H6*. CERN TIS-RP/IR/2000-09 (2000)

[Gul94] S. Guldbakke, E. Dietz, H. Kluge, D. Schlegel: *PTB Neutron Fields for the Calibration of Neutron Sensitive Detectors*. Strahlenschutz: Physik und Meßtechnik. Eds. W. Koelzer, R. Maushart, Verlag TUV Rheinland, Koeln, Vol. **1**, p. 240-247 (1994)

[Gul98] S. Guldbakke, E. Dietz, D. Schlegel: *Properties of the  $^7\text{Li}(p,n)^7\text{Be}$  Neutron Source for Investigation of Fissile Material in Nuclear Waste*. Physikalisch Technische Bundesanstalt PTB-6.41-98-2 (1998)

[Gul01] S. Guldbakke: private communication (2001)

[Har79] J.A. Harvey, N.W. Hill: Nucl. Instr. Meth. **162**, p. 507 (1979)

[Hoo93] M.C. Hooper, C. Raffnsøe, G.R. Stevenson: *Beam Monitoring in the May 1993 CERN-CEC Experiment*. CERN/TIS-RP/TM/93-21 (1993)

[ICR90] International Commission on Radiological Protection: *1990 Recommendations of the International Commission on Radiological Protection*. ICRP Publication 60, Oxford: Pergamon Press (1990)

[ICR95] International Commission on Radiological Protection: *Conversion Coefficients for Use in Radiological Protection against External Radiation*. ICRP Publication 74, Oxford: Pergamon Press (1995)

[ISO99a] International Organization for Standardization: *Reference Neutron Radiations – Part1*. ISO/CDIS 8529-1:1999(E) (1999)

[ISO99b] International Organization for Standardization: *Reference Neutron Radiations – Part2*. ISO/CDIS 8529-2:1999(E) (1999)

[Jaa73] R. Jaarsma, H. Rief: *TIMOC 72 code manual*. Ispra report EUR 5016e (1973)

[Kno79] G.F. Knoll: *Radiation Detection and Measurement*. (1979)

[Leo87] William Leo: *Techniques for Nuclear and Particle Physics Experiments*. Springer (1987)

[Liu93] J. Liu, S. Roesler, G.R. Stevenson: *Carbon-11 In Beam Measurements During the September 1993 CERN-CEC Experiments*. CERN/TIS-RP/TM/93-43 (1993)

[Mar01] V. Mares, A.V. Sannikov, H. Schraube: *Response Functions of the Anderson-Braun and Extended-Range Rem Counters for Neutron Energies from Thermal to 10 GeV*. Proc. of Inter. Workshop on Neutron Field Spectrometry in Science, Technology and Radiation Protection. 4-8 June 2000, Pisa, Italy, Nucl. Instr. Meth. A (in press)

[Mat94] M. Matzke: Physikalisch-Technische Bundesanstalt, Braunschweig PTB-N-19 (1994)

[Mat01] M. Matzke: *Propagation of Uncertainties in Unfolding Procedures*. Proc. of Inter. Workshop on Neutron Field Spectrometry in Science, Technology and Radiation Protection. 4-8 June 2000, Pisa, Italy, Nucl. Instr. Meth. A (in press)

[McE67] W.N. McElroy, S. Berg, T.Crockett, R.G. Hawkins: US Weapons Laboratory Report AFWL-TR-67-41 (1967)

[Mol47] G.Z. Molière: *Theorie der Streuung schneller geladener Teilchen I - Einzelstreuung am abgeschirmten Coulomb-Feld.* Z. Naturforsch. **2a**, p. 133 (1947)

[Mol48] G.Z. Molière: *Theorie der Streuung schneller geladener Teilchen II - Mehrfach und Vielfachstreuung.* Z. Naturforsch. **3a**, p. 78 (1948)

[Mol55] G.Z. Molière: *Theorie der Streuung schneller geladener Teilchen III - Die Vielfachstreuung von Bahnspuren unter Berücksichtigung der statistischen Kopplung.* Z. Naturforsch. **10a**, p. 177 (1955)

[Nel85] W.R. Nelson, H. Hirayama, D.W.O. Rogers: *The EGS4 code system.* SLAC-265 (1985)

[Ott99] T. Otto: *Traceability to International Standards of CERN's Calibration Sources.* CERN/TIS-RP/IR/93-05 (1999)

[Per78] F.G. Perey: *The STAY'SL Code.* Oak Ridge Report ORNL/TM-6062.(N) (1978)

[Ran64] J. Ranft: CERN 64-47 (1964)

[Ran66] J. Ranft: *Estimation of Radiation Problems Around High-Energy Accelerators Using Calculations of the Hadronic Cascade in Matter.* Particle Accelerators **3**, p. 129 (1972)

[Ran70] J. Ranft: *Monte Carlo Calculation of Energy Deposition by the Nucleon-Meson Cascade and Total-Absorption Nuclear Cascade (TANC) Counters.* Nucl. Instr. Meth. **81**, p. 29 (1970)

[Reg99] M. Reginatto, P. Goldhagen: *MAXED, a Computer Code for Maximum Entropy Deconvolution of Multisphere Neutron Spectrometer Data.*, Health Physics **77-5** (1999)

[Rei93] G. Reitz: *Radiation Environment in the Stratosphere.* Radiat. Prot. Dosim. **48**, p. 5-20 (1993)

[Roe94] S. Roesler, G.R. Stevenson: *Carbon-11 Measurements During the May 1994 H6 Runs.* CERN/TIS-RP/TM/94-10 (1994)

[Sch98] D. Schlegel: *Target's User's Manual.* PTB-6.41-1998-1 (1998)

[Sch01] D. Schlegel: private communication (2001)

[Sel85] S.M. Seltzer, M.J. Berger: *Bremsstrahlung Spectra from Electron Interactions with Screened Nuclei and Orbital Electrons.* Nucl. Instr. Meth. **B12**, p. 95 (1985)

[Sel86] S.M. Seltzer, M.J. Berger: *Bremsstrahlung Spectra from Electrons with Kinetic Energy 1 keV-10 GeV Incident on Screened Nuclei and Orbital Electrons of Neutral Atoms with Z = 1-100*. At. Data Nucl. Data Tab. **35**, p. 345 (1986)

[Ste94a] G.R. Stevenson, J. Liu, K. O'Brian, J. Williams: *Beam Intensity Measurements Using  $^{11}C$  Activation for the CERN-CEC Experiments*. CERN/TIS-RP/TM/94-15 (1994)

[Ste94b] G.R. Stevenson, M.C. Hooper, M. Huhtinen, J. Williams: *Measurements of Neutron Yield Using a REM-counter and In-Beam C-11 Activation during the H6A94 Runs at the CERN-CEC Reference Field Facility*. CERN/TIS-RP/TM/94-26 (1994)

[Tho88] D.J. Thomas, N. Soochak: *Determination of the  $^3He$  Number Density for the Proportional Counter Used in the NPL Bonner Sphere System*. NPL Report RS(EXT)104, National Physics Laboratory, Teddington, July 1998

[Tho94] D.J. Thomas, A.V. Alevra, J.B. Hunt, H. Schraube: *Experimental Determination of the Response of Four Bonner Sphere Sets to Thermal Neutrons*. Radiat. Prot. Dosim. **54**, p. 25-31 (1994)

[Ver68] V.V. Verbinski, W.R. Burrus, T.A. Love, et al.: Nucl. Instrum. Meth. **65**, p. 8 (1968)

[Vin99] H. Vincke: private communication (1999)

[Vin00] H. Vincke: FLUKACAD/PIPSICAD: *A 3 dimensional Interface Between FLUKA and AutoCad.*, Proc. of SATIF-5 (2000)

[Vyl97] V. Vylet, J. C. Liu, S.H. Rokni, L.-X. Thai: Radiat. Prot. Dosim. **70**, p. 425-428 (1997)

[Wet81] H. Wetzig, K. Hänßgen, J. Ranft: *Monte-Carlo Simulation of Elastic Hadron Nucleus Reactions with the Computer Code NUCREL*. KMU-HEP 81-07 (1981)

[Wie94] B. Wiegel, A.V. Alevra, B.R.L. Siebert: *Calculations of the Response Functions of Bonner Spheres with a Spherical  $^3He$  Proportional Counter Using a Realistic Detector Model*. PTB-N-21 (1994)

[Wie01] B. Wiegel, A.V. Alevra: *NEMUS-The PTB Neutron Multisphere Spectrometer: Bonner Spheres and More*. Proc. of Inter. Workshop on Neutron Field Spectrometry in Science, Technology and Radiation Protection. 4-8 June 2000, Pisa, Italy. Nucl. Instr. Meth. A (in press)

[Witt01] J. Wittstock: private communication (2001)

# Acknowledgements

First of all I wish to express my gratitude to Prof. Hannes Aigner, my supervisor at the Technical University of Vienna. He was very kind to accept me as his student and thus made it possible for me to gain experience in an exciting international research environment such as CERN.

It is a pleasure for me to thank Marco Silari, my supervisor at CERN who always gave me the possibility to realize my scientific ideas.

I really appreciated to work in the radiation protection group of Hans Menzel. His kind interest in my work and his efforts to provide a comfortable working environment have been of great importance to me.

I am grateful to Thomas Otto for always finding time for discussions, which helped me to better understand my experiments. Many thanks to Alfredo Ferrari and Paola Sala for providing me the FLUKA code and always having time for answering my questions. I am thankful to Graham Stevenson and Helmut Vincke for helping me a lot doing my first steps using FLUKA. I am also indebted to Tiziana Rancati for providing me the old response functions of the conventional Bonner spheres and to Prof. Claudio Birattari for lending me the conventional Bonner spheres and funding the construction of the two new spheres. I am grateful to Prof. Armando Foglio Para and Marcel Reginatto for providing me their unfolding programmes and giving me an introductory tutorial to it. Special thanks go to Stefan Roesler for the careful proof-reading of this thesis.

Many people contributed to the success of my experiments. I am very thankful to Luisa Ulrici for sharing the first beam time period with me and taking over many shifts. Thanks to Konrad Elsener for answering all my questions concerning the beam. I am thankful also to Edda Gschwendtner for sharing her experience concerning the H6 area with me. I am very grateful to Paola Cappellaro, Sabine Mayer and Evangelia Dimovasili for taking over many shifts. I am indebted to Michel Renou, Daniel Perrin and Hubert Müller for their help in all mechanical and electrical aspects and problems, which occurred mainly during the test beams (of course!).

Special thanks go to Burkhard Wiegel from the PTB, who I met at a conference, which was the beginning of a close collaboration during the last year of my thesis. He made the calibration measurements at PTB possible and I could profit a lot from his experience concerning Bonner spheres. Many thanks also to Sigmund Guldbakke and Dietrich Schlegel for providing me the fluence data and the calculated TARGET spectra during my measurements at the PTB. I also owe thanks to Jürgen Wittstock for his practical support during day and night.

I am very thankful for the three years I could spend at CERN financed by a grant of the Austrian Ministry of Science and meeting so many wonderful and interesting people, who enriched my life and made my stay so enjoyable. Especially I want to thank Luisa Ulrici for her friendship and for sharing all my ups and downs during this period.

Finally, I am grateful to my parents for their encouragement and unconditional support during my studies.

# Curriculum Vitae

Angela Mitaroff

Date of birth 24.05.1973  
Place of birth Vienna  
Nationality Austrian

## Education

Nov 1998-Dec 2001 Doctoral thesis at CERN within the TIS/RP group:  
*Design, Calibration and Tests of an Extended Range Bonner Sphere Spectrometer.*  
10.06.1998 Graduated from university with masters degree.  
Diploma examination with excellent success  
(‘mit Auszeichnung’)  
Nov 1996-June 1998 Diploma thesis on the topic of *Dose verification of carbon ion beams with thermo-luminescent dosimeters and CHO cells* performed at the ‘Gesellschaft für Schwerionenforschung - GSI’ in Darmstadt, Germany.  
01.10 1991-10.06.1998 Study of physics at the ‘Technische Universität’ in Vienna  
1983-1991 High school in Vienna ‘Bundesrealgymnasium Wien V’, with advanced levels in physics and biology. Final exams ‘Matura’ with excellent success (‘mit Auszeichnung’)  
1979-1983 Primary school ‘Volksschule der Gemeinde Wien X’

## Specialized Courses, Practical Experience

May 1993-Dec 1994 Student assistant for the international AUSTRON - Project  
01.07.-31.07.1994 Practical work at the ‘Forschungszentrum Seibersdorf’, Austria,  
07.08.-29.09.1995 Participation in the international summer-student programme of GSI in the division of biophysics.  
11.03.-15.03.1996 Participation in a course about vacuum physics organized by the TU-Dresden, Germany  
28.07.-20.09.1996 Participation in the international summer-student programme of DESY  
23.09.-28.09.1997 Participation in a course about diode lasers in the physics centre of Bad Honnef organized by the ‘Deutsche Physikalische Gesellschaft - DPG’.  
Nov 1996-Oct 1998 Student assistant in the division of biophysics at GSI

# Publications

1. A. Mitaroff, W. Kraft-Weyrather, O.B. Geiß, G. Kraft: *Biological Verification of Heavy Ion Treatment Planning*. Radiation and Environmental Biophysics, **37**, p. 47-51 (1998)
2. A. Mitaroff, M. Silari: *Improving the High Energy Response of a Bonner Sphere Spectrometer*. CERN/TIS-RP/IR/99-27 (1999)
3. E. Gschwendtner, A. Mitaroff, T. Otto: *Performance Tests of the CERF Beam Monitor*. CERN/TIS-RP/TM/2000-07 (2000)
4. E. Gschwendtner, A. Mitaroff, L. Ulrici: *A New Calibration of the PIC Monitor in H6*. CERN/TIS-RP/IR/2000-09 (2000)
5. A. Ferrari, A. Mitaroff, M. Silari: *A Reference Radiation Facility for Dosimetry at Flight Altitudes*. Proc. of 1st International Workshop on Space Radiation Research and 11th Annual NASA Space Radiation Health Investigators' Workshop. 27-31 May 2000, Arona, Italy Physica Medica, **17**, p. 116-119 (2001)  
CERN/TIS-RP/IR/2000-15 (2000)
6. A. Mitaroff, M. Silari: *The CERN-EU High-Energy Reference Field (CERF) Facility*. Newsletter European Research in Radiological Sciences No. **9** (2001)
7. A. Mitaroff, E. Dimovasili, S. Mayer, C. Birattari, B. Wiegel, M. Silari, H. Aigner: *Kalibrierung und Experiment eines Bonnerkugel-Spektrometers mit erweitertem Meßbereich*. Proc. of Conf. Strahlenschutz für Mensch und Gesellschaft im Europa von morgen. 17-21 Sep. 2001, Eds. K. Mück, A. Hefner, N. Vana, p. 21-25 (2001)
8. S. Agosteo, C. Birattari, A. Foglio-Para, A. Mitaroff, M. Silari, L. Ulrici: *90° Neutron Emission from High Energy Protons and Lead Ions on a Thin Lead Target*. Proc. of Int. Workshop on Neutron Field Spectrometry in Science, Technology and Radiation Protection, 4-8 June 2000, Pisa, Italy Nucl. Instr. Meth. A (in press)  
CERN Divisional Report: CERN-TIS-2000-011-RP-Conf (2000)

9. A. Mitaroff, M. Silari: *The CERN-EU High-Energy Reference Field (CERF) Facility for Dosimetry at Commercial Flight Altitudes and in Space.* Submitted for publication in Radiat. Prot. Dosim. CERN Divisional Report: CERN-TIS-2001-006-RP-PP (2001)
10. C. Birattari, P. Cappellaro, A. Mitaroff, M. Silari: *Development of an Extended-Range Bonner Sphere Spectrometer.* Proc. of Advanced Monte Carlo for Radiation Physics, Particle Transport Simulation and Applications. 23-26 October 2000, Lisbon, Portugal Conference proceedings (in press) Cern Divisional Report: CERN-TIS-2001-002-RP-Conf (2001)
11. A. Ferrari, A. Mitaroff, M. Silari: *The CERN-EU Radiation Facility for Dosimetry at Flight Altitude and in Space.* Proc. of 16th International Conference on the Application of Accelerators in Research & Industry. 1-4 November 2000 Denton, Texas, USA, Conference proceedings (in press)
12. S. Agosteo, C. Birattari, A. Foglio-Para, L. Gini, A. Mitaroff, M. Silari, L. Ulrici: *Neutron Production from 158 GeV/c per Nucleon Lead Ions on Thin Copper and Lead Targets in the Angular Range 30°-135°.* Submitted for publication in NIM B
13. A. Mitaroff, T. Otto: *Recombination Measurements of the CERF Beam Monitor for a 120 GeV/c Hadron Beam.* CERN/TIS-RP/TM/ (to be published)

### Presentations at Conferences with Book of Abstracts only

1. A. Mitaroff, W. Kraft-Weyrather, G. Kraft, H. Aiginger: *Dosisverifikation für die Schwerionentherapie mit Thermoluminiszenz- dosimetern und CHO-Zellen.* Fachausschusstagung Medizinische Physik, Biophysik, Umweltphysik, 14-18 September 1998, Graz, Austria, Book of Abstracts: p. 172
2. A. Mitaroff, M. Silari, H. Aiginger: *An Extended-Range Bonner Sphere Spectrometer.* 50. OePG-Jahrestagung "Physik-Event 2000", 25-29 September 2000, Graz, Austria, Book of Abstracts: p. 205